THE UNIVERSITY OF CHICAGO

MULTICONFIGURATION PAIR-DENSITY FUNCTIONAL THEORY DEVELOPMENTS AND APPLICATIONS TO PHOTO-CHEMICALLY RELEVANT EXCITED STATES

A DISSERTATION SUBMITTED TO
THE FACULTY OF THE DIVISION OF THE PHYSICAL SCIENCES
IN CANDIDACY FOR THE DEGREE OF
DOCTOR OF PHILOSOPHY

DEPARTMENT OF CHEMISTRY

BY
THAÏS RENÉE SCOTT

CHICAGO, ILLINOIS
DECEMBER 2022

For my mother and father, JoAnn and Donahue Scott. I love you both dearly.

CONTENTS

LIST OF FIGURES

LIST OF TABLES

ACKNOWLEDGMENTS

This collection of works represents input and support from various people. First, I would like to express gratitude for the invaluable guidance and mentorship provided by my advisor, Prof Laura Gagliardi, who provided me with numerous opportunities to develop as a theoretical chemist.

I would also like to thank my committee members, Prof. David Mazziotti and Prof. Giulia Galli for graciously agreeing to be on my committee.

Throughout the past five years, I have been able to collaborate with various groups. For the work included in this dissertation, I would like to thank Eva Vos, Prof Jesús González-Vázquez and Prof Inés Corral for their insight and discussions regarding the formation of photolesions in thiated DNA. Dr. Bholanath Maity, Dr. Gautam D. Stroscio and Prof Luigi Cavallo provided helpful insights for the Ni-Halide dissociation project. For the analytic gradient works, I would like to thank Dr. Jie J. Bao, Dr. Meagan S. Oakley, Dr. Matthew R. Hermes, Prof Andrew M. Sand, Prof Donald G. Truhlar and Prof Roland Lindh for their guidance on these long-term projects.

I have also had fruitful collaborations with Dr. Brendan J Graziano, Dr. Matthew V. Vollmer, Michael J. Dorantes, Dr. Victor G. Young, Dr. Eckhard Bill, Prof Connie C. Lu, Julia G. Knapp, Dr. Debmalya Ray, Dr. Paul B. Calio, Megan C. Wasson, and Prof Omar K. Farha.

I would also like to thank current and former members of the Gagliardi group who have been a wonderful support system. For both scientific and non-scientific advice, I would like to thank Riddhish, Matt, Carlo, Prachi, Aleks, Meagan, Paul, Soumi, Abhishek and Ruhee. My experience in the group was made immeasurably better because of them.

I would also like to thank all of the friends I've made in graduate school and my family who would constantly lift me up. In particular, I'd like to thank Mia and Siri who were always there for me when I would need a shoulder to lean on. I'd like to thank my parents, JoAnn and Donahue, and my siblings, Austin, Alaya, Dacia, and Lela. I would also like to thank Alec for his patience and for a being an incredible partner for the last five years.

ABSTRACT

The primary focus of this research is the development and application of cost efficient multireference methods to quantitatively model chemical phenomena in excited states.

Multi-configuration pair-density functional theory (MC-PDFT) is a method developed in the Gagliardi and Truhlar groups that aims at combining the advantages of wave function and density functional theories to allow robust modeling of strongly correlated systems. While the energies of MC-PDFT with a state-average reference have shown remarkable accuracy for reaction barriers and excitation energies, analytic gradients are necessary for additional applications like efficient calculations of stationary points on potential energy surfaces and direct dynamics simulations. The analytic gradients for MC-PDFT with a state-average reference wave function and density fitting were implemented in the *OpenMolcas* and *PySCF* software. Including density fitting made the code more performant and allowed for the study of significantly larger systems. This was then extended by formulating and implementing gradients and energies for compressed multi-state pair-density functional theory (CMS-PDFT). CMS-PDFT includes state interactions by allowing states to mix through the diagonalization of an effective Hamiltonian. As a result, this method gives the correct shape of the potential energy surface for systems with nearly degenerate states, e.g., near conical intersections or locally avoided crossings.

In this work, we are interested in photosensitization, which is a process where a light-harvesting molecule transfers energy to a substrate and promotes it to an excited state. This excitation mechanism is important for the photochemistry of Ir-Ni dual catalysis and photolesion formation in thio-substituted DNA. In both studies, the insights provided by the MC-PDFT calculations helped to determine the mechanism responsible for these photochemical reactions.

CHAPTER 1

INTRODUCTION

1.1 Motivation

The interaction of light and molecules is integral for a broad variety of physical phenomena. After exposure to light, molecules can be promoted into excited electronic states where the electrons populate orbitals in such a way that the energy is higher than in its resting or ground state configuration. The energy of the light required to populate these states is proportional to the difference in energy between the ground and excited states. Additionally, other factors can dictate whether exposure to light results in a specific excited state, for example symmetry considerations. In the present work, we are generally interested in transfers from singlet to triplet states, where the total angular momentum, S, changes from 0 to 1.

Excitations from a ground state singlet to a triplet state are particularly interesting because of the potential for novel reactivity. Unfortunately, inefficient intersystem crossing or extremely small absorption cross sections often prevent significant population of these high-energy states via direct excitation. To overcome this issue, a secondary molecule called a photosensitizer can be used to absorb light and then transfer a portion of this energy to another substrate, promoting it to a previously inaccessible high-energy triplet state. While photosensitization has been a tool for accessing excited states in organic chemistry since the 1960s,[3,4] there has been renewed interest in the topic as a way to access excited states in other contexts, for example organometallic catalysis[5] and photodamage of DNA.[6]

Currently, photosensitization processes with visible light are being intensively investigated[5] for organometallic catalysts because of the potential for novel chemical transformations. Photosensititizers can be used with diverse organic substrates and proceed via mechanistically distinct cross-coupling pathways.[7] Unfortunately, the short lifetimes of relevant excited states limit the experimental insights, and theoretical studies are needed to understand the mechanisms govern-

ing the catalysis.[8] In this work, we are interested in the role of triplet excited states in $LNi^{II/III}$(Aryl)(Halide) complexes for Ni–Halide bond homolysis. Understanding the electronic structure of this Ni-Halide homolysis is an important step in tuning and controlling the arylation of $C(sp^3)$–H bonds. This is a major challenge in organic chemistry because, under classical conditions, the individual catalysts are reliant on their specific visible light absorption cross section. With photosensitization, we can bypass this requirement with a general photosensitizer and access a broader range of excited states.[9]

There is also widespread interest in thiated nucleobases because of their potential function as photosensitizers in medicinal chemistry. The formation of genotoxic photoproducts in canonical and thio-substituted DNA nucleobases is thought to be the result of triplet energy transfer but the exact role of the triplet states is still unclear.[10] Canonical DNA nucleobases have very short-lived triplet excited states with ultrafast repopulation of the ground state which makes the study of these states difficult experimentally.[11–13] The triplet excited states of the thiated DNA analogues are much longer lived[14] and allow for experimental observation and subsequent theoretical comparisons. From these comparisons, one can depict the predictive power of various theoretical methods and provide a protocol for future studies involving canonical nucleobases. We are also interested in the differences, at the electronic structure level, between the thiated and canonical nucleobases in the ground state to ensure that alternative causes of photodamage are explored.[15]

Considering the complexity of the excited-state reaction paths[16] involved in these applications, one must employ a robust and efficient theoretical method with an adequate treatment of electron correlation effects. In this work, we employ multi-configuration pair-density functional theory[17,18] (MC-PDFT) which has proven to be a successful method for studying excited states, with applications ranging from energy gaps for diradical systems[19] to accurate ordering of the excited states in benzene.[20] Analytic gradients for MC-PDFT[21] for ground states using a state-specific reference wave function have been used to optimize geometries for the calculation of adiabatic singlet-triplet splitting in diradical pyrazines[22] and of barrier heights for a set of small

organic chemical reactions.[23]

In this work, we have developed analytic gradients of MC-PDFT with a state-average reference wave function to study the excited states of chemical systems,[1] reduced the computational cost of manipulating the two-electron integrals by implementing density fitting,[24] and implemented the compressed multi-state PDFT (CMS-PDFT) analytic gradients.[25] We then use MC-PDFT to study the photosensitization of dual catalysis[26] and thiated DNA nucleobases.[27] In the following sections of the Introduction, we discuss the theoretical background required to derive the analytic gradients.

1.2 Potential Energy Surfaces

The Schrödinger equation[28] describes the quantum-mechanical behavior of particles, making it the most fundamental equation in quantum chemistry. We are interested in the non-relativistic, time-independent Schrödinger equation,

$$\hat{H} |\Psi\rangle = E |\Psi\rangle \tag{1.1}$$

where $\hat{H}$ is the Hamiltonian, Ψ is the wave function, and E is the energy. For a molecule, the exact wave function depends explicitly on both the coordinates of the electrons and nuclei. However, it is convenient to separate the motion of the electrons from the motion of the nuclei using the Born-Oppenheimer (BO) approximation.[29] Within the BO approximation, one assumes that the electronic wave function depends only on the nuclear positions and does not depend on their velocities. We also assume that the nuclei only experience a smeared-out potential of electrons. As a result of this approximation, the Hamiltonian can be separated into electronic and nuclear terms and a hyper-surface can be defined that describes how the electronic energy varies with a change in the nuclear coordinates.

The potential energy hyper-surface will be referred to as the potential energy surface (PES)

in the following text, as a hyper-surface is difficult to visualize and interpret. In many cases, it is more helpful to visualize one or two important geometric coordinates with a curve or surface, respectively. However, it is important to note that we are still concerned with the total hyper-surface when discussing stationary points and the optimization procedures used to locate them.

Each excited state is associated with an individual PES and these excited states can be accessed via adiabatic or non-adiabatic photochemistry. The term adiabatic means states do not cross each other and that transfers between states occur via absorption or emission of light. Non-adiabatic reactions can non-radiatively jump from surface to surface when states get close in energy. For the majority of this research the focus is the adiabatic states, but we do, in Chapter 4, discuss the changes to the Hamiltonian needed to accurately treat non-radiative transitions.

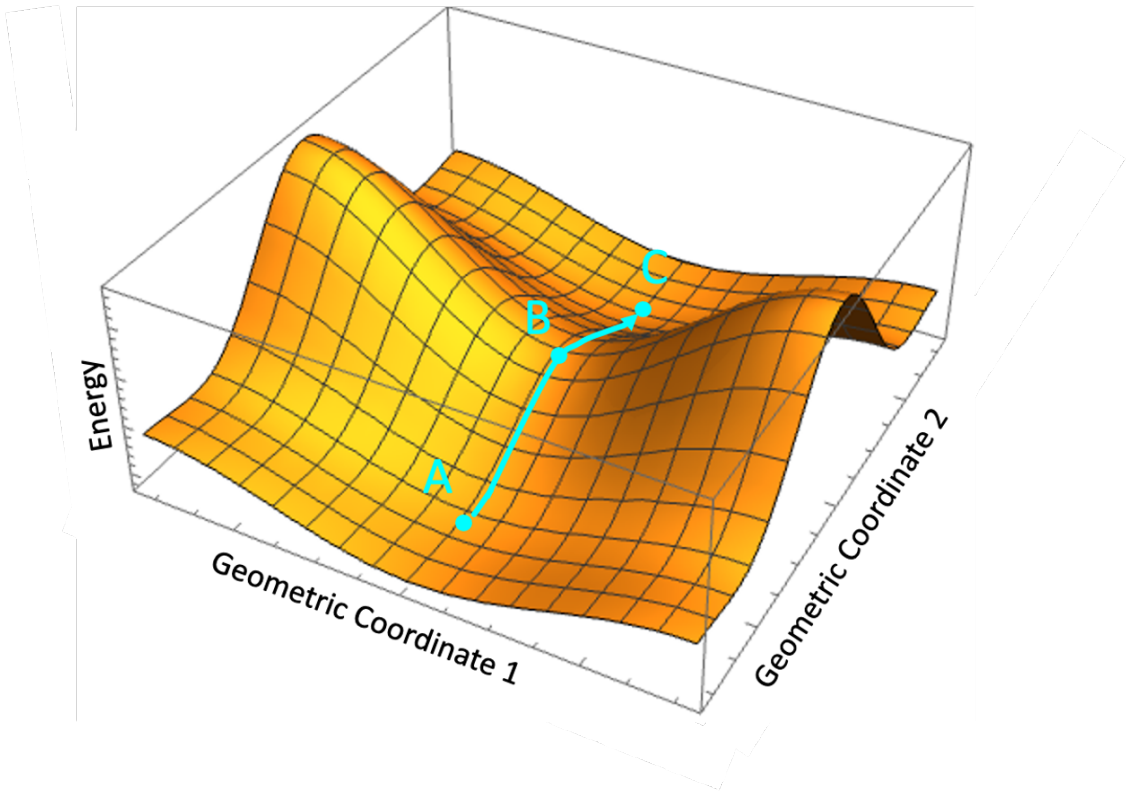

Figure 1.1: Simplified schematic of a general potential energy surface. A and C are minima and B is the lowest energy saddle point that connects them. The arrow represents the reaction path.

The position of minima and the lowest energy pathway between them, shown in figure 1.1, is particularly relevant for chemical applications. These paths represent the transformation of reactants, to intermediates and transition states, and then finally to products.[30] Stationary points or optimized geometries are located on the ground or excited state surface by constructing a local quadratic approximation of the PES and then minimizing it by following the gradient descent. There are many classes of gradient descent methods[31] and those methods will not be discussed here, but all of them rely on efficient gradient computations. Determining the gradient of the energy with numerical differentiation is only feasible for small systems as multiple single point energy calculations are required for each atom. The development of much more efficient analytical formulations for the energy gradient are needed to study larger systems.

One of the most fundamental concepts for analytic gradients of the energy is the Hellmann-Feynman theorem.[32,33] This theorem states, that the derivative of an energy, E, that is variational or a stationary point with respect to all parameters defining its underlying wave function is explicitly dependent on the Hamiltonian only, and one can disregard the implicit dependence on the wave function.

$$\frac{\partial E}{\partial \lambda} = \langle \Psi | \frac{\partial \hat{H}}{\partial \lambda} | \Psi \rangle \tag{1.2}$$

where λ is a perturbation; this allows one to avoid the tedious task of evaluating the response of the parameters of the wave function with respect to the coordinates of the perturbation. However, the MC-PDFT energy methods are not variational and we must use additional tools to compute efficient gradients.

1.3 Non-Variational Energy Gradients

In this section, we will briefly define the general form of the analytic derivative for a non-variational energy. Handy and Schaefer,[34] introduced a protocol that simplified the gradients, which was

later refined by Helgaker and Jørgensen.[35] This simplification makes use of Lagrange's method of undetermined multipliers and has been employed for various non-variational energies. It is sometimes referred to as the generalized Hellmann-Feynman theorem.

The energy is a function of an external perturbation λ, and the un-optimized (non-variational) internal parameters of the wave function, $\mathbf{C}$.

$$\mathcal{E} = \mathcal{E}(\lambda, \mathbf{C}) \tag{1.3}$$

In a non-variational energy, some wave function parameters are determined by a condition W_k that minimizes an alternative (often simpler) energy expression, e,

$$W_k(\lambda, \mathbf{C}) = \frac{\partial e(\lambda, C)}{\partial C_k} = 0 \tag{1.4}$$

where $k = 1, .., N$ and N is the total number of conditions responsible for determining the elements in $\mathbf{C}$. We then form a Lagrangian as

$$\mathcal{L}(\lambda, \mathbf{C}, z) = \mathcal{E}(\lambda, \mathbf{C}) - \sum_k z_k W_k(\lambda, \mathbf{C}) \tag{1.5}$$

The Lagrangian is equivalent to the total energy because 1.4 is equivalent to 0. Therefore taking the derivative of the Lagrangian is also equivalent to taking the derivative of the energy.

$$\frac{\partial \mathcal{E}(\lambda, \mathbf{C})}{\partial \lambda} = \frac{\partial \mathcal{L}(\lambda, \mathbf{C}(\lambda), z)}{\partial \lambda} = \frac{\partial \mathcal{E}}{\partial \lambda} - \sum_k z_k \frac{\partial W_k(\lambda, \mathbf{C}(\lambda))}{\partial \lambda} \tag{1.6}$$

The benefit of forming the Lagrangian is that one can assert that its derivative with respect to each of the $\mathbf{C}$ components is zero by solving for the appropriate multipliers, z_k. This process removes the need to solve the wave function response equations ($\partial C_k / \partial \lambda$), and reduces the computational effort needed to compute the gradient of the energy significantly.

The Lagrange multiplier terms that account for the response of the non-variational wavefunc-

tion parameters are contained in the effective density matrix.[36] A general energy of a molecule with a finite basis set can be written, in second quantization, as

$$E = V_n + \sum_{pq} h_q^p D_q^p + \frac{1}{2} \sum_{pqrs} g_{qs}^{pr} d_{qs}^{pr} \tag{1.7}$$

where V_n, h_q^p and g_{qs}^{pr} are the zero-, one-, and two-body Hamiltonian matrix elements; D_q^p refers to the one-body reduced density matrix for orbitals p and q, and d_{qs}^{pr} represents the two-body reduced density matrix for orbitals p, q, r and s. The terms h_{pq} and g_{pqst} are the one-electron and two-electron matrix elements defined as

$$h_q^p = \int \phi_p^*(\mathbf{r}) h(i) \phi_q(\mathbf{r}) d\mathbf{r} \tag{1.8}$$

$$g_{qs}^{pr} = \int \int \phi_p^* \phi_r^* \frac{1}{r_{12}} \phi_q \phi_t d\mathbf{s}_1 d\mathbf{r}_2 \tag{1.9}$$

where h(i) is the one-body operator,

$$\hat{h} = \sum_i \nabla_i^2 - \sum_A \frac{Z_A}{r_{iA}} \tag{1.10}$$

ϕ_p is a general orbital p, r_iA is the distance between particles i and A, and $\mathbf{r}$ are the spatial coordinates. The derivatives of the h_q^p and g_{qs}^{pr} integrals contribute to the gradient through two chain rule terms, a portion that is directly dependent the changes in the integral and another that is dependent, indirectly, on the change in the wave function (spin-orbitals ϕ). The effective densities are the derivatives of the total energy with respect to a given integral, including all coupling terms, while keeping all other quantities unchanged. It is symmetrized to have the same permutational symmetry as the one- and two-electron integrals. Using this formalism, one can rewrite the energy derivative to the order a as

$$E^{(a)} = V_n^{(a)} + \sum_{pqs} \breve{D}_q^p h_q^{p(a)} + \frac{1}{2} \sum_{pqrs} \breve{d}_{qs}^{pr} g_{pr}^{pr(a)} \tag{1.11}$$

where $\breve{D}$ and $\breve{d}$, are one and two body effective density matrices. The effective densities do not contain any dependence on the perturbation and depend only on the definition of the energy functional for the particular method. It is important to note that h_q^p and g_{qs}^{pr} also contain renormalization terms which account for how the atomic-orbital basis functions shift with a change in geometry.[37]

These tools are the general framework for the gradients of non-variational energies. Since a variety of electronic structure methods have been formulated in this unified way, one can repurpose gradients code for more facile implementations of analytic gradients for modern electronic structure methods.

1.4 Electron Correlation

Analytic solutions to the Schrödinger equation within the BO approximation are only available for a handful of trivial systems, and the development of computationally efficient and accurate approximations to $\hat{H}$ is a large portion of quantum chemical research. The basis of many of these methods is called Hartree-Fock (HF) theory, which assumes that each electron is an independent particle moving in an average field of the other electrons. Each electron has an associated molecular orbital (MO) or spin-orbital that is comprised of spin and spatial components. For our purposes, these MOs are Gaussian-type orbitals expanded into a fixed, finite set of atom-centered basis functions or atomic orbitals (AOs). The total HF wavefunction for an n electron system is an anti-symmetrized product of MOs, called a Slater determinant. The restricted HF method uses a single Slater determinant to define the wave function and the orbitals for HF are obtained in a variational manner. This means that the wave function that minimizes the HF energy is the optimal wave function for the given molecular system.

The difference between the exact energy and the HF energy is called the electron correlation energy. Formally one cannot separate the electron correlation energy into distinct parts but it is nevertheless convenient in describing the shortcomings of HF. Static correlation effects arise because of near-degeneracies in the one-particle basis states and systems with significant static

correlation are referred to as strongly correlated. Multi-configurational or multi-reference methods are designed to address this challenge by including a linear combination of Slater determinants in the wave function. Dynamic correlation is associated with the mean-field approximation in HF which poorly describes the instantaneous changes in the wave function as two electrons approach one another. Many theoretical methods address this effect by excitation into virtual orbitals but this is usually computationally expensive.

Until this point we have focused mostly on wave function theory, but a more efficient way to solve the Schrödinger equation is with Kohn-Sham density functional theory[38,39] (KS-DFT). KS theory is based on an existence theorem that states that there is a universal exchange– correlation functional that relates the ground-state energy to the electron density, exactly. There is no systematic way to obtain this functional, and it is likely impossible to define.[40] There are many approximations to the universal functional that have been developed,[41] but in general KS-DFT performs reasonably well for most systems that are single configurational in nature. This treatment reduces the N-particle problem from 3N dimensions in wave function theories to a set of more manageable N coupled 3-dimensional equations. These equations can be solved in a similar way to HF theory, as the exact ground-state density minimizes the exchange correlation (XC) functional. However, KS-DFT often converges to the incorrect or broken-symmetry wave functions for strongly correlated systems. Ideally one would want to combine the efficiency of KS-DFT with the wave functions obtained with multi-configuration wave function theories and there have been many attempts to do so.[42] In this work, specifically, we discuss the MC-PDFT method which was proposed by the Gagliardi and Truhlar groups.[17,18]

1.5 Multiconfiguration Pair-Density Functional Theory

In this section we discuss the MC-PDFT energy but let us first introduce the notation. In the following text, the indices $p, q, r, s, t...$ refer to general molecular orbitals and $\kappa, \lambda, \mu, \nu...$ refer to one-electron basis functions, taken here as primitive or contracted Gaussians. The indices $I, J, K...$

refer to the states included in the average of the SA-CASSCF calculations (this set of states is referred to below as averaged states) and $R, S, T...$ refer to eigenstates of the Hamiltonian in the complementary part of the active space, referred to as the unaveraged space. The index Λ refers to CSFs, and the index A is used for atoms. In practice it is necessary to partition the MOs into inactive, active, and virtual sets for efficient implementation, but this notationally-complex distinction is omitted in this section for brevity.

The MC-PDFT energy is

$$E_{\text{MC-PDFT}} = V_n + h^p_q D^p_q + \frac{1}{2} g^{pr}_{qs} D^p_q D^r_s + E_{\text{OT}}[\rho, \rho', \Pi, \Pi'], \tag{1.12}$$

where E_{OT}, which is expressed as a functional of the electronic density, ρ, the on-top pair density, Π, and their derivatives, is called the on-top energy. The definitions of the electronic density, on-top pair density, and their derivatives are

$$\rho = \phi_p D^p_q \phi_q \tag{1.13}$$

$$\rho' = \phi'_p D^p_q \phi_q + \phi_p D^p_q \phi'_q. \tag{1.14}$$

$$\Pi = \frac{1}{2} \phi_p \phi_q d^{pr}_{qs} \phi_r \phi_s \tag{1.15}$$

$$\begin{aligned} \Pi' = \frac{1}{2} (&\phi'_p \phi_q d^{pr}_{qs} \phi_r \phi_s + \phi_p \phi'_q d^{pr}_{qs} \phi_r \phi_s \\ &+ \phi_p \phi_q d^{pr}_{qs} \phi'_r \phi_s + \phi_p \phi_q d^{pr}_{qs} \phi_r \phi'_s) \end{aligned} \tag{1.16}$$

where ρ, Π, and ϕ_p, ϕ_q, etc. are all functions of one 3-dimensional real-space coordinate, $\boldsymbol{r}$, and ϕ_p is the p^{th} molecular orbital. MC-PDFT does not suffer from the "symmetry dilemma"[43,44] of KS-DFT and other single-determinantal methods, in which one must choose between physically realistic spin densities and accurate total energies, because it always involves a reference wave function that is an eigenfunction of $\hat{S}^2$, where $\hat{S}$ is the total electron spin operator.

MC-PDFT uses on-top functionals E_{ot} translated from KS exchange-correlation functionals

E_{xc},[17] such that

$$E_{\mathrm{ot}}[\rho, \Pi, \rho'] = E_{\mathrm{xc}}[\tilde{\rho}_\alpha, \tilde{\rho}_\beta, \tilde{\rho}'_\alpha, \tilde{\rho}'_\beta] \tag{1.17}$$

where the translation involves fictitious nonphysical spin densities and their derivatives:

$$\tilde{\rho}_\alpha = \begin{cases} \frac{\rho}{2}\left(1 + \sqrt{1-R}\right) & R \leq 1 \\ \frac{\rho}{2} & R > 1 \end{cases} \tag{1.18}$$

$$\tilde{\rho}_\beta = \begin{cases} \frac{\rho}{2}\left(1 - \sqrt{1-R}\right) & R \leq 1 \\ \frac{\rho}{2} & R > 1 \end{cases} \tag{1.19}$$

$$\tilde{\rho}'_\alpha = \begin{cases} \frac{\rho'}{2}\left(1 + \sqrt{1-R}\right) & R \leq 1 \\ \frac{\rho'}{2} & R > 1 \end{cases} \tag{1.20}$$

$$\tilde{\rho}'_\beta = \begin{cases} \frac{\rho'}{2}\left(1 - \sqrt{1-R}\right) & R \leq 1 \\ \frac{\rho'}{2} & R > 1 \end{cases} \tag{1.21}$$

where R is also a function of the three-dimensional real-space coordinate $\boldsymbol{r}$ and is given by

$$R = \frac{4\Pi}{\rho^2} \tag{1.22}$$

The full translation scheme[45], with dependence on Π' has also been developed to smooth out discontinuities caused by the discrete translation. As mentioned in the motivation section MC-PDFT has been very successful in studies for excited states by using a state-average (SA) reference wavefunction. SA-CASSCF is a method used to treat ground and excited states with a consistent set of orbitals that minimize the average energy of a set of states. In the following section, we describe the implementation and formal derivation of the first order analytic derivatives with respect to the nuclear coordinates of the MC-PDFT energy with a state-average reference wave function.

Some sections contain replications of text from reference 1. All text is used with permission.

CHAPTER 2

ANALYTIC GRADIENTS FOR STATE-AVERAGED MULTICONFIGURATION PAIR-DENSITY FUNCTIONAL THEORY

2.1 Introduction

Here we expand the capabilities of SA-PDFT by deriving and implementing analytic gradients of the energy that can be used to determine stationary points on excited-state potential energy surfaces or to carry out efficient direct dynamics simulations. Analytic gradients are more efficient than numeric gradients for medium-sized and large molecules (e.g. nucleobases).[46] Additionally, there is no finite difference error when the gradient is computed analytically.

The present work builds on previous work in which SS-PDFT[47] gradients were derived and implemented in *OpenMolcas*.[48] Here we extend that work to SA-PDFT, and we implement analytic SA-PDFT gradients in both *OpenMolcas* and *mrh*,[49] which is an add-on to PySCF.[50] First the theory and a formal cost scaling analysis of the SA-PDFT gradients are presented. Then the correctness of the analytic gradients is validated through a comparison to numeric gradients across the potential energy curve for lithium hydride. Finally, the excitation energies and optimized equilibrium geometries for formaldehyde, *trans*-butadiene, and cytosine are reported.

2.2 Theory

2.2.1 Lagrangian

The Lagrangian in the SS-PDFT case is

$$\begin{aligned} \mathscr{L}_{\text{MC-PDFT}} &= E_{\text{MC-PDFT}} + \vec{z} \cdot \nabla_{\vec{\Psi}} E_{\text{CASSCF}} \\ &= E_{\text{MC-PDFT}} + \vec{z}_{\text{orb}} \cdot \nabla_{\vec{\kappa}} E_{\text{CASSCF}} + \vec{z}_{\text{CI}} \cdot \nabla_{\vec{p}} E_{\text{CASSCF}} \end{aligned}$$

where $\nabla_{\vec{\Psi}} E_{\text{CASSCF}}$ is the gradient of the CASSCF energy with respect to the orbital rotations ($\nabla_{\vec{\kappa}}$) and state transfer operators ($\nabla_{\vec{P}}$). The parameterization of the CASSCF energy that allows the evaluation of these derivatives is

$$E_{\text{CASSCF}} = \langle \text{CAS} | \bar{H} | \text{CAS} \rangle \tag{2.1}$$

where $|\text{CAS}\rangle$ is the CASSCF wave function, and $\bar{H}$ is defined as

$$\bar{H} = e^{-\hat{P}} e^{-\hat{\kappa}} \hat{H} e^{\hat{\kappa}} e^{\hat{P}} \tag{2.2}$$

$$\hat{\kappa} = \sum_{p<q} \kappa_q^p (\hat{E}_q^p - \hat{E}_p^q) \tag{2.3}$$

$$\hat{P} = \sum_{\Lambda} P_\Lambda (|\Lambda\rangle \langle \text{CAS}| - |\text{CAS}\rangle \langle \Lambda|) \tag{2.4}$$

where κ_q^p and P_Λ are operator amplitudes and $\hat{E}_q^p$ is the spin-summed excitation operator from the q^{th} to the p^{th} orbital. Note that the sum in Eq. (2.4) is over all CSFs in the active space. Since the CASSCF energy is stationary with respect to the parameters κ_q^p and P_Λ, the value of the Lagrangian, $\mathscr{L}_{\text{MC-PDFT}}$, is equal to the SS-PDFT energy regardless of the value of the Lagrange multipliers, $\vec{z}$. Therefore, one can choose these multipliers such that the Lagrangian is stationary with respect to all wave function parameters by solving [using, for example, the preconditioned conjugate gradient (PCG) method[51]]

$$\nabla_{\vec{\Psi}} \mathscr{L}_{\text{MC-PDFT}} = \nabla_{\vec{\Psi}} E_{\text{MC-PDFT}} + \mathbf{H}_{\vec{\Psi}}^{E_{\text{CAS}}} \cdot \vec{z} = \vec{0} \tag{2.5}$$

whereupon the Hellman-Feynman theorem applies to $\mathscr{L}_{\text{MC-PDFT}}$ and yields the same gradient as full differentiation of $E_{\text{MC-PDFT}}$. The gradient vector of the SS-PDFT energy with respect to wave function parameters is $\nabla_{\vec{\Psi}} E_{\text{MC-PDFT}}$; it will be called the energy response, and it is discussed in the following section. The term $\mathbf{H}_{\vec{\Psi}}^{E_{\text{CAS}}}$ is the Hessian matrix for the CASSCF energy with respect to wave function parameters.

The generalization of this procedure to the SA-PDFT case is discussed next. In general, the Lagrangian must contain multipliers associated with every parameter that may respond to a change in molecular geometry but with respect to which the energy is not stationary, and these multipliers must have cofactors that accurately represent the conditions determining the values of those parameters. This means that for SA-PDFT there must be two classes of CI transfer parameters that solve different sets of equations. Therefore we distinguish two kinds of terms in Eq. (2.4):

$$\begin{aligned}\hat{P} &= \sum_{J,R} P_{JR} \left(|R\rangle \langle J| - |J\rangle \langle R| \right) \\ &\quad + \sum_{J \neq I} P_{IJ} \left(|J\rangle \langle I| - |I\rangle \langle J| \right)\end{aligned} \tag{2.6}$$

where I indexes the root for which the molecular gradient is sought (and is not summed in the second term); $|J\rangle$ is an active-space state that appears in the state average; and $|R\rangle$ is an active-space state that does not appear in the state average (as mentioned at the beginning of the Theory section, these states are called unaveraged states). The orbital parameters (κ_q^p) and the CI parameters (P_{JR}) minimize the SA-CASSCF energy:

$$E_{\text{CASSCF}}^{\text{SA}} = \sum_{J}^{n_{SA}} \omega_J \langle J| \bar{H} |J\rangle \tag{2.7}$$

where ω_J is the weight of the J^{th} root in the state average and in this work we assume equal weights in all cases. The SA-CASSCF energy is insensitive to the CI parameters (P_{IJ}) of the averaged states because with the assumption of equal weights it is the trace of a Hermitian matrix under unitary transformation. Instead, P_{IJ} are chosen to diagonalize the Hamiltonian in the state-averaged space:

$$\langle I| \bar{H} |J\rangle = \delta_{IJ} E_{\text{CASSCF}}^{(I)} \quad \forall \quad J \tag{2.8}$$

Comparison of Eqs. (2.2), (2.6), and (2.8) reveals that this is equivalent to a stationarity condition

for the I^{th} root:

$$\frac{\partial E^{(I)}_{\text{CASSCF}}}{\partial P_{IJ}} = \langle I|\,\bar{H}\,|J\rangle + \langle J|\,\bar{H}\,|I\rangle = 0 \;\; \forall \;\; J \neq I \tag{2.9}$$

Therefore, for the I^{th} root in SA-PDFT, the Lagrangian is

$$\begin{aligned}
\mathscr{L}^{(I)}_{\text{MC-PDFT}} &= E^{(I)}_{\text{MC-PDFT}} + \vec{z}_{\text{orb}} \cdot \nabla_{\vec{\kappa}} E^{\text{SA}}_{\text{CASSCF}} \\
&\quad + \sum_{J}^{n_{\text{SA}}} \omega_J z_{JR} \frac{\partial E^{(J)}_{\text{CASSCF}}}{\partial P_{JR}} + \sum_{J\neq I}^{n_{\text{SA}}} \omega_I z_{IJ} \frac{\partial E^{(I)}_{\text{CASSCF}}}{\partial P_{IJ}} \\
&= E^{(I)}_{\text{MC-PDFT}} + \vec{z}_{\text{orb}} \cdot \nabla_{\vec{\kappa}} E^{\text{SA}}_{\text{CASSCF}} \\
&\quad + \sum_{J}^{n_{\text{SA}}} \omega_J \vec{z}^{(J)}_{\text{CI}} \cdot \nabla_{\vec{P}_J} E^{(J)}_{\text{CASSCF}}
\end{aligned} \tag{2.10}$$

where in the second equality there has been a transformation from the eigenstate to the CSF basis in the second index of P_{IJ} and P_{JR}, and the elements of $\vec{z}^{(J)}_{\text{CI}}$ are

$$z_{J\Lambda} = \begin{cases} \sum_R z_{JR} \langle R|\Lambda\rangle + \sum_K^{n_{\text{SA}}} z_{IK} \langle K|\Lambda\rangle & J = I \\ \sum_R z_{JR} \langle R|\Lambda\rangle & \text{otherwise} \end{cases} \tag{2.11}$$

Because the coefficient matrix generated by differentiation of Eq. (2.10) is not symmetric, one cannot apply the PCG method to solve for the values of all Lagrange multipliers in one step. Instead, the linear equations $\nabla_{\vec{\Psi}} \mathscr{L}^{(I)}_{\text{MC-PDFT}} = \vec{0}$ are solved in two steps. First, the insensitivity of the SA energy to P_{IJ} is exploited to solve analytically for the CI Lagrange multipliers corresponding to averaged states:

$$z_{IJ} = -(E^{(J)}_{\text{CASSCF}} - E^{(I)}_{\text{CASSCF}})^{-1} \frac{1}{2\omega_I} \frac{\partial E^{(I)}_{\text{MC-PDFT}}}{\partial P_{IJ}} \tag{2.12}$$

which is possible because the eigenstate basis renders the relevant Hessian matrix diagonal. Sec-

ond, all other Lagrange multipliers are solved for using the PCG method in the CSF basis,

$$\begin{aligned}\nabla_{\vec{\Psi}}\mathscr{L}^{(I)}_{\text{MC-PDFT}} &= \mathbf{P}_{\text{ext}} \cdot \nabla_{\vec{\Psi}} E^{(I)}_{\text{MC-PDFT}} \\ &\quad + \sum_{J}^{n_{\text{SA}}} \omega_J \mathbf{P}_{\text{ext}} \mathbf{H}^{E^{(J)}_{\text{CAS}}}_{\vec{\Psi}} \cdot \vec{z}^{(J)} = \vec{0}\end{aligned} \tag{2.13}$$

where $\mathbf{H}^{E^{(J)}_{\text{CAS}}}_{\vec{\Psi}}$ is the CASSCF Hessian matrix for the J^{th} root and where $\vec{z}^{(J)}$ includes both $\vec{z}^{(J)}_{\text{CI}}$ and the orbital Lagrange multipliers common to all roots, $\vec{z}_{\text{orb}}$. The projector matrix, $\mathbf{P}_{\text{ext}}$, eliminates all components of CI transfers between states in the average manifold,

$$\{\mathbf{P}_{\text{ext}}\}_{J\Lambda,J\Lambda'} = 1 - \sum_{K}^{n_{\text{SA}}} |\Lambda\rangle \langle\Lambda|K\rangle \left\langle K\middle|\Lambda'\right\rangle \left\langle\Lambda'\right| \tag{2.14}$$

thus fixing the z_{IJ} components at the analytically determined values and preventing any spurious components rotating two averaged roots other than I (z_{JK}) from emerging. Note that the Hessian is projected on only *one* side, so that the response of the orbital and unaveraged CI degrees of freedom to z_{IJ} is included. In practice, if an implementation of an SA-CASSCF "Hessian" matrix is available, it may not be necessary to include $\mathbf{P}_{\text{ext}}$ explicitly, but care must be taken to ensure that this matrix is nonsymmetric in the specific way that reproduces Eq. (2.13) precisely.

2.2.2 Energy Response

The Hessian matrix of the CASSCF energy of the J^{th} root, $\mathbf{H}^{E^{(J)}_{\text{CAS}}}_{\vec{\Psi}}$, is already implemented in many quantum chemistry packages and is not further discussed here. It remains to discuss the PDFT energy response, $\nabla_{\vec{\Psi}} E^{(I)}_{\text{MC-PDFT}}$. The formulae for this response in the SA-PDFT and SS-PDFT cases are essentially the same, and we note that all densities and density matrices that appear in this section in the SA case correspond to the I^{th} root (not the state average). The overall formulae

for the elements of the response (in the CSF basis where applicable) are

$$\frac{\partial E_{\text{MC-PDFT}}}{\partial \kappa_q^p} = F_q^p - F_p^q \tag{2.15}$$

$$\frac{\partial E_{\text{MC-PDFT}}}{\partial P_{I\Lambda}} = \langle I| \hat{H}_{\text{ps}} \hat{Q}_I |\Lambda\rangle + \langle \Lambda| \hat{Q}_I \hat{H}_{\text{ps}} |I\rangle \tag{2.16}$$

$$\frac{\partial E_{\text{MC-PDFT}}}{\partial P_{J\Lambda}} = 0 \ \forall \ J \neq I \tag{2.17}$$

with

$$F_q^p = \left(h_r^p + g_{rt}^{ps} D_t^s + V_r^p\right) D_r^q + v_{rt}^{ps} d_{rt}^{qs} \tag{2.18}$$

$$\hat{H}_{\text{ps}} = \left(h_q^p + g_{qs}^{pr} D_s^r + V_q^p\right) \hat{E}_q^p + \frac{1}{2} v_{qs}^{pr} \hat{e}_{qs}^{pr} \tag{2.19}$$

$$\hat{Q}_I = 1 - |I\rangle \langle I| \tag{2.20}$$

and where V and v are one- and two-body effective potentials respectively, and $\hat{e}_{qs}^{pr}$ is the spin-summed two-electron excitation from orbitals q, s to p, r. Note that Eq. (2.16) spans both the averaged and unaveraged spaces [i.e., it contributes to both Eq. (2.12) and Eq. (2.13)].

The effective potentials account for the differentiation of the on-top energy. They are

$$V_q^p = \int \frac{\partial \epsilon_{\text{OT}}}{\partial \rho} \phi_p \phi_q + \frac{\partial \epsilon_{\text{OT}}}{\partial \rho'} (\phi'_p \phi_q + \phi_p \phi'_q) d\boldsymbol{r} \tag{2.21}$$

$$v_{qs}^{pr} = \int \frac{\partial \epsilon_{\text{OT}}}{\partial \Pi} \phi_p \phi_q \phi_r \phi_s d\boldsymbol{r} \tag{2.22}$$

where ϵ_{OT} is the integrand of the exchange-correlation energy with respect to a real-space coordinate,

$$E_{\text{OT}} = \int \epsilon_{\text{OT}}(\boldsymbol{r}) d\boldsymbol{r} \tag{2.23}$$

As discussed earlier, the on-top functional is a translation of a Kohn-Sham density functional. Therefore, the derivatives of the integrand ϵ_{OT} (collectively $\nabla_{\vec{\rho}} \epsilon_{\text{OT}}$) are obtained *via* the chain

rule:

$$\nabla_{\vec{\rho}}\,\epsilon_{\mathrm{OT}} = \nabla_{\vec{\tilde{\rho}}}\,\epsilon_{\mathrm{XC}} \cdot \mathbf{J}^{\vec{\tilde{\rho}}}_{\vec{\rho}} \tag{2.24}$$

where $\nabla_{\vec{\tilde{\rho}}}\,\epsilon_{\mathrm{XC}}$ is

$$\nabla_{\vec{\tilde{\rho}}}\,\epsilon_{\mathrm{XC}} = \left\{ \frac{\partial \epsilon_{\mathrm{XC}}}{\partial \tilde{\rho}_\alpha}, \frac{\partial \epsilon_{\mathrm{XC}}}{\partial \tilde{\rho}_\beta}, \frac{\partial \epsilon_{\mathrm{XC}}}{\partial \tilde{\rho}'_\alpha}, \frac{\partial \epsilon_{\mathrm{XC}}}{\partial \tilde{\rho}'_\beta} \right\} \tag{2.25}$$

and the Jacobian matrix, $\mathbf{J}^{\vec{\tilde{\rho}}}_{\vec{\rho}}$, is

$$\mathbf{J}^{\vec{\tilde{\rho}}}_{\vec{\rho}} = \begin{Bmatrix} \frac{\partial \tilde{\rho}_\alpha}{\partial \rho} & \frac{\partial \tilde{\rho}_\alpha}{\partial \rho'} & \frac{\partial \tilde{\rho}_\alpha}{\partial \Pi} \\ \frac{\partial \tilde{\rho}_\beta}{\partial \rho} & \frac{\partial \tilde{\rho}_\beta}{\partial \rho'} & \frac{\partial \tilde{\rho}_\beta}{\partial \Pi} \\ \frac{\partial \tilde{\rho}'_\alpha}{\partial \rho} & \frac{\partial \tilde{\rho}'_\alpha}{\partial \rho'} & \frac{\partial \tilde{\rho}'_\alpha}{\partial \Pi} \\ \frac{\partial \tilde{\rho}'_\beta}{\partial \rho} & \frac{\partial \tilde{\rho}'_\beta}{\partial \rho'} & \frac{\partial \tilde{\rho}'_\beta}{\partial \Pi} \end{Bmatrix} \tag{2.26}$$

The quantities in Eq. (2.25) can be obtained in standard KS-DFT implementations. Those in Eq. (2.26) are obtained by applying the chain rule to Eqs. (1.18-1.21) and (1.22) and are tabulated in the SI.

2.2.3 Derivative of the Lagrangian

Given a set of Lagrange multipliers which solve Eqs. (2.12) and (2.13), the molecular gradient for the I^{th} root MC-PDFT energy in SA-PDFT is obtained by differentiating Eq. (2.10) with respect to nuclear displacements. The chain rule for this operation generates terms involving the derivatives of the Hamiltonian matrix elements, AO overlap integrals in a finite AO basis, the exchange-correlation energy (including grid coordinates and grid weights in a finite quadrature grid), and density matrices. The last of these are dropped because they are indirectly derivatives of wave function parameters which are constrained to sum to zero by Lagrange's method of undetermined multipliers.

The derivatives of the Hamiltonian and overlap matrix elements are obtained in the AO basis

as

$$h_\lambda^{\tilde{\kappa}} \equiv \int \Big(\frac{1}{2}\phi_\kappa \nabla_{\vec{\boldsymbol{R}}_A} \hat{h}_{\text{core}} \phi_\lambda - P_{A\kappa}\phi'_\kappa \hat{h}_{\text{core}}\phi_\lambda\Big) d\boldsymbol{r} \tag{2.27}$$

$$g_{\lambda\nu}^{\tilde{\kappa}\mu} \equiv -P_{A\kappa}\int \phi'_\kappa(\boldsymbol{r}_1)\phi_\lambda(\boldsymbol{r}_1) r_{12}^{-1}\phi_\mu(\boldsymbol{r}_2)\phi_\nu(\boldsymbol{r}_2) d\boldsymbol{r}_1 d\boldsymbol{r}_2 \tag{2.28}$$

$$s_\lambda^{\tilde{\kappa}} \equiv P_{A\kappa}\int \phi'_\kappa \phi_\lambda d\boldsymbol{r} \tag{2.29}$$

These equations are essentially first derivatives of the Hamiltonian and overlap matrix elements with respect to the three components of the A^{th} atomic nucleus's coordinate, $\boldsymbol{R}_A$. The term $P_{A\kappa}$ is 1 if κ is an atomic orbital centered on atom A and 0 otherwise.

The derivatives of the exchange-correlation energy can be evaluated in more than one way because they involve tensor products that can be carried out in various orders. Here, we present these derivatives as they are evaluated in our *OpenMolcas* implementation. We generate $3N_{\text{atom}}$ atomic-coordinate derivatives of the translated densities and their electron-coordinate derivatives (collectively denoted $\nabla_{\vec{\lambda}}\vec{\tilde{\rho}}$) by using the Jacobian given by Eq. (2.26) and the atomic-coordinate derivatives of the true density and density derivatives (used in many standard DFT codes) and on-top pair density:

$$\nabla_{\vec{\lambda}}\vec{\tilde{\rho}} = J^{\vec{\tilde{\rho}}}_{\vec{\rho}} \cdot \nabla_{\vec{\lambda}}\vec{\rho}, \tag{2.30}$$

with

$$\nabla_{\vec{\lambda}}\vec{\tilde{\rho}} = \left\{\nabla_{\vec{\lambda}}\tilde{\rho}_\alpha, \nabla_{\vec{\lambda}}\tilde{\rho}_\beta, \nabla_{\vec{\lambda}}\tilde{\rho}'_\alpha, \nabla_{\vec{\lambda}}\tilde{\rho}'_\beta\right\} \tag{2.31}$$

$$\nabla_{\vec{\lambda}}\vec{\rho} = \left\{\nabla_{\vec{\lambda}}\rho, \nabla_{\vec{\lambda}}\rho', \nabla_{\vec{\lambda}}\Pi\right\} \tag{2.32}$$

$$\nabla_{\vec{\lambda}_A}\rho = -2P_{A\kappa}\phi'_\kappa D_\lambda^\kappa \phi_\lambda + P_{A\boldsymbol{r}}\rho' \tag{2.33}$$

$$\nabla_{\vec{\lambda}_A}\rho' = -2P_{A\kappa}\left(\phi''_\kappa D_\lambda^\kappa \phi_\lambda + \phi'_\kappa D_\lambda^\kappa \phi'_\lambda\right) + P_{A\boldsymbol{r}}\rho'' \tag{2.34}$$

$$\nabla_{\vec{\lambda}_A}\Pi = -2P_{A\kappa}\phi'_\kappa \phi_\lambda d_{\lambda\nu}^{\kappa\mu}\phi_\mu\phi_\nu + P_{A\boldsymbol{r}}\Pi' \tag{2.35}$$

where $P_{A\boldsymbol{r}}$ is 1 if $\boldsymbol{r}$ is evaluated at a grid point associated with the A^{th} atom and 0 otherwise, and the symbol $\nabla_{\vec{\lambda}_A}$ in Eqs. (2.33)–(2.35) refers respectively to the components of $\nabla_{\vec{\lambda}}\rho$, $\nabla_{\vec{\lambda}}\rho'$, and $\nabla_{\vec{\lambda}}\Pi$ which involve the A^{th} atom. The contribution to the molecular gradient is then evaluated with a standard KS-DFT analytical gradient code,

$$\nabla_{\vec{\lambda}} E_{\text{OT}} = \int \left(\nabla_{\vec{\lambda}} \vec{\rho} \cdot \nabla_{\vec{\rho}} \epsilon_{\text{XC}} \right) d\boldsymbol{r} + \epsilon_{\text{OT}}(\vec{\boldsymbol{r}}) \cdot J^{\vec{w}}_{\vec{\lambda}} \tag{2.36}$$

where the last term accounts for the response of the quadrature weights of the numeric integration (not to be confused with the state-averaged weights of various roots) and corresponds simply to the quadrature evaluation of Eq. (2.23) with $3N_{\text{atom}}$ sets of derivatives of quadrature weights in place of the weights themselves.

The details of our PySCF implementation are not presented in detail, but that implementation rearranges the intermediates of Eqs. (2.30)–(2.36) to generate derivatives of V and v analogous to $h^{\tilde{\kappa}}_{\lambda}$ and $g^{\tilde{\kappa}\lambda}_{\mu\nu}$.

The full expression for the molecular gradient, including the differentiated Hamiltonian, overlap, and exchange-correlation contributions, including all finite-grid and finite-basis corrections, is

$$\begin{aligned} \nabla_{\vec{\lambda}} E_{\text{MC-PDFT}} = {} & 2[h^{\tilde{p}}_q + g^{\tilde{p}r}_{qs} D^r_s] D^p_q + \nabla_{\vec{\lambda}} E_{\text{OT}} \\ & + 2(h^{\tilde{p}}_q \breve{D}^p_q + g^{\tilde{p}r}_{qs} \breve{d}^{pr}_{qs}) \\ & - [s^{\tilde{p}}_q + s^{\tilde{q}}_p](F^p_q + \breve{F}^p_q) \end{aligned} \tag{2.37}$$

where F^p_q is from Eq. (2.18), and $\breve{F}^p_q$ is

$$\breve{F}^p_q = h^p_r \breve{D}^q_r + g^{ps}_{rt} \breve{d}^{sq}_{tr} \tag{2.38}$$

The effective density matrices, $\breve{D}$ and $\breve{d}$, contain the Lagrange multipliers as follows:

$$\begin{aligned}
\breve{D}^p_q &= \sum_s (\{D_{\mathrm{SA}}\}^s_q z^p_s - \{D_{\mathrm{SA}}\}^p_s z^s_q) \\
&\quad + \sum_{J,\Lambda} w_J z_{J\Lambda} (\langle \Lambda | \hat{E}^p_q | J \rangle + \langle J | \hat{E}^p_q | \Lambda \rangle) \qquad (2.39) \\
\breve{d}^{pr}_{qs} &= \sum_t (\{d_{\mathrm{SA}}\}^{ts}_{qs} z^p_t - \{d_{\mathrm{SA}}\}^{pr}_{ts} z^t_q + \{d_{\mathrm{SA}}\}^{pt}_{qs} z^r_t - \{d_{\mathrm{SA}}\}^{pr}_{qt} z^t_s) \\
&\quad + \sum_{J,\Lambda} w_J z_{J\Lambda} (\langle \Lambda | \hat{e}^{pr}_{qs} | J \rangle + \langle J | \hat{e}^{pr}_{qs} | \Lambda \rangle) \qquad (2.40)
\end{aligned}$$

where D_{SA}, d_{SA} are the state-averaged one- and two-body density matrices. All other density matrices appearing in Eq. (2.37) arise from the differentiation of $E^{(I)}_{\text{MC-PDFT}}$ and are specific to the I^{th} root.

2.2.4 Operation cost, storage cost, and timing

Previous work has reported the attractive timing and low memory requirements of MC-PDFT energy computations as compared to those of CASPT2.[19,52–56] Here we discuss additional considerations related to timing and memory requirements when one calculates gradients.

The intermediate arrays and tensors that appear above have the same dimensions and sizes as comparable quantities utilized in the evaluation of SA-CASSCF or KS-DFT analytical gradients. The calculations of the two-body effective potential terms (v) dominate the overall cost of the SA-PDFT gradient steps, and for these as well as the on-top pair density (Π) and its various derivatives, we exploit the partition of the MO indices into those for inactive, active, and virtual orbitals. The largest segment of the effective potential or 2-RDM required at any step in the evaluation of SA-PDFT analytical gradients is that which appears in Eq. (2.18). Here, the block-diagonal structure of the 2-RDM is exploited so that only two-body effective potential elements with at least three indices restricted to the active space are explicitly calculated (this also applies to derivatives of v alluded to in the previous section). This leads to operation and storage costs respectively of

$O(M^1 M^3_{\mathrm{CAS}} n_{\mathrm{grid}})$ and $O(M^1 M^3_{\mathrm{CAS}})$ associated with the two-body effective potentials, where M, M_{CAS}, and n_{grid} are the numbers respectively of AOs, active orbitals, and quadrature grid points. This should be compared to $O(M^4 M^1_{\mathrm{CAS}})$ operation and $O(M^3 M^1_{\mathrm{CAS}})$ storage costs for the leading step of the integral transformations required in CASSCF without density fitting.

In practice one usually has $n_{\mathrm{grid}} \gg M$, so the two-body effective potential evaluation is often the slowest part of SA-PDFT gradient calculations, including the preceding CASSCF energy calculation. It should also be noted that available memory is used to vectorize the effective potential calculations, so actual memory consumption will often be higher than the minimal "cost" discussed here. Additionally, this analysis ignores the $O(e^{M_{\mathrm{CAS}}})$ operation and storage cost associated with manipulating the active-space CI vector, which dominates the overall cost of the method in the limit of large M_{CAS}.

2.3 Computational Methods

All SA-PDFT calculations were performed using local versions of *OpenMolcas*[48] and the PySCF[50] add-on package *mrh*[49] using the tPBE on-top functional. Geometry optimizations using energies and gradients computed by PySCF and *mrh* were carried out by the external program geomeTRIC.[57] All SA-PDFT computations were performed with the aug-cc-pVTZ basis set and an ultrafine grid size. The CASPT2 geometry optimizations were performed using the same local version of *OpenMolcas* and the 6-311G+(2df) basis set for cytosine. numeric gradients were computed for CASPT2 since analytic gradients are not yet implemented in *OpenMolcas* or PySCF. The CASPT2 computations were performed with a state-averaged reference wave function, but the PT2 corrections and the PDFT energies were computed independently and the states were not allowed to interact. For the CASPT2 calculations, the default IPEA shift value, 0.25 E_h, was used, and the default number of frozen deep core orbitals was used for each system studied here. For the numeric gradient in *OpenMolcas* a Δ value of 0.06 was used and convergence criteria for the orbital rotation matrix and energy gradient were set to 1.0e-05.

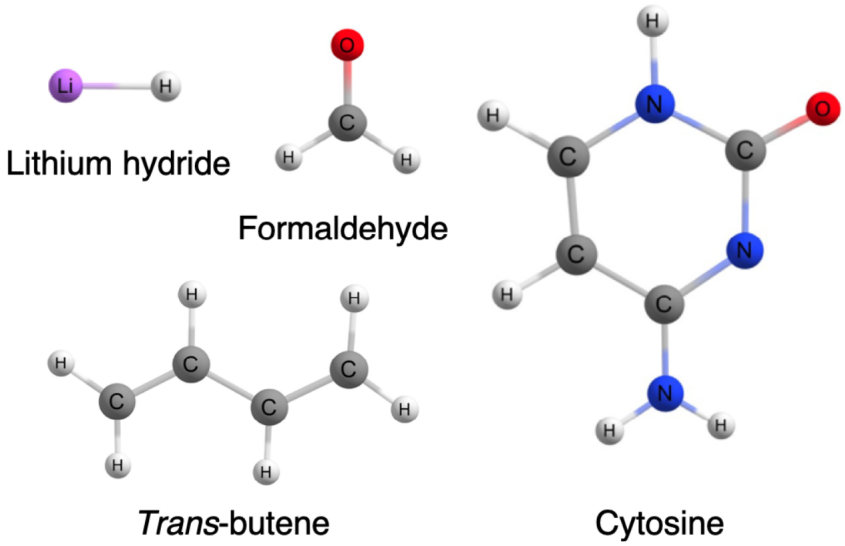

Figure 2.1: Systems studied to verify the analytic gradients.

A set of four molecules (shown in Figure 2.1) were used to assess the correctness of the analytic gradients and the accuracies of geometries and excitation energies computed with SA-PDFT. All states studied are singlet states.

The active space used for lithium hydride contains one σ and one σ^* orbital. The active space of formaldehyde is composed of pairs of bonding/antibonding σ(C-H), σ(C=O), and π(C=O) orbitals, oxygen lone pairs, and two second-shell oxygen lone pair orbitals. Two π and two π^* orbitals and the associated electrons are included in the active space for *trans*-butadiene. The active space for cytosine includes the entire occupied π space and lone pair orbitals with three correlating π^* orbitals. Active spaces sizes, symmetry constraints, number of configurations, and the states included in the average for all molecules studied with SA-PDFT are shown in Table 2.1.

Table 2.1: The active spaces, symmetry constraints, number of configuration state functions (CSFs), and number of included states in the state-averaged framework for all systems included in the benchmark study.

System	Active Space	Symmetry	States Averaged	CSFs
Lithium Hydride	(2e,2o)	None Enforced	2	3
Formaldehyde	(12e,12o)	None Enforced	2	226,512
Trans-butadiene	(4e,4o)	C_{2h}	2 (^1A_g)	12
Cytosine	(14e,10o)	C_s	3 (^1A_g)	2,598

2.4 Results

We will consider lithium hydride, formaldehyde, and *trans*-butadiene to test the correctness of the analytic gradient implementation, and then we will consider formaldehyde, *trans*-butadiene, and cytosine to test the accuracy of geometries predicted by SA-PDFT with the newly implemented analytic gradients.

2.4.1 Correctness of Analytic Gradients

Gradients were first computed for the ground and first-excited singlet states of LiH to show the agreement between the numeric and analytic gradients. Two low-lying singlet states, namely the $X^1\Sigma^+$ and $A^1\Sigma^+$ states, were considered; we can label the states as S_0 and S_1. Gradients were computed for both states at 0.1 Å intervals from 0.5 Å to 5.5 Å, and they are shown in Figure 2.2 along with the potential energy curves. The numeric and analytic gradients agree at all distances.

The experimentally determined equilibrium bond distances[58] for the $X^1\Sigma^+$ and $A^1\Sigma^+$ states are 1.60 Å and 2.60 Å. The calculated values are 1.62 Å and 2.91 Å respectively; the latter does not agree well with experiment. This disagreement is a consequence of the notoriously flat shape of the A state potential well (which is "anomalous" with "a long history"[58]) that arises from an avoided crossing and from severe configuration mixing of valence bond states with ionic, covalent

Li 2s, and covalent Li 2p characters;[59,60] the flatness means that a small shift in the energies can be associated with a large shift in the equilibrium distance. To get quantitative results one should treat the curve crossing region with state-interaction methods including at least three states.[59,60] We note though that the two-state treatment of LiH is not presented here as an attempt to treat this molecule accurately but rather to demonstrate the correctness of the implementation of analytic gradients on a simple case.

The mean unsigned deviation (MUD) for the SA-PDFT analytic gradients compared to the numeric gradients is 4×10^{-5} hartree bohr^{-1}. The same analysis was performed with SA-CASSCF and the MUD between the analytic and numeric gradients was 2×10^{-5} hartree bohr^{-1}. The analysis for SA-CASSCF is shown in the SI in Figure S1. This shows that the SA-PDFT numeric and analytic gradients agree as well as do the SA-CASSCF analytic and numeric gradients. Further checks involving the SA-PDFT numeric gradients from formaldehyde and *trans*-butadiene are presented in the SI in table S1.

2.4.2 Formaldehyde

Here optimized geometries for the ground and first-excited singlet states of formaldehyde are compared to experiment and to theoretical structural parameters reported in the work of Budzak, Scalmani, and Jacquemin[61] and references therein. The benchmark data set includes geometries determined at ADC(2), CC2, CCSD, CCSDR(3), and CC3 levels of theory. Note that the geometries of both the ground and first excited electronic states are predicted from SA-PDFT calculations based on the same SA-CASSCF active space.

Table 2.2 shows that all methods included in this work produce results in good agreement with experiment for the ground-state geometries, and SA-PDFT is the best performing method for the ground state of formaldehyde. In the following text experimental values are considered the reference but it should be noted that a comparison to experiment tests not just SA-PDFT but

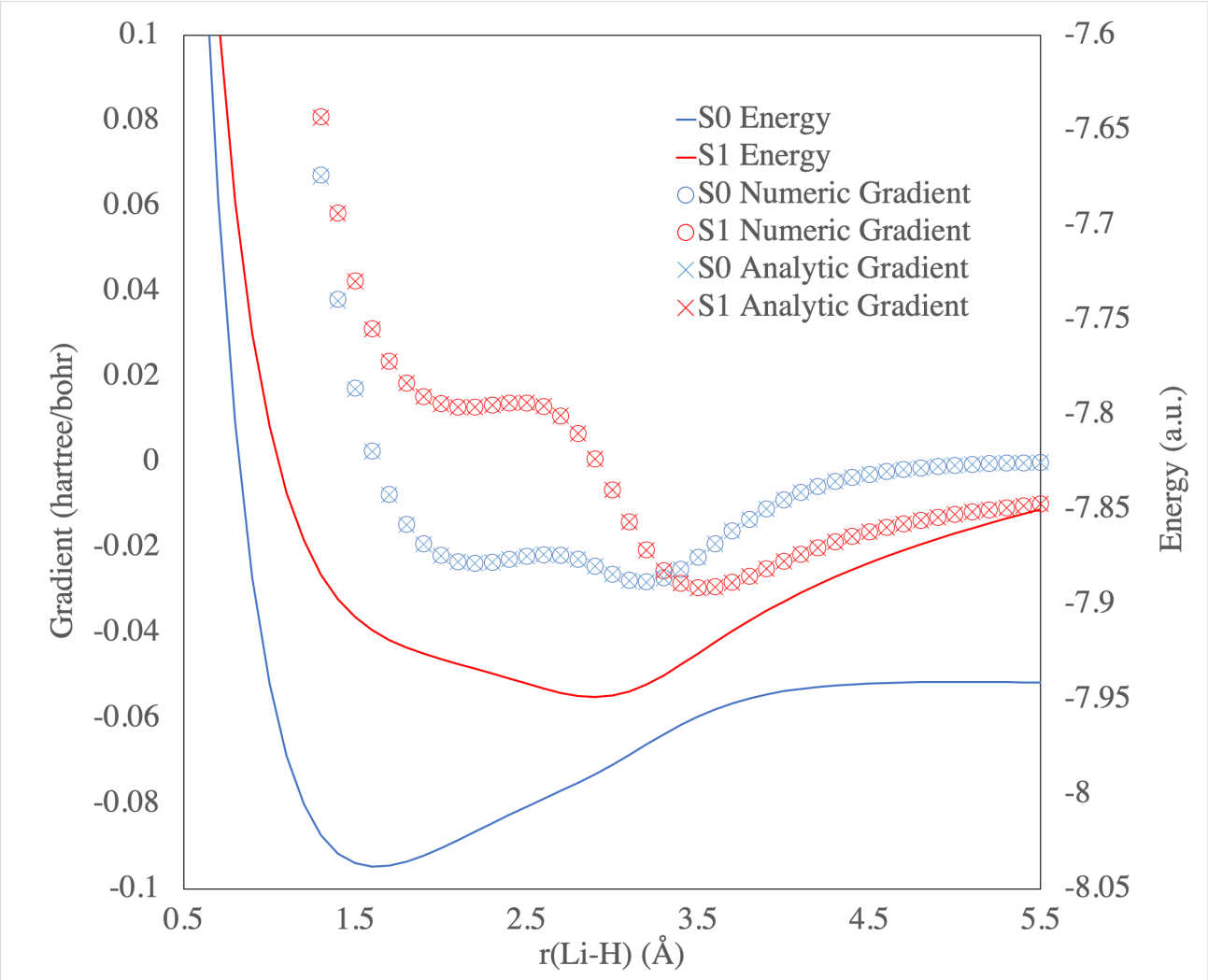

Figure 2.2: Potential energy surface (PES) scan of lithium hydride from a bond distance of 0.5 Å to 5 Å. The numeric and analytic gradients and energies for SA-PDFT are shown at each point on the PES is shown for both the ground, S_0 and excited, S_1 states.

also other factors such as basis set dependence. The geometries optimized with SS-PDFT are also included in the table, but little difference is observed between the SA- and SS-PDFT ground-state geometric parameters.

In order to include both the excited state and the ground state in the same state-averaged manifold in *OpenMolcas*, no spatial symmetry was enforced in the SA-PDFT and SA-CASSCF calculations. However, the geometries computed with CASPT2(12e,10o) and the single reference methods in Table 2.3 (CC2, CCSD, ADC(2), and CC3), imposed C_{2v} symmetry. Therefore, the energies and geometries were determined using a set of orbitals that are variational with respect to that state's energy and not an average energy. It should be noted that these results are taken from the work by Jacquemin[62] and it was observed that CC3 and CASPT2 with a large active space and diffuse basis set give geometries close to experiment.[62]

The lowest-lying $n \rightarrow \pi^*$ state of formaldehyde is known to deviate from a planar structure and to have a significantly lengthened carbonyl bond, and experimental values for the out-of-plane angle, η, vary from 20.5°[63] to 34.0°[64–66]. Here, 34° is taken as the reference value based on both experimental[65,66] and theoretical[62] work. Results computed with SA-PDFT have the second largest error for the puckering angle, η. The carbonyl bond distance for this state is 1.323 ± 0.002 Å[63–65] which is much longer than the ground state carbonyl bond length of 1.208 ± 0.001 Å[65,67]. Table 2.3 shows that SA-PDFT gives results in agreement with experiment for bond distances and the ∠H-C-H for the lowest lying excited singlet state of formaldehyde.

In Table 2.4, the adiabatic and vertical energetic gaps are reported for SA-PDFT, CASPT2, and SA-CASSCF. Vertical gaps are computed as the energy difference between the ground and excited state at the optimized ground-state geometry for that method. The adiabatic gaps correspond to the difference in energy computed at the optimized structures for both the excited and ground state for that method. The reference for the adiabatic gap is CC3[62] and the reference for the vertical gap is experiment[68]. Compared to CC3, the SA-PDFT adiabatic gap is 0.03 eV larger, and the CASPT2 one is 0.02 eV smaller, and SA-CASSCF is 0.01 eV larger. All methods shown here overestimate

Table 2.2: Ground-electronic-state equilibrium geometries of formaldehyde with the first row being experiment and the other rows being the difference from the experiment. Bond distances are reported in Å and angles are reported in degrees.

	C=O	C-H	∠H-C-H	η
Exp.[65]	1.208	1.116	116.3	0
SA-PDFT(12e,12o)	0.002	-0.002	-0.2	0
SS-PDFT(12e,12o)	0.001	-0.016	0.1	0
CASPT2(12e,10o)[62]	0.001	-0.014	-0.1	0
SA-CASSCF	0.006	-0.013	1.0	0
ADC(2)[62]	0.002	-0.020	0.2	0
CC2[62]	0.009	-0.018	0.1	0
CCSD[62]	-0.007	-0.019	0.1	0
CC3	0.000	-0.017	0.2	0

Table 2.3: Excited-electronic-state equilibrium geometries of formaldehyde with the first row being experiment and the other rows being the difference from the experiment. Bond distances are reported in Å and angles are reported in degrees.

	C=O	C-H	∠ H-C-H	η
Exp.[64]	1.323	1.098	118.4	34
SA-PDFT(12e,12o)	0.000	0.004	-0.8	-6
CASPT2(12e,10o)[62]	0.003	-0.008	-0.3	4
SA-CASSCF(12e,12o)	0.033	-0.019	-0.3	-2
ADC(2)[62]	0.057	-0.017	5.4	-15
CC2[62]	0.030	-0.013	2.9	-5
CCSD[62]	-0.023	-0.011	0.5	-3
CC3[62]	-0.003	-0.009	-0.2	3

Table 2.4: The excitation energies between the ground state and lowest lying excited state with $^1n \rightarrow \pi^*$ character in formaldehyde.

	ΔE (eV)	
Method	Adiabatic	Vertical Absorption
Exp[68]		3.79
CC3[62,69]	3.55	3.97
SA-PDFT(12e,12o)	3.58	3.92
CASPT2(12e,10o)[62]	3.53	3.98
SA-CASSCF(12e,12o)	3.56	4.04

the experimental vertical gap by more than 0.10 eV; but SA-PDFT and SA-CASSCF differ from the more expensive CASPT2 differ by only 0.06 eV.

Formaldehyde was studied in order to compare SA-PDFT geometries and energetics to other methods from the literature, but both the ground and first excited singlet states have single-reference character and thus it is not essential to use a multireference method. Next we consider *trans*-butadiene, which has considerable multireference character.

2.4.3 Trans-butadiene

To show the performance of SA-PDFT on a system with a multireference ground state, *trans*-butadiene was studied and compared to results by Watson and Chan[70]. Both the ground state and the 2^1A_g state of *trans*-butadiene are known to have strong multireference character based on their M diagnostics.[71]

The best estimate for the vertical gap has been reported as 6.39 ± 0.07 eV[70]. Multi-state CASPT2 (MS-CASPT2) at the experimental equilibrium geometry predicts the vertical gap to be 6.69 eV.[71] CASPT2 computed for a SA-CASSCF reference wave function with no state interaction is also an interesting comparison to SA-PDFT because SA-PDFT does not include state-interaction effects, therefore we compare to CASPT2 results as well as MS-CASPT2. The adiabatic, vertical absorption, and vertical de-excitation gaps are shown in Table 2.5.

SA-CASSCF predicts a vertical absorption gap closest to the best estimate but all methods

Table 2.5: The excitation energy (in eV) of the 2^1A_g states in *trans*-butadiene.

	ΔE (eV)		
Method	Adiabatic	Vertical Absorption	Vertical De-Excitation[a]
Best Estimate[70]		6.39	
MS-CASPT2		6.69	
CASPT2	5.68	6.68	-4.80
SA-PDFT	5.77	6.91	-4.72
SA-CASSCF	5.42	6.57	-4.47

[a] Difference between the Ground and 2^1A_g states at the 2^1A_g equilibrium geometry.

Table 2.6: Bond lengths and geometries of the 1^1A_g and 2^1A_g states *trans*-butadiene with the first set of values being the reference values and the other sets being differences from the reference values. The bond lengths are reported in angstroms (Å) and bond angles reported in degrees

	1^1A_g			2^1A_g		
Method	C=C	C-C	∠C-C=C	C-C	C=C	∠C-C=C
Exp.[72]	1.349	1.465	123.8			
CASPT2	-0.007	-0.011	-0.2	1.488	1.394	122.1
SA-PDFT	-0.013	0.005	0.3	0.008	0.003	2.0
SA-CASSCF	-0.004	-0.009	0.5	0.001	0.019	1.1

overestimate the gap by more than 0.15 eV. SA-PDFT is the furthest from this value with a difference of 0.52 eV. For the adiabatic gap, SA-PDFT is 0.09 eV different from the CASPT2 value while SA-CASSCF differs by 0.26 eV. The vertical de-excitation energy computed with SA-PDFT is 0.08 eV different from CASPT2 and SA-CASSCF is 0.33 eV different from CASPT2. The geometries predicted by these three methods for the ground and excited ^1A_g states of *trans*-butadiene are shown in Table 2.6.

For the ground state, all three methods predict geometric parameters that are similar to the reference values. The method with the largest deviation from the experimental value for the C-C bond length is CASPT2, for the ∠C-C=C angle is SA-CASSCF, and for the C=C bond lengths is SA-PDFT. In the excited state CASPT2, SA-PDFT and SA-CASSSCF are in excellent agreement.

2.4.4 Cytosine

In this section, we report the optimization of the geometries of the ground and excited states of cytosine; we compare the results to CCSD and MS-CASPT2 computations reported by Fogarasi[73] and Nakayama[2], respectively. Cytosine shows the efficiency of SA-PDFT compared with CASPT2 in handling conjugated systems with midsize active spaces. The geometry was optimized with the (14e, 10o) active space which contains the occupied π space, two lone pair orbitals, and three correlating π^* orbitals, and has shown to be accurate in previous work.[74–76] In the SA-PDFT and CCSD/TZP[73] geometry optimizations, C_s symmetry was used, and the three lowest $^1A'$ states were considered. For direct comparison to the SA-PDFT results, cytosine was also optimized with SA(3)-CASSCF(14e,10o) and CASPT2(14e,10o), with the same state-averaged reference wave function as used for the SA-PDFT computation. Atomic labels on cytosine are shown in Figure 2.3 for use in tabulating and discussing the results. (Tables 2.7 - 2.9).

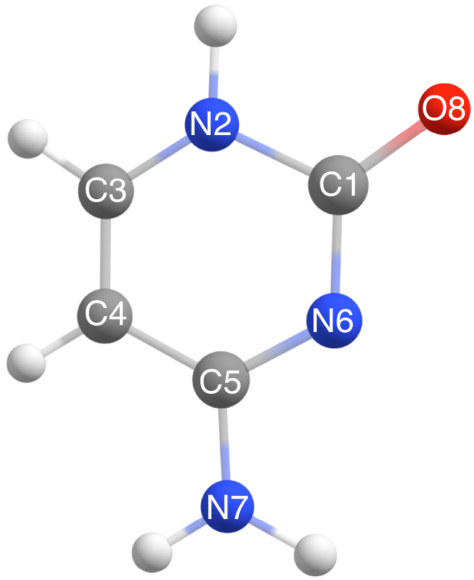

Figure 2.3: The ground-state geometry of cytosine as optimized by SA(3)-PDFT.

In Tables 2.7 and 2.8, the ground-state geometries of cytosine computed with SA(3)-CASSCF, SA(3)-PDFT, CASPT2(14e,10o), and CCSD are compared to experiment. The computational entries in these tables are reported as differences with respect to the experimental reference geometry. The SA-PDFT method reproduces the experimental geometry to within 0.06 Å. In some instances, namely the C1-N2 and N2-C3 bond lengths, SA(3)-PDFT performs slightly worse than CCSD and CASPT2(14e,10o). The C1-N2 bond length predicted by SA(3)-PDFT is 0.02 Å longer than the one predicted by CCSD and CASPT2(14e,10o), 0.049 Å longer than the SA(3)-CASSCF result, and a total of 0.066 Å longer than experiment. For the N2-C3 bond length, SA-PDFT predicts this parameter to be 0.02 Å shorter than experiment, whereas the CCSD and CASPT2(14e,10o) values are approximately 0.01 Å longer than experiment. The SA(3)-CASSCF results also predict a slightly shorter N2-C3 bond distance than experiment. For other carbon-nitrogen bonds, SA(3)-PDFT gives results similar or closer to experiment than the other methods, as reported in Table 2.7. The C5-N6 and C5-N7 bonds computed with SA(3)-PDFT have an error 50% smaller compared to CCSD and CASPT2(14e,10o). The N6-C1 bond length computed with SA(3)-PDFT correctly reproduces the experimental length by up to three decimal places. The SA(3)-CASSCF and SA(3)-PDFT results both over- or underestimate the experimental geometry for each bond distance for cytosine, which results in the same sign of error in each case in Table 2.7. The computed ground state cytosine bond lengths are very similar to the experimental values; each method reported in Table 2.7 (SA(3)-CASSCF(14e,10o), CCSD, CASPT2(14e,10o), and SA(3)-PDFT) has a MUD of 0.02 Å.

Table 2.8 reports the SA(3)-CASSCF, CCSD, CASPT2(14e,10o) and SA(3)-PDFT bond angle deviations with respect to the experimental values. All methods have a similar magnitude of error, except for a few angles with larger error from SA(3)-PDFT results. The MUD for SA(3)-CASSCF is 0.9°, CCSD is 1.3°, CASPT2(14e,10o) is 1.4°, and SA(3)-PDFT is 1.6°. Along with the bond distance analysis above, these data show that SA(3)-PDFT provides a similar accuracy for ground state geometry optimization as CASPT2(14e,10o) and CCSD.

Table 2.7: Experimental bond distances (first row, in Å) of the ground state of cytosine and differences of theoretical values from experiment

Method	C1-N2	N2-C3	C3-C4	C4-C5	C5-N7	C5-N6	N6-C1	C1-O8	MUD
Exp.[77]	1.374	1.357	1.342	1.424	1.330	1.337	1.364	1.234	-
SA(3)-CASSCF(14e,10o)	0.017	-0.003	0.004	0.022	0.020	-0.046	0.027	-0.038	0.02
CCSD[73]	0.042	0.003	0.011	0.022	0.027	-0.024	0.015	-0.020	0.02
CASPT2(14e,10o)	0.046	0.005	0.015	0.019	0.030	-0.017	0.014	-0.012	0.02
SA(3)-PDFT(14e,10o)	0.066	-0.017	0.016	0.012	0.021	-0.011	0.000	-0.019	0.02

Table 2.8: Experimental bond angles (first row, in degrees) of the ground state of cytosine and differences of theoretical values from experiment

Method	∠6-1-2	∠5-6-1	∠4-5-6	∠3-2-1	∠3-4-5	∠4-3-2	∠8-1-2	∠8-1-6	∠7-5-6	∠7-5-4	MUD
Exp.[77]	118.1	119.9	122.0	122.7	117.3	120.1	119.8	122.2	118.2	119.9	
SA(3)-CASSCF(14e,10o)	-1.2	0.6	1.4	0.4	-1.1	-0.2	-0.2	1.4	0.2	-1.8	0.9
CCSD[73]	-1.6	-0.2	2.5	0.8	-1.5	-0.1	-1.1	2.6	-1.0	-1.6	1.3
CASPT2(14e,10o)	-1.8	-0.2	2.7	1.0	-1.6	-0.2	-1.1	2.8	-1.3	-1.5	1.4
SA(3)-PDFT(14e,10o)	-2.3	0.6	2.0	0.7	-1.6	-0.5	-2.3	4.5	-1.8	-0.4	1.6

Table 2.9: CASPT2(14e,10o) computed bond distances (first row, in Å) of the first singlet excited state of cytosine and differences of subsequent theoretical values from CASPT2(14e,10o).

Method	C1-N2	N2-C3	C3-C4	C4-C5	C5-N7	C5-N6	N6-C1	C1-O8	MUD
CASPT2(14e,10o)	1.453	1.301	1.394	1.444	1.350	1.320	1.374	1.210	
SA(3)-CASSCF(14e,10o)	-0.095	0.080	0.030	-0.079	0.022	0.097	-0.100	0.118	0.08
MS(2)-CASPT2(8e,7o)[2]	-0.043	0.075	0.036	-0.053	0.047	0.031	-0.049	0.066	0.05
SA(3)-PDFT(14e,10o)	-0.024	0.081	0.022	-0.059	0.019	0.096	-0.032	0.026	0.04

The geometry of the first singlet excited state of cytosine was optimized with SA(3)-CASSCF, SA(3)-PDFT, and CASPT2(14e,10o). The reference CASPT2(14e,10o) computation used the same active space and number of roots as the SA(3)-PDFT computation. A previous study on the excited states of cytosine provided a MS(2)-CASPT2(8e,7o) optimized geometry, which is used here as another set of structural parameters to compare to.[2] The active space used was (8e, 7o), and was composed of only π and π^* orbitals. Only two roots were considered in the geometry optimization and the DZP basis set was used. Each excited state geometry reported in Table 2.9 is of $^1\pi\pi^*$ character, with a final electronic state of $^1\mathrm{A}'$.

The excited state optimized structure is very similar across all methods. The deviations from CASPT2(14e,10o) of MS(2)-CASPT2(8e,7o) and SA(3)-PDFT are of similar magnitude. However, the SA(3)-PDFT geometries deviate slightly in some cases. The SA(3)-CASSCF geometries have the same error or deviate more with respect to the reference geometry than that of SA(3)-PDFT. This shows that SA(3)-PDFT improves the first excited state geometry of cytosine as compared to SA-CASSCF and ultimately results in a structure closer to that of CASPT2. The MUD from the CASPT2(14e,10o) excited structure is 0.04 Å for the SA(3)-PDFT results, which is smaller than that of MS(2)-CASPT2(8e,7o) at 0.05 Å and SA(3)-CASSCF at 0.08 Å.

2.5 Conclusion

In this work, SA-PDFT analytic gradients were derived and implemented using a Lagrangian framework. This is a generalization of the SS-PDFT analytic gradients previously available in *OpenMolcas*. A test set of four molecules was studied in order to assess the correctness and accuracy of the SA-PDFT gradients, excitation and emission energies, and geometries.

Comparison to numeric gradients for the potential energy curve of LiH and additional comparisons for formaldehyde and *trans*-butadiene showed that SA-PDFT analytic gradients closely agree with numeric SA-PDFT gradients in both the ground state and first singlet excited state.

The geometries computed with SA-PDFT are comparable to those computed with CC2, CCSD,

CC3, and CASPT2. Analytical gradients for SA-PDFT provide an avenue for the study of excited geometries and excitation energies in systems that are prohibitively expensive when using other post-CASSCF methods. The results presented in this work clearly show SA-PDFT gives results with similar accuracy to CASPT2 for ground and excited state properties of small organic molecules at an attractive computational cost. In future studies, in order to efficiently optimize geometries of larger molecules, the SA-PDFT gradient expressions will be modified to make use of the density fitting[78,79] approximation to speed up the two-electron integrals.

Reproduced with permission from 1.

CHAPTER 3

ANALYTIC GRADIENTS FOR MULTICONFIGURATION PAIR-DENSITY FUNCTIONAL THEORY WITH DENSITY FITTING: DEVELOPMENT AND APPLICATION TO GEOMETRY OPTIMIZATION IN THE GROUND AND EXCITED STATES

3.1 Introduction

The computation of the 4-index electron-repulsion integrals (ERIs) and their transformation into the atomic-orbital basis is a major bottleneck of gradient and energy calculations, as the steps involved in computing and manipulating the ERIs scale as the fourth power of basis set size (for a fixed molecular size).[80] By using density fitting (DF) procedures one can reduce the cost of these steps by 1–2 orders of magnitude. Various in-depth analyses of this procedure have been reported.[80–85] Here, we use the DF techniques reported by Delcey at al.[78] for SA-CASSCF analytic gradients and apply them to MC-PDFT analytic gradients.

Cholesky decomposition (CD) approximates the 4-center ERIs by expressing them as a product of 3-center tensors to reduce the storage requirements of the molecular integrals as well as the cost of their manipulation. Using DF, the CD is written as

$$g_{\nu\sigma}^{\mu\kappa} \equiv (\mu\nu|\kappa\sigma) \equiv \langle\mu(1)\kappa(2)|\,\frac{1}{r_{12}}\,|\nu 1\sigma(2)\rangle \approx \sum_{K=1}^{M}\sum_{L=1}^{M} C_{\mu\nu}^{K}(K|L)C_{\kappa\sigma}^{L} \tag{3.1}$$

where is a generic two-electron integral. The Greek indices represent atomic orbitals, L and K represent auxiliary basis functions from the Cholesky basis, (K|L) is the Coulomb repulsion in the auxiliary basis, M is the number of auxiliary basis functions in the Cholesky basis, and are

coefficients that are obtained by the equation

$$C^L_{\mu\nu} = \sum_K (\mu\nu|K)(K|L)^{-1} \tag{3.2}$$

In our study the atomic compact Cholesky decomposition (acCD)[86] as developed in OpenMolcas[48] is used, but the following discussion on analytical gradients with density fitting can be applied to any set of differentiable auxiliary basis functions.

In both SS-CAS-PDFT and SA-CAS-PDFT, the energy is not variational with respect to the orbitals and configuration interaction coefficients. The standard approach for analytical evaluation of molecular gradients for nonvariational quantum-chemical theories, such as MC-PDFT, is to use Lagrange's method of undetermined multipliers, which defines a Lagrangian function with a value that is identical to that of the total energy but that has vanishing first derivatives with respect to all parameters. Obtaining this Lagrangian involves solving a set of differential equations for the Lagrange multipliers as described in Sand et al.[21] for SS-CAS-PDFT and in Scott et al.[1] for SA-CAS-PDFT; the modification of this to apply the DF approximation is straightforward. Once the Lagrange multipliers are on hand, the molecular gradient is obtained by differentiating the Lagrangian function with respect to nuclear coordinates; this is facilitated by the observation that all partial derivatives of the Lagrangian with respect to either wave function parameters or Lagrange multipliers vanish by construction.

The on-top energy is the energy of the on-top pair-density-functional term in MC-PDFT[87] (it is analogous to the exchange-correlation energy of Kohn–Sham DFT (KS-DFT) and is so named because it is a functional of ρ and Π, the electronic density and the on-top pair density at a point in space, and ρ' and Π', their gradients (unlike the exchange-correlation energy of KS-DFT which is a functional of the spin-up and spin-down electron densities, their gradients, and possibly other ingredients, depending on the approximate functional). The programmable equations of the effective-density matrices are given by Eqs. 2.39 and 2.40 of the previous chapter. The density-fitting approximation for the ERIs is obtained by transforming $C^L_{\mu\nu}$ from the atomic orbital

basis (μ,ν) to the molecular orbital basis (p,q) using standard techniques, substituting into equation (3.1), and simplifying. This yields

$$g^{pr}_{qs} = (pq|K)(K|L)^{-1}(L|rs) \tag{3.3}$$

The OpenMolcas[48] implementation of the differentiation of Eq. (3.3) with respect to nuclear coordinates is similar to the one presented by Delcey et al.[78] for SA-CASSCF, except that (i) the bare 2-body density matrix is replaced by the product of two one-body density matrices ($d^{pr}_{qs} \rightarrow D^{p}_{q}$ D^{r}_{s}) (ii) the present formulation involves the on-top density rather than the SA-CASSCF energy expression.

MC-PDFT with density fitting is implemented in the OpenMolcas[48] software package and the PySCF[50] add-on package mrh. Gradients and optimized geometries using this method have been computed for formaldehyde, ethylene, acrolein, p-hydroxybenzylidene-imidazolinon-5-one (pHBDI), cytosine, and rhodopsin. Each of these systems is involved in photochemical reactions, and they have been studied previously using SA-CASSCF and in some cases with complete active space perturbation theory through second order[88,89] (CASPT2). We validate the accuracy of the newly implemented density fitting for each of these systems and assess the accuracy of the gradients and optimized geometries by comparison to MC-PDFT without density fitting and to CASPT2. We also report on the timing reduction when using density fitting with SA-CAS-PDFT (which is MC-PDFT applied with an SA-CASSCF reference state) and when using three different grid sizes for the numerical quadrature in the evaluation of the energy expression.

3.2 Computational Methods

All MC-PDFT calculations were performed using local versions of OpenMolcas[48] and using the tPBE[87] on-top functional. No symmetry constraints were used. Three grid sizes – coarse, fine, and ultrafine – were used in the MC-PDFT calculations. The coarse grid has 35 radial shells

and 110 angular points per shell, labelled as (35,110). The fine (75,302) and ultrafine (99,590) grids were also used in this study. The Baker geometry optimization convergence criteria[90] were used, setting the energy change threshold to $1x10^{-6}$ a.u. and the norm of the gradient threshold to $3x10^{-4}$ a.u. Only singlet states were studied in this work, and the six systems studied are shown in Figure (3.1).

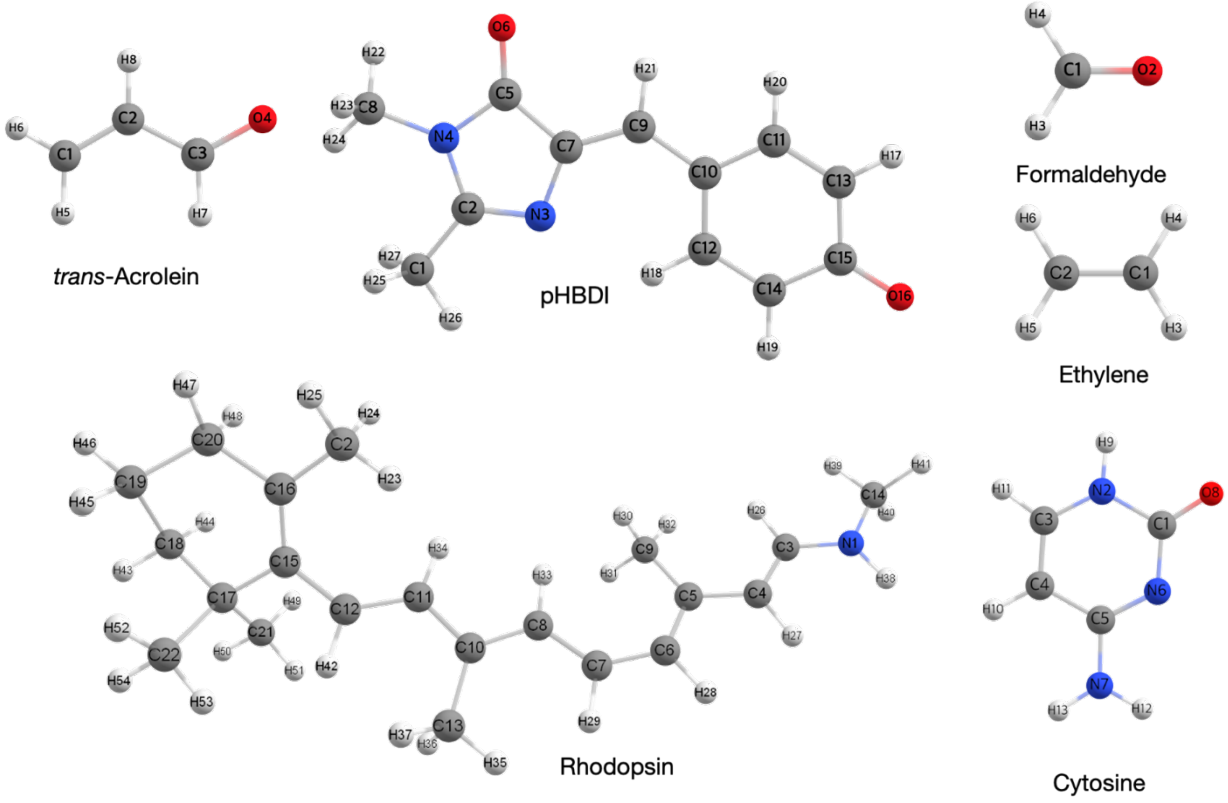

Figure 3.1: Systems studied to verify the analytic gradients.

The active space of formaldehyde is composed of the σ(C-H), σ(C=O), and π(C=O) bonding and anti-bonding orbital pairs. For ethylene, we include the π and π^* orbitals in the active space. The active space for acrolein includes the occupied π orbitals and correlating π^* orbitals with a doubly occupied lone pair orbital localized on the O atom. The active space for cytosine includes

the entire occupied π space and lone-pair orbitals with three correlating π^* orbitals. The active space for pHBDI consists of two conjugated π orbitals delocalized on the 5- and 6-member rings and one antibonding π orbital delocalized across the bond between the rings. The active space used in the case of rhodopsin is the full π space with correlating π^* orbitals. Active space sizes, number of configuration state functions, number of states included in the state average, and grid size for all these molecules are shown in Table 3.1. Basis set information is reported in Table 3.2.

Molecule	Active Space	N[a]	CSFs[b]	Grid Size
Formaldehyde	(6e, 6o)	2	175	Ultrafine
Ethylene	(2e,2o)	1	3	Ultrafine
Acrolein	(6e,5o)	2	50	Ultrafine
Cytosine	(14e,10o)	3	2,598	Coarse, Fine, and Ultrafine
pHBDI	(4e,3o)	2	6	Coarse, Fine, and Ultrafine
Rhodopsin	(12e,12o)	2	226,512	Coarse, Fine, and Ultrafine

Table 3.1: Details of SA-CAS-PDFT calculations. [a]Number of States in the average. [b]Number of configuration state functions.

3.3 Results and Discussion

In the three following subsections we assess the performance of the implementation as compared to SA-CAS-PDFT without density fitting and to other methods with respect to 1) the accuracy of the gradients 2) the agreement between optimized molecular structures and 3) the reduction of computational time.

3.3.1 Correctness of the SA-CAS-PDFT Gradients with Density Fitting

The acCD auxiliary basis sets used in the Cholesky-based density fitting procedure presented here are unbiased and tunable because they are derived *ab initio* and with strict integral-error control.[91] Therefore, in the following section we do not analyze the numerical accuracy of the approximate ERI. Instead, we only analyze the quality of the gradients and the optimized geometries.

To validate the correctness of the MC-PDFT gradients computed with density fitting, a comparison between the gradient computed with and without density fitting is reported for each system in Figure (3.2) and Table 3.2. The gradient was computed both ways at the same geometry and the percent difference between the norm of the gradient for each atom was computed. The errors are comparable to those in density-fitted calculations with other electronic structure methods, for example a maximum error of 0.9% for a density-fitted SA-CASSCF calculation on a ruthenium nitrosyl complex and a 6.1% maximum error for a density-fitted Kohn-Sham calculation with the BP86 exchange-correlation functional on the same system.[92] For all molecules studied in this work, the mean relative error is less than 1.1% at all grid sizes. The median error is less than 0.6% in all cases and the maximum error is at most 5.6%. This shows that the density-fitted MC-PDFT gradients implemented here are as accurate as the density-fitted SA-CASSCF and density-fitted BP86 gradients implemented in OpenMolcas. The maximum relative error, 5.6% for rhodopsin using a coarse grid, is significantly improved when the grid size is increased from coarse to fine (5.6% to 1.7%), but no significant accuracy improvement is obtained by increasing the grid from fine to ultrafine (1.7% either way). Increasing the basis set size from 137 contracted basis functions (cc-pVDZ) to 310 (cc-pVTZ) for cytosine gives a substantial increase in the accuracy of the gradients predicted by density-fitted MC-PDFT. This is in line with the acCD procedure where the auxiliary basis set is a function of the valence basis set, and, as the valence basis set is getting saturated, the same goes for the auxiliary basis set. Hence, as the valence basis set is saturated, the DF error is reduced.

Using rhodopsin as an example, we analyze the effect on the gradient of reducing the grid size from ultrafine to coarse; Figure 3.2 shows that there is a dramatic change. However, the difference in the percent error between the ultrafine and fine grids is very small. The largest errors are generally found for the gradient components of the heavier atoms, and some of the components are significantly harder to converge than others. For example, at C9 (Figure 1) the error is only reduced from 2.3% to 1.2% while the error at H24 is reduced from 5.1% to 0.2% when changing

Molecule	Basis Set[a]	Grid	% Error Mean	% Error Median	% Error Max
Formaldehyde	aug-cc-pVTZ (138)	Ultrafine	0.070	0.005	0.500
Trans-acrolein	aug-cc-pVTZ (176)	Ultrafine	0.002	0.001	0.005
Ethylene	aug-cc-pVTZ (184)	Ultrafine	0.018	0.015	0.034
Cytosine	cc-pVTZ (310)	Coarse	0.002	0.001	0.005
		Fine	0.002	0.001	0.005
		Ultrafine	0.002	0.001	0.005
	cc-pVDZ (137)	Coarse	0.020	0.010	0.120
		Fine	0.020	0.010	0.110
		Ultrafine	0.020	0.010	0.110
pHBDI	cc-pVDZ (279)	Coarse	0.080	0.030	0.360
		Fine	0.080	0.030	0.370
		Ultrafine	0.090	0.030	0.410
Rhodopsin	cc-pVDZ (468)	Coarse	1.050	0.530	5.570
		Fine	0.340	0.230	1.670
		Ultrafine	0.340	0.220	1.680
Overall		Coarse	0.288	0.020	5.570
		Fine	0.111	0.020	1.670
		Ultrafine	0.090	0.023	1.680

Table 3.2: The mean, median, and maximum relative error of the MC-PDFT atomic components of the gradients computed with density fitting to those computed without density fitting. [a]Number in parentheses is number of contracted basis functions

from a coarse to ultrafine grid. Overall, the relative error per atom for rhodopsin is reasonable (less than 6.0% for all atoms). The difference in computation time when using the three grid sizes is the main motivation behind the comparisons in Table (3.2) and Figure 3.2, and this is discussed further in Subsection 3.3.3.

3.3.2 Optimized Geometries

In this subsection optimized minimum-energy structures calculated by MC-PDFT without and with density fitting are compared to further validate the accuracy of the density-fitted MC-PDFT approach; we also compare to SA-CASSCF and CASPT2 geometries (all SA-CASSCF and SA-CASPT2 calculations from ref[1] are performed with Cs symmetry). In addition, we investigate

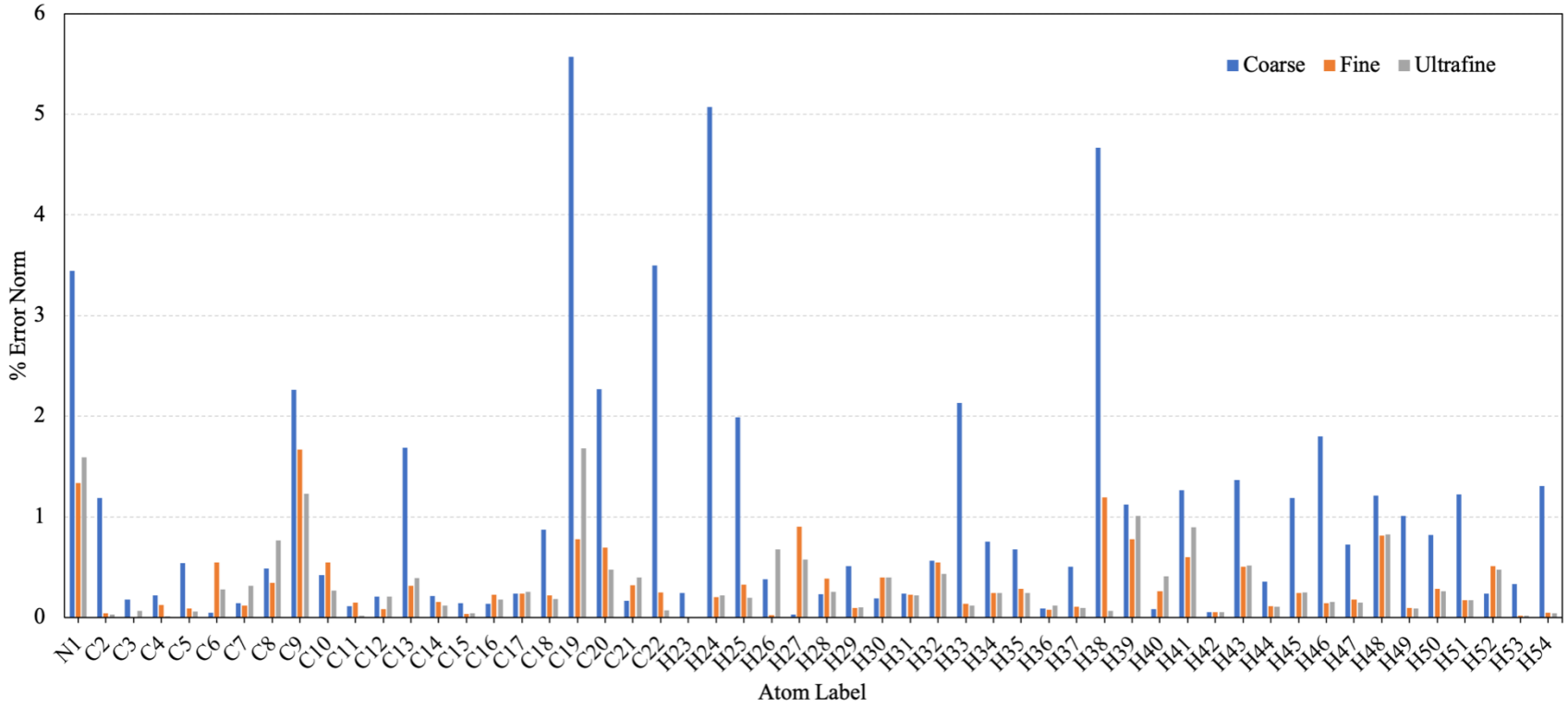

Figure 3.2: The relative error of the norm of the gradient on each atom of rhodopsin in the density-fitted MC-PDFT calculation as compared to that in the calculation without density fitting. Coarse, fine, and ultrafine grid size results are in blue, orange, and gray respectively.

the impact of grid size on the optimized geometries by using the coarse, fine, and ultrafine grid sizes available in *OpenMolcas*.

First, we consider calculations for the ground state and first excited singlet state of cytosine; these calculations are presented in Tables 3.3 - 3.6. The atom labels for cytosine used in these tables are shown in Figure 2.1.

Tables 3.3 and 3.4 shows that for the ground state of cytosine, the mean unsigned deviation (MUD) of SA-CAS-PDFT bond lengths and bond angles from experiment with the ultrafine grid is 0.027 Å and 1.9 deg without density fitting and 0.026 Å and 1.5 deg with density fitting. Changing the grid does not change the MUD of bond lengths and changes the MUD of bond angles by only 0.2 deg. Overall, the introduction of density fitting or changing of the grid leads to only small differences in the deviations from experiment. Optimized structures from all methods agree reasonably well with the experimentally predicted structures for the ground state.

Tables 3.5 and 3.6 for the first singlet excited state of cytosine use the CASPT2 structure as the reference. The MUDs for SA-CAS-PDFT, with or without density fitting (DF), are at most 0.060 Å for bond lengths and 3.6 deg for bond angles. Moving to a larger basis set would likely reduce these deviations as suggested by Table 3.2, where the norm of the gradients for DF was more accurate with the cc-pVTZ basis set than with the cc-pVDZ basis set.

Next, we consider calculations for pHBDI. Figure 3.3 compares bond lengths optimized with density-fitted SA-CAS-PDFT and the ultrafine grid to those obtained by XMS-CASPT2.[93] The geometries are very similar, with the largest deviation in a bond length being only 0.008 Å, and the MUD of density-fitted SA-CAS-PDFT with respect to XMS-CASPT2 only 0.004 Å. The bond angles are also similar with an MUD of 0.3 deg. The MUDs for the coarse and fine grids are respectively 0.009 Å and 0.008 Å for bond lengths and 0.5 deg and 0.3 deg for bond angles. Optimizations using the fine and ultrafine grids give almost identical structures for pHBDI. The results

	grid[a]	DF	C1-N2	N2-C3	C3-C4	C4-C5	C5-N7	C5-N6	N6-C1	C1-O8	MUD
Experiment[77]	-	1.374	1.357	1.342	1.424	1.330	1.337	1.364	1.234	-	
SA-CASSCF[1]	-	no	1.391	1.354	1.346	1.446	1.350	1.291	1.391	1.196	0.022
SA-CAS-PDFT	U	no	1.452	1.342	1.368	1.451	1.357	1.324	1.373	1.212	0.027
SA-CAS-PDFT	U	yes	1.439	1.351	1.357	1.460	1.364	1.324	1.383	1.215	0.026
SA-CAS-PDFT	F	yes	1.439	1.351	1.357	1.461	1.364	1.324	1.383	1.215	0.026
SA-CAS-PDFT	C	yes	1.440	1.351	1.357	1.461	1.363	1.325	1.382	1.215	0.026
SA-CASPT2[1]	-	no	1.420	1.362	1.357	1.443	1.360	1.320	1.378	1.222	0.020

Table 3.3: Bond lengths (Å) of the singlet ground state of cytosinea with and without density fitting (DF). [a]Grids are ultrafine (U), fine (F), and coarse (C). All optimized geometries except CASPT2 are calculated with the cc-pVDZ basis set. The SA-CASPT2 geometry optimizations were performed using the 6-311G+(2df) basis set. The last column is the mean unsigned deviation from experiment.

	grid	DF	6-1-2	5-6-1	4-5-6	3-2-1	3-4-5	4-3-2	8-1-2	8-1-6	7-5-6	7-5-4	MUD
Experiment[77]	-	-	118.1	119.9	122	122.7	117.3	120.1	119.8	122.2	118.2	119.9	-
SA-CASSCF[1]	-	no	116.9	120.5	123.4	123.1	116.2	119.9	119.6	123.6	118.4	118.1	0.9
SA-CAS-PDFT	U	no	115.1	120.9	124.1	124.0	115.6	120.2	117.7	127.2	117.3	118.6	1.9
SA-CAS-PDFT	U	yes	115.9	120.1	124.1	123.8	115.9	120.2	117.9	126.2	117.8	118.1	1.5
SA-CAS-PDFT	F	yes	115.9	120.1	124.1	123.8	115.9	120.2	117.9	126.1	117.8	118.1	1.5
SA-CAS-PDFT	C	yes	115.6	120.2	124.2	124.0	115.6	120.3	117.9	126.5	117.3	118.5	1.7
SA-CASPT2[1]	-	no	116.3	119.7	124.7	123.7	115.7	119.9	118.7	125.0	116.9	118.4	1.4

Table 3.4: Bond angles (deg) of the singlet ground state of cytosinea with and without density fitting (DF).[a]Grids are ultrafine (U), fine (F), and coarse (C). All optimized geometries except CASPT2 are calculated with the cc-pVDZ basis set. The SA-CASPT2 geometry optimizations were performed using the 6-311G+(2df) basis set and the SA-CASSCF calculations were performed with the aug-cc-pVTZ basis set. The last column is the mean unsigned deviation from experiment.

	grid	DF	C1-N2	N2-C3	C3-C4	C4-C5	C5-N7	C5-N6	N6-C1	C1-O8	MUD
CASPT2[1]	-	no	1.453	1.301	1.394	1.444	1.350	1.320	1.374	1.210	-
SA-CASSCF[1]	-	no	1.358	1.381	1.424	1.365	1.372	1.417	1.274	1.328 7 0.06	
MS-CASPT2[2]	-	no	1.410	1.376	1.430	1.391	1.397	1.351	1.325	1.276	0.04
SA-CAS-PDFT	U	no	1.425	1.398	1.419	1.383	1.380	1.440	1.320	1.271	0.06
SA-CAS-PDFT	U	yes	1.398	1.405	1.388	1.395	1.393	1.423	1.321	1.293	0.05
SA-CAS-PDFT	F	yes	1.357	1.431	1.387	1.400	1.379	1.416	1.295	1.368	0.06
SA-CAS-PDFT	C	no	1.417	1.397	1.419	1.386	1.382	1.436	1.317	1.275	0.05

Table 3.5: Bond lengths (Å) of the first excited singlet state of cytosinea with and without density fitting (DF). [a]Grids are ultrafine (U), fine (F), and coarse (C). The last column shows the mean unsigned deviation from CASPT2. The SA-CASPT2 geometry optimizations from ref[1] were performed using the 6-311G+(2df) basis set and the SA-CASSCF calculations from ref[1] are performed with the aug-cc-pVTZ basis set. The MS-CASPT2 geometries are taken from ref[2], where they were optimized using the Sapporo-DZP basis set. Only bond lengths were available for the MS-CASPT2 geometries.

	DF	Grid	6-1-2	5-6-1	4-5-6	3-2-1	3-4-5	4-3-2	8-1-2	8-1-6	7-5-6	7-5-4	MUD
CASPT2[1]	no	-	118.1	119.1	122.8	123.4	118.4	118.3	116.7	125.2	119.0	118.3	-
SA-CASSCF[1]	no	-	126.6	116.1	121.6	119.8	119.6	116.4	112.1	121.2	112.7	125.8	4.2
SA-CAS-PDFT	no	U	123.4	117.2	121.6	119.7	120.0	117.9	113.8	122.8	111.6	126.7	3.6
SA-CAS-PDFT	yes	U	123.8	116.7	121.3	120.3	120.6	117.3	114.8	121.4	112.8	125.7	3.5
SA-CAS-PDFT	yes	F	123.8	114.6	121.7	118.4	120.7	116.2	114.0	117.7	113.2	125.2	3.4
SA-CAS-PDFT	yes	C	123.3	117.2	121.7	120.5	120.0	117.2	114.4	122.3	111.9	126.3	3.4

Table 3.6: Bond angles (deg) of the singlet ground state of cytosinea with and without density fitting (DF).[a]Grids are ultrafine (U), fine (F), and coarse (C). All optimized geometries except CASPT2 are calculated with the cc-pVDZ basis set. The SA-CASPT2 geometry optimizations were performed using the 6-311G+(2df) basis set and the SA-CASSCF calculations were performed with the aug-cc-pVTZ basis set. The last column is the mean unsigned deviation from experiment.

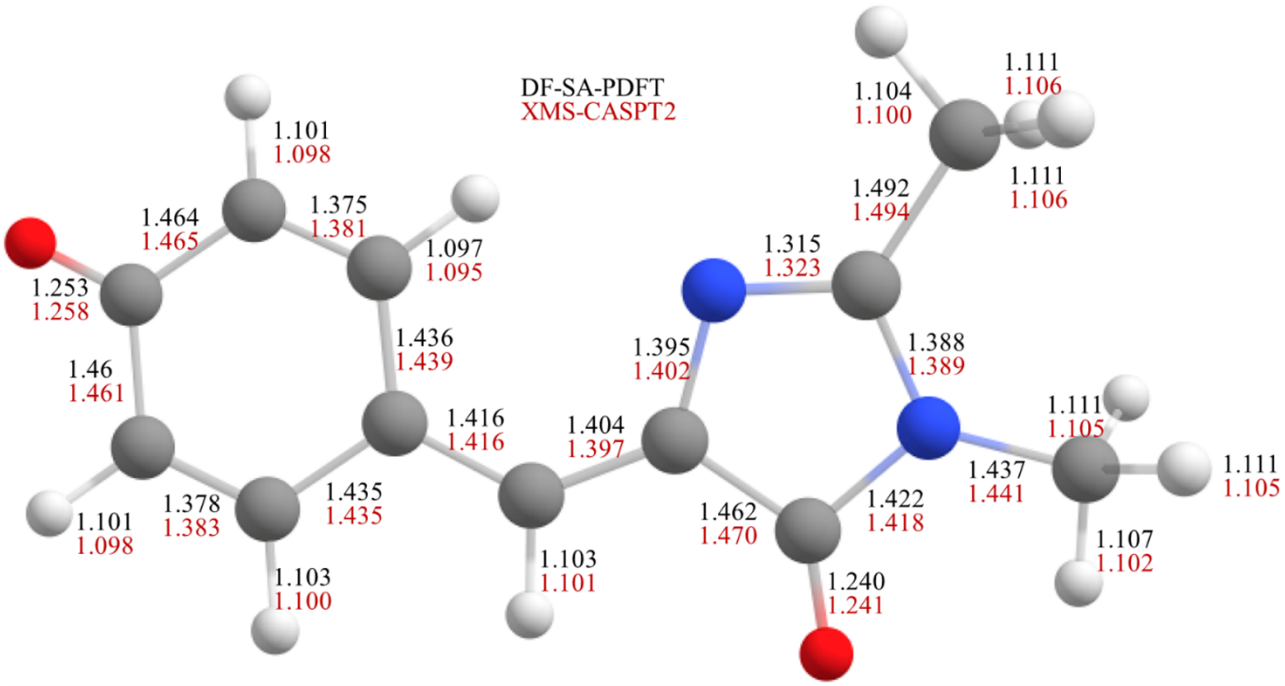

Figure 3.3: Bond lengths, in Å, of pHBDI optimized by density-fitted SA-CAS-PDFT with the ultrafine grid (black) and optimized by XMS-CASPT2 (red). Both are computed with the cc-pVDZ basis set.

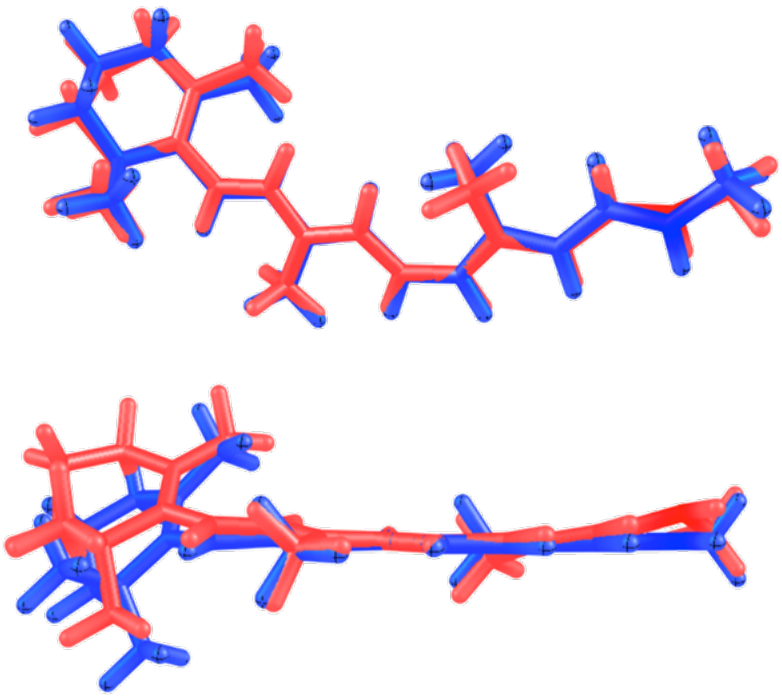

Figure 3.4: Overlay of rhodopsin structures optimized with XMS-CASPT2 (blue) and density-fitted SA-CAS-PDFT (red).

for pHBDI and cytosine show that grid size does not have a large effect on geometry accuracy for MC-PDFT.

Finally, we consider our largest system, rhodopsin and the overlay of rhodopsin structures optimized with density-fitted SA-CAS-PDFT and XMS-CASPT2[94] with a cc-pVDZ basis set is shown in Figure 3.2. The overlay was chosen with respect to the best fit along the carbon chain. The MUDs of these two sets of structural parameters are 0.009 Å and 1.1 deg. The optimized structures of density-fitted SA-CAS-PDFT and XMS-CASPT2 are given in the SI.

3.3.3 Timing

The timings for all OpenMolcas modules that had significant speed-ups when using density-fitted SA-CAS-PDFT are reported in Figure 3.5; these include integral (which computes the integrals in

the density fitting procedure), gradient (which computes that derivative of the Lagrangian for MC-PDFT), linear response (which computes the Lagrange multipliers), and energy (which computes the SA-CAS-PDFT energy and some effective potentials). For this timing analysis, we include one energy and one gradient calculation at the same geometry for all basis sets and grid sizes. These computations were run on one Intel Haswell E5-2680v3 processor with 20 GB of memory and the OpenMolcas program version 18.09 with the tag 1640-g3ea5c59.

Figure 3.5 shows that with the larger basis set, the computation of the ERIs is a major bottleneck in the fine and coarse grid calculations. With DF, the time spent in the integral module is no longer the bottleneck, and the numerical quadrature becomes the bottleneck in the fine and coarse grids. With the ultrafine grid, the quadrature portion of the gradient and energy modules is the bottleneck with both basis sets. In coarse-grid calculations, Figure 3.5a), the non-quadrature portion of the gradient and energy modules are faster with DF than without (5 times faster with cc-pVTZ and 2 times faster with cc-pVDZ), and similar speed-ups occur in the fine and ultrafine calculations. In the cc-pVDZ basis set for each grid size the longest steps are the quadrature portions of the energy and gradient modules. With both density fitting and conventional ERIs the integral step takes less than a minute with the cc-pVDZ basis set for all grid sizes.

For rhodopsin, the geometry optimization could only be completed with density-fitted SA-CAS-PDFT and the coarse grid. Without density-fitting, the full geometry optimization of this system had only completed a few gradient iterations after one week with the following resources: one Intel Haswell E5-2680v3 processor with 30 GB of memory and the OpenMolcas program version 18.09 with the tag 1640-g3ea5c59. Increasing the grid size also made the quadrature portions of the energy and gradient modules considerably longer. With density-fitting and the coarse grid, one gradient iteration for rhodopsin took 8 hours and 48 min. using the same resources.

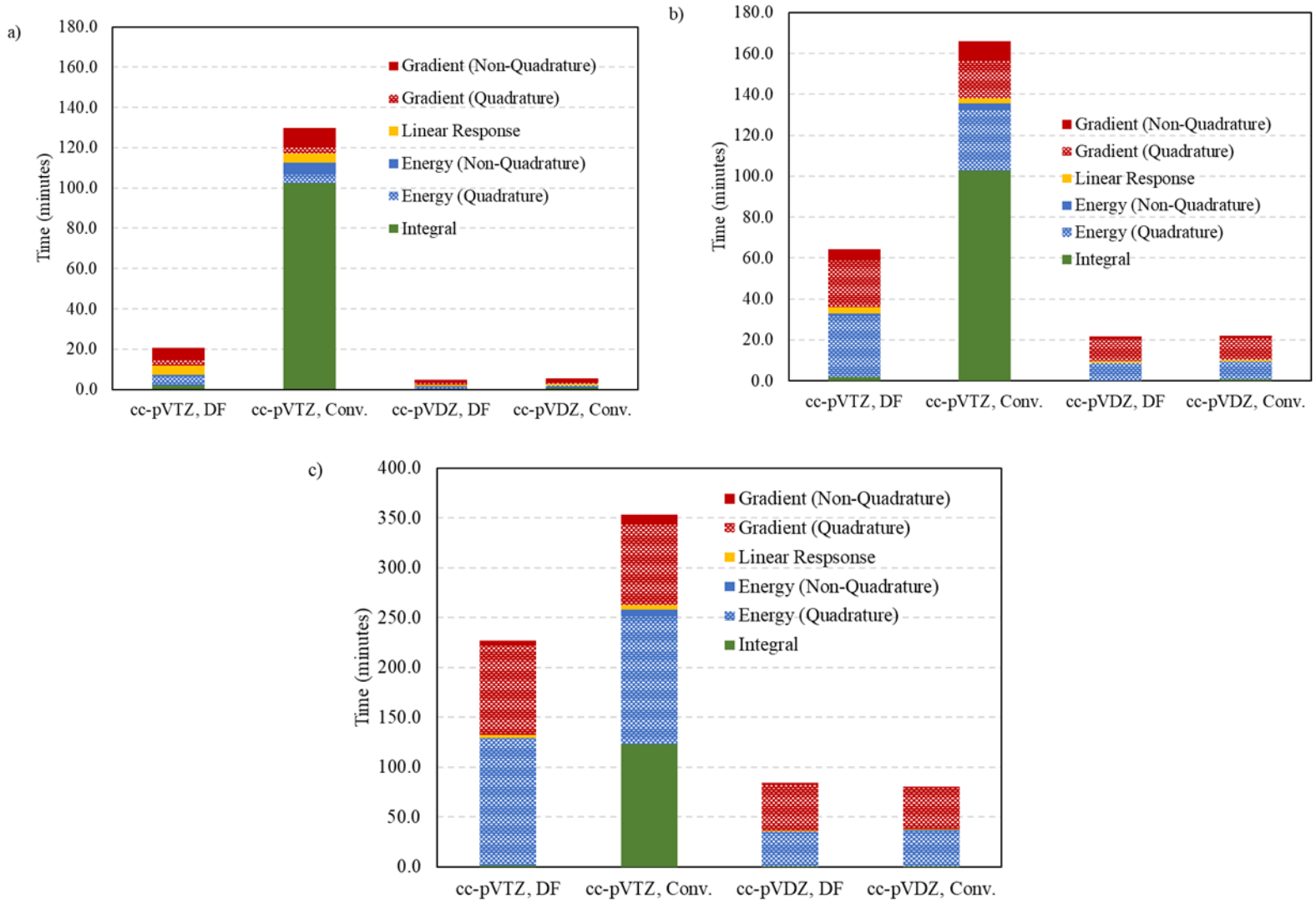

Figure 3.5: Comparison of the timings for one gradient and energy calculation of cytosine at the same geometry: (a) coarse grid; (b) fine grid; (c) ultrafine grid. Timings are reported for the integral, linear response, energy, and gradient modules. Time specifically spent in the numerical integration programs for the pair-density functional in the gradient and energy modules are denoted as quadrature, and the rest of the time is denoted as non-quadrature. Results are shown for the cc-pVTZ and cc-pVDZ basis sets. Calculations with density fitting are labeled DF, and those without density fitting are labeled Conv.

3.3.4 Conclusions

A study of gradient accuracy and geometric parameters obtained by density-fitted CAS-PDFT has been presented to validate the accuracy against both CAS-PDFT without density fitting and CASPT2 with density fitting. We also present computational timings to show the improved efficiency. The new density-fitted implementation of MC-PDFT gradients allows faster optimization of mid-size molecules compared to the conventional implementation, and it allows the optimization of large molecules such as rhodopsin, which would not be otherwise possible. The next steps will be (i) the development of a parallel version of density-fitted MC-PDFT in order to generate accurate potential energy surfaces for ground and excited states of extended systems and (ii) the development of analytic gradients for a multi-state treatment[95,96] of excited states.

Reproduced with permission from 24

CHAPTER 4

ANALYTIC GRADIENTS FOR COMPRESSED-STATE MULTISTATE PAIR-DENSITY FUNCTIONAL THEORY

4.1 Introduction

The MC-PDFT method by itself defines an expression for the total energy of a state but does not provide a procedure for state interaction. The Truhlar and Gagliardi groups have proposed a state-interaction model and several multistate extensions to MC-PDFT to address this issue.[21,95] Multistate PDFT methods are more efficient, and they evaluate state interaction by rotating the basis of a state-averaged complete-active-space self-consistent-field (SA-CASSCF) wave function within a model space into an intermediate-state representation, such that the molecular Hamiltonian furnishes nonzero coupling elements between intermediate states, while their energies (diagonal elements of the model-space effective Hamiltonian) are evaluated using MC-PDFT. The most promising method appears to be what we have named compressed multistate PDFT (CMS-PDFT).[96] The CMS-PDFT method defines the intermediate states as those linear combinations that maximize the sum of the classical Coulomb energies of the intermediate states, and this method was found to produce qualitatively correct and reasonably quantitatively accurate potential energy surfaces for a wide variety of systems exhibiting significant state interaction with a computational cost nearly equivalent to that of evaluating the same number of MC-PDFT total energies.[96]

The CMS-PDFT energy is not variational, and analytic gradients therefore require recasting CMS-PDFT energies in terms of a constrained energy minimization for which the Lagrange multipliers must be evaluated, similar to chapter 2. The specific contribution performed in this work by the author was the implementation of the energy and the first and second order response of the CMS objective function with respect to state rotations. This development is further discussed in the context of the total analytic gradient for CMS-PDFT.

In this chapter, there is a slight deviation from the previous notation which is necessary to

describe include the treatment of the intermediate states. The lowercase letters other than x, y, z index molecular orbitals (MOs), and capital letters other than X, Y, Z index many-electron states within a given complete active space (CAS). Specific types of many-electron states are identified with specific letter ranges: A, B for configuration state functions (CSFs), including the special case of single determinants; I, J for SA-CASSCF reference states, P, Q, R, S, T, U for CMS-PDFT intermediate states, and M, N for CMS-PDFT final states. For MOs, p, q, r, s, t indicate general MOs, i, j, k, l indicate active MOs, c indicates an inactive (core) MO (which is doubly occupied in all configurations) and a indicates a virtual MO (which is unoccupied in all configurations).

The uppercase letters X, Y, Z indicate three different types of unitary group generators that define the wave function in the CMS-PDFT method: X for orbital rotations and Y and Z for many-electron state rotations (i.e., unitary transformations of the configuration interaction [CI] vectors). Rotations between two states that are both within a particular model space are indicated by Z, and rotations between a state within the model space and another state outside of it are indicated by Y. The lowercase letters x, y, z indicate a set of Lagrange multipliers for the corresponding uppercase-letter generators or their associated variables. In what follows we proceed from the fundamentals of the CMS-PDFT energy to the details of constructing the corresponding nuclear gradients.

4.2 Theory

4.2.1 CMS-PDFT

CMS-PDFT energies and wave functions are the solutions to an eigenequation for an effective Hamiltonian defined in a model space of $n_{\mathrm{SA}} \geq 2$ multideterminantal wave functions:

$$|N\rangle \langle N| \hat{H}^{\mathrm{CMS}} |M\rangle = |N\rangle \delta_{MN} E_M^{\mathrm{CMS}}, \tag{4.1}$$

where

$$\hat{H}^{\mathrm{CMS}} = \sum_{P\neq Q}^{n_{\mathrm{SA}}} |P\rangle\, H_{PQ}\, \langle Q| + \sum_{P}^{n_{\mathrm{SA}}} |P\rangle\, E_P^{\mathrm{PDFT}}\, \langle P|\,, \tag{4.2}$$

where $H_{PQ} \equiv \langle P|\, \hat{H}\, |Q\rangle$ is a matrix element of the molecular electronic Hamiltonian and

$$\begin{aligned} E_P^{\mathrm{PDFT}} &= V_{\mathrm{NN}} + \sum_{p,q} h_{pq} D_{pq}^{PP} + \frac{1}{2} \sum_{p,q,r,s} g_{pqrs} D_{pq}^{PP} D_{rs}^{PP} \\ &\quad + E_{\mathrm{OT}}[\rho_P, \Pi_P], \end{aligned} \tag{4.3}$$

is the MC-PDFT energy expression: V_{NN} for the internuclear Coulomb repulsion; h and g respectively for the one- and two-electron Hamiltonian interaction elements; D^{PP}, ρ_P, and Π_P respectively for the one-body reduced density matrix (1-RDM), density, and on-top pair density for state P; and $E_{\mathrm{OT}}[\rho_P, \Pi_P]$ for the on-top energy functional that provides the energetic contributions due to electron correlation and exchange.

The states $|P\rangle$, $|Q\rangle$, etc. defining $\hat{H}^{\mathrm{CMS}}$ in Eq. (4.2) span a model space constructed by an underlying SA-CASSCF calculation,

$$|P\rangle = \sum_{I} |I\rangle\, \langle I|P\rangle\,, \tag{4.4}$$

where $|I\rangle$ are SA-CASSCF wave functions. The unitary transformation coefficients ($\langle I|P\rangle$) are determined by maximizing the sum of the classical electron-electron Coulomb energies under rotation of the states defining the model space,

$$\langle I|P\rangle = \mathrm{argmax}\; Q_{\text{a-a}}, \tag{4.5}$$

$$Q_{\text{a-a}} \equiv \frac{1}{2} \sum_{P} \sum_{i,j,k,l} g_{ijkl} D_{ij}^{PP} D_{kl}^{PP}. \tag{4.6}$$

The transformation from the SA-CASSCF basis ($|I\rangle\,, |J\rangle$) to the CMS-PDFT intermediate-state ba-

sis ($|P\rangle, |Q\rangle$) is necessary because PDFT does not furnish a way to approximate the Hamiltonian matrix elements coupling different states. Furthermore, in the SA-CASSCF basis, the off-diagonal Hamiltonian matrix elements appearing in Eq. (4.2) are identically zero by construction and therefore cannot be used to treat state interaction. The motivation for the specific form of the objective function defining the intermediate states, $Q_{\text{a-a}}$ in Eq. (4.6), is described in Ref. 96.

4.2.2 Derivatives of the CMS objective function

In anticipation of the requirements of Sec. 4.2.3 below, we here present the first and second derivatives of the CMS-PDFT objective function, $Q_{\text{a-a}}$, with respect to rotation between intermediate states. These derivatives can be utilized in a straightforward way to implement a Newton-Raphson gradient-descent algorithm for solving Eq. (4.5) above, although this was not the algorithm implemented originally in the previous work presenting the CMS-PDFT method.[96] This algorithm was implemented by the author in the PySCF package.

Parameterizing intermediate state $|P\rangle$ as

$$|P\rangle \quad \rightarrow \quad \exp\left[\hat{Z}\right]|P\rangle\,, \tag{4.7}$$

with

$$\hat{Z} \quad = \quad \sum_{P>Q} Z_{PQ}\left(|Q\rangle\langle P| - |P\rangle\langle Q|\right), \tag{4.8}$$

and defining

$$W^{PR}_{QS} \quad \equiv \quad \sum_{i,j,k,l} g_{ijkl} D^{PQ}_{ij} D^{RS}_{kl}\,, \tag{4.9}$$

$$V^{PR}_{QS} \quad \equiv \quad \delta_{QR}\left(W^{PS}_{SS} + W^{SP}_{PP} - W^{PQ}_{SQ} - W^{PR}_{SR} - 4W^{PR}_{QS}\right), \tag{4.10}$$

where D^{PQ} is the one-body transition density matrix between states P and Q, we have

$$Q_{\text{a-a}} = \frac{1}{2}\sum_{P} W_{PP}^{PP}, \tag{4.11}$$

$$\frac{\partial Q_{\text{a-a}}}{\partial Z_{PQ}} = 2\left(W_{PP}^{QP} - W_{QQ}^{PQ}\right), \tag{4.12}$$

$$\frac{\partial^2 Q_{\text{a-a}}}{\partial Z_{PQ}\partial Z_{RS}} = V_{QS}^{PR} - V_{PS}^{QR} - V_{QR}^{PS} + V_{PR}^{QS}\,. \tag{4.13}$$

The solution of Eq. (4.5) corresponds to a stationary point at which the Hessian is negative-definite,

$$\frac{\partial Q_{\text{a-a}}}{\partial Z_{PQ}} = 0, \tag{4.14}$$

$$\mathbf{H}_{ZZ}^{Q_{\text{a-a}}} \prec 0, \tag{4.15}$$

where $\mathbf{H}_{ZZ}^{Q_{\text{a-a}}}$ is the Hessian matrix with elements given by Eq. (4.13).

4.2.3 Analytic gradient formalism

It is straightforward to demonstrate that the final CMS-PDFT energies, E_M^{CMS}, are stationary with respect to their expansion coefficients in terms of the intermediate states, $\langle P|M\rangle$. Therefore, the derivatives of the expansion coefficients upon perturbation of the physical Hamiltonian do not contribute to the molecular gradients of the CMS-PDFT energies. As a consequence, differentiation of CMS-PDFT effective Hamiltonian matrix elements can be substituted for differentiation of CMS-PDFT final state total energies without loss of generality,

$$dE_M^{\text{CMS}} = \sum_{P,Q} \langle M|P\rangle\, dH_{PQ}^{\text{CMS}}\, \langle Q|M\rangle\,, \tag{4.16}$$

which is convenient because partial derivatives of H_{PQ}^{CMS} have simpler programmable expressions than those of E_M^{CMS} due to the form of Eq. (4.2). Therefore, in the following, we will consider

the gradient of H_{PQ}^{CMS} rather than that of E_M^{CMS} directly, with the understanding that the unitary transformation described by Eq. (4.16) is applied to any equation in which $\partial H_{PQ}^{\mathrm{CMS}}$ or dH_{PQ}^{CMS} appears.

The matrix elements of the effective Hamiltonian are not stationary with respect to their orbital coefficients and CI vectors. Therefore, the Hellmann-Feynman theorem does not apply, and we instead make use of Lagrange's method of undetermined multipliers to recast the expressions for H_{PQ}^{CMS} as the solutions to a constrained-optimization problem.We parameterize the intermediate-state wave functions as

$$|P\rangle \quad \rightarrow \quad \exp\left[\hat{X}\right]\exp\left[\hat{Y}\right]\exp\left[\hat{Z}\right]|P\rangle\,, \tag{4.17}$$

where $\hat{Z}$ is defined by Eq. (4.8) and

$$\hat{X} \;=\; \sum_{p>q}\sum_{\sigma} X_{pq}\left(\hat{c}_{p\sigma}^{\dagger}\hat{c}_{q\sigma} - \hat{c}_{q\sigma}^{\dagger}\hat{c}_{p\sigma}\right), \tag{4.18}$$

$$\hat{Y} \;=\; \sum_{P,A} Y_{PA}\left(\hat{Q}_{\mathrm{SA}}\,|A\rangle\,\langle P| - |P\rangle\,\langle A|\,\hat{Q}_{\mathrm{SA}}\right), \tag{4.19}$$

where $\hat{c}_{p\sigma}^{\dagger}$ ($\hat{c}_{p\sigma}$) creates (annihilates) an electron of spin σ in the pth orbital, where $|A\rangle$ is a single determinant or CSF, and where

$$\hat{Q}_{\mathrm{SA}} \;\equiv\; 1 - \sum_{P} |P\rangle\,\langle P|\,. \tag{4.20}$$

The variables X_{pq} and Y_{PA}, respectively, denote rotations between orbitals and rotations between many-electron states within the model space and those outside of it. The latter need to be explicitly separated from the rotations between two states within the model space [Z_{PQ} from Eq. (4.8)] using the projection operator $\hat{Q}_{\mathrm{SA}}$, because Y_{PA} and Z_{PQ} satisfy two unrelated sets of optimization conditions in the CMS-PDFT energy calculation. The effect of the projection operator is accounted for by requiring that every row of the matrix Y (and its corresponding Lagrange-multiplier matrix

y; see below) is orthogonal to all intermediate states (or equivalently to all reference or final states):

$$\sum_A Y_{PA} \langle A|Q\rangle = 0 \;\; \forall \;\; P, Q. \tag{4.21}$$

The minimization of the state-averaged energy of the underlying SA-CASSCF calculation (E_{CAS}) determines X and Y, whereas Eqs. (4.14) and (4.15) determines Z, so the Lagrangian for CMS-PDFT is written as

$$\begin{aligned} \mathcal{L}_{PQ}^{\mathrm{CMS}} &= H_{PQ}^{\mathrm{CMS}} + \sum_{p>q} \frac{\partial E_{\mathrm{CAS}}}{\partial X_{pq}} x_{pq} + \sum_{R,A} \frac{\partial E_{\mathrm{CAS}}}{\partial Y_{RA}} y_{RA} \\ &\quad + \sum_{R>S} \frac{\partial Q_{\text{a-a}}}{\partial Z_{RS}} z_{RS}, \end{aligned} \tag{4.22}$$

where, as a reminder, uppercase X, Y, Z indicate the wave function variables and lowercase x, y, z indicate the corresponding Lagrange multipliers. The values of the latter are determined by solving for

$$\frac{\partial \mathcal{L}_{PQ}^{\mathrm{CMS}}}{\partial X_{pq}} = \frac{\partial \mathcal{L}_{PQ}^{\mathrm{CMS}}}{\partial Y_{RA}} = \frac{\partial \mathcal{L}_{PQ}^{\mathrm{CMS}}}{\partial Z_{RS}} = 0, \tag{4.23}$$

so that the Lagrangian is stationary in X, Y, Z, x, y, and z. The dependence of these parameters on the molecular geometry can therefore be neglected when evaluating the molecular gradient,

$$\frac{\mathrm{d}H_{PQ}^{\mathrm{CMS}}}{\mathrm{d}\lambda} = \frac{\mathrm{d}\mathcal{L}_{PQ}^{\mathrm{CMS}}}{\mathrm{d}\lambda} = \frac{\partial \mathcal{L}_{PQ}^{\mathrm{CMS}}}{\partial \lambda}. \tag{4.24}$$

4.2.4 Determination of the Lagrange multipliers

Substituting Eq. (4.22) into (4.23) yields a system of coupled linear equations,

$$\begin{pmatrix} \nabla_X H_{PQ}^{\mathrm{CMS}} \\ \nabla_Y H_{PQ}^{\mathrm{CMS}} \\ \nabla_Z H_{PQ}^{\mathrm{CMS}} \end{pmatrix} + \begin{pmatrix} \mathbf{H}_{XX}^{E_{\mathrm{CAS}}} & \mathbf{H}_{XY}^{E_{\mathrm{CAS}}} & \mathbf{H}_{XZ}^{Q_{\text{a-a}}} \\ \mathbf{H}_{YX}^{E_{\mathrm{CAS}}} & \mathbf{H}_{YY}^{E_{\mathrm{CAS}}} & \mathbf{H}_{YZ}^{Q_{\text{a-a}}} \\ 0 & 0 & \mathbf{H}_{ZZ}^{Q_{\text{a-a}}} \end{pmatrix} \begin{pmatrix} \vec{x} \\ \vec{y} \\ \vec{z} \end{pmatrix} = \begin{pmatrix} 0 \\ 0 \\ 0 \end{pmatrix}, \tag{4.25}$$

where $\vec{x}, \ldots$, $\nabla_X, \ldots$, and $\mathbf{H}^f_{XX}, \ldots$ are vectors of Lagrange multipliers, vectors of first derivatives with respect to wave function variables, and Hessian matrix blocks of some function f with respect to wave function variables, respectively.

Some of the elements of the second-derivative matrix in Eq. (4.25) are zero by construction, because E_{CAS} is insensitive to rotations among intermediate states. The sole nonzero block in the Z rows, $\mathbf{H}^{Q_{\text{a-a}}}_{ZZ}$, was presented in Sec. 4.2.2, and we assume that the model space is small enough to store it in memory and invert it noniteratively,

$$\vec{z} = -\left(\mathbf{H}^{Q_{\text{a-a}}}_{ZZ}\right)^{-1} \cdot \nabla_Z H^{\mathrm{CMS}}_{PQ}. \tag{4.26}$$

We then solve for $\vec{x}$ and $\vec{y}$ with $\vec{z}$ fixed by rearranging Eq. (4.25):

$$\begin{pmatrix} \nabla_X H^{\mathrm{CMS}}_{PQ} + \mathbf{H}^{Q_{\text{a-a}}}_{XZ} \cdot \vec{z} \\ \nabla_Y H^{\mathrm{CMS}}_{PQ} + \mathbf{H}^{Q_{\text{a-a}}}_{YZ} \cdot \vec{z} \end{pmatrix} + \begin{pmatrix} \mathbf{H}^{E_{\mathrm{CAS}}}_{XX} & \mathbf{H}^{E_{\mathrm{CAS}}}_{XY} \\ \mathbf{H}^{E_{\mathrm{CAS}}}_{YX} & \mathbf{H}^{E_{\mathrm{CAS}}}_{YY} \end{pmatrix} \begin{pmatrix} \vec{x} \\ \vec{y} \end{pmatrix} = \begin{pmatrix} 0 \\ 0 \end{pmatrix}, \tag{4.27}$$

using the standard preconditioned conjugate gradient iterative solver.

Most of the gradient vectors and Hessian blocks appearing in Eqs. (4.25)–(4.27) are slight modifications or straightfoward generalizations of similar quantities that appear in the programmable equations for SA-CASSCF[97] or MC-PDFT based on SA-CASSCF wave functions[1]. For instance, the Hessian of the SA-CASSCF average energy, $\mathbf{H}^{E_{\mathrm{CAS}}}$, is well-established and is unchanged in the context of CMS-PDFT inasmuch as the Y sectors are expressed in the reference-state basis ($|I\rangle, |J\rangle$). (In practice, we evaluate the Hessian-vector product of $\mathbf{H}^{E_{\mathrm{CAS}}}_{YY}$ in the intermediate-state basis ($|P\rangle, |Q\rangle$); this modifies the form of the equation somewhat, as described in Sec. 1 of the supplementary material.)

The driving vector of Eq. (4.25) ($\nabla_X, \nabla_Y, \nabla_Z$) is either a minor generalization of the energy response for MC-PDFT with an SA-CASSCF wave function,[1] or an off-diagonal generalization

of the SA-CASSCF energy response,[97] depending on the indices P and Q:

$$\left\{\nabla_X H^{\mathrm{CMS}}_{PQ}\right\}_{pq} = \begin{cases} \frac{\partial E^{\mathrm{PDFT}}_P}{\partial X_{pq}} & P = Q \\ \frac{\partial H_{PQ}}{\partial X_{pq}} & \text{otherwise} \end{cases}, \tag{4.28}$$

$$\left\{\nabla_Y H^{\mathrm{CMS}}_{PQ}\right\}_{RA} = \begin{cases} \frac{\partial E^{\mathrm{PDFT}}_P}{\partial Y_{RA}} & P = Q \\ \frac{\partial H_{PQ}}{\partial Y_{RA}} & \text{otherwise} \end{cases}, \tag{4.29}$$

$$\left\{\nabla_Z H^{\mathrm{CMS}}_{PQ}\right\}_{RS} = \begin{cases} \frac{\partial E^{\mathrm{PDFT}}_P}{\partial Z_{RS}} & P = Q \\ \frac{\partial H_{PQ}}{\partial Z_{RS}} & \text{otherwise} \end{cases}. \tag{4.30}$$

In the diagonal case, we define

$$\hat{A} = \sum_{P,A} A_{PA} \left(|A\rangle \langle P| - |P\rangle \langle A|\right), \tag{4.31}$$

[i.e., $\hat{Y}$ from Eq. (4.19) without the projection operator, $\hat{Q}_{\mathrm{SA}}$], and evaluate

$$\frac{\partial E^{\mathrm{PDFT}}_P}{\partial X_{pq}}, \frac{\partial E^{\mathrm{PDFT}}_P}{\partial A_{PA}} \tag{4.32}$$

via Eqs. (28) and (29), respectively, of Ref. 1, using the intermediate-state CI vectors, densities, and density matrices of $|P\rangle$ rather than the SA-CASSCF reference-state quantities. The Y and Z

components of the latter are then separated,

$$\begin{aligned}
\frac{\partial E_P^{\mathrm{PDFT}}}{\partial Z_{RS}} &= \delta_{RP} \sum_A \frac{\partial E_P^{\mathrm{PDFT}}}{\partial A_{PA}} \langle A|S\rangle, \\
&\quad -\delta_{SP} \sum_A \frac{\partial E_P^{\mathrm{PDFT}}}{\partial A_{PA}} \langle A|R\rangle, \qquad (4.33) \\
\frac{\partial E_P^{\mathrm{PDFT}}}{\partial Y_{RA}} &= \delta_{RP} \left(\frac{\partial E_P^{\mathrm{PDFT}}}{\partial A_{PA}} - \sum_{S<P} \frac{\partial E_P^{\mathrm{PDFT}}}{\partial Z_{PS}} \langle A|S\rangle \right. \\
&\quad \left. + \sum_{S>P} \frac{\partial E_P^{\mathrm{PDFT}}}{\partial Z_{SP}} \langle A|S\rangle \right), \qquad (4.34)
\end{aligned}$$

It is important to remember that Z_{RS} is only defined for $R > S$.

In the off-diagonal case of Eqs. (4.28)–(4.30), we have

$$\begin{aligned}
\frac{\partial H_{PQ}}{\partial X_{pq}} &= F_{pq}^{PQ} - F_{qp}^{PQ} + F_{pq}^{QP} - F_{qp}^{QP}, \qquad (4.35) \\
\frac{\partial H_{PQ}}{\partial Y_{RA}} &= 0, \qquad (4.36) \\
\frac{\partial H_{PQ}}{\partial Z_{RS}} &= \delta_{QR} H_{PS} - \delta_{QS} H_{PR} \\
&\quad + \delta_{PR} H_{SQ} - \delta_{PS} H_{RQ} \qquad (4.37)
\end{aligned}$$

with

$$F_{pq}^{PQ} \equiv \sum_r h_{pr} D_{qr}^{PQ} + \sum_{r,s,t} g_{prst} d_{qrst}^{PQ}, \qquad (4.38)$$

where d^{PQ} is the two-body transition density matrix.

What remains are only the off-diagonal Hessian-vector products of the CMS-PDFT intermediate-state objective function, $\mathbf{H}^{Q_{\text{a-a}}}$, appearing in the first term on the left-hand side of Eq. (4.27). In order to express these terms concisely, we introduce additional Coulomb-potential intermediates

related to W_{QS}^{PR} defined in Eq. (4.9) above,

$$\hat{W}_Q^P = \sum_{i,j,k,l} g_{ijkl} D_{kl}^{PQ} \sum_\sigma \hat{c}_{i\sigma}^\dagger \hat{c}_{j\sigma}, \tag{4.39}$$

so that $W_{QS}^{PR} = \langle R| \hat{W}_Q^P |S\rangle = \langle P| \hat{W}_S^R |Q\rangle$. We also introduce effective density matrices and CMS generalized Fock matrices,

$$\tilde{D}_{ij}^{PP} \equiv \sum_Q \left(D_{ij}^{PQ} + D_{ij}^{QP} \right) \tilde{z}_{PQ}, \tag{4.40}$$

$$F_{pi}^{Q_{\text{a-a}}} \equiv \sum_{j,k,l} g_{pjkl} \sum_P \left(\tilde{D}_{ij}^{PP} D_{kl}^{PP} + D_{ij}^{PP} \tilde{D}_{kl}^{PP} \right), \tag{4.41}$$

$$F_{pc}^{Q_{\text{a-a}}} = F_{pa}^{Q_{\text{a-a}}} = 0, \tag{4.42}$$

where $\tilde{z}_{PQ}$ is

$$\tilde{z}_{PQ} = \begin{cases} z_{PQ} & P > Q \\ -z_{QP} & Q > P \end{cases}. \tag{4.43}$$

Using these intermediates, the Hessian-vector products in the first term on the left-hand side of Eq. (4.27) have the elements

$$\left\{ \mathbf{H}_{XZ}^{Q_{\text{a-a}}} \cdot \vec{z} \right\}_{pq} \equiv \sum_{P>Q} \frac{\partial^2 Q_{\text{a-a}}}{\partial X_{pq} \partial Z_{PQ}} z_{PQ}$$

$$= 2\left(F_{pq}^{Q_{\text{a-a}}} - F_{qp}^{Q_{\text{a-a}}} \right. \tag{4.44}$$

$$Big), \tag{4.45}$$

$$\left\{ \mathbf{H}_{YZ}^{Q_{\text{a-a}}} \cdot \vec{z} \right\}_{PA} \equiv \sum_{Q>R} \frac{\partial^2 Q_{\text{a-a}}}{\partial Y_{PA} \partial Z_{QR}} z_{QR} = \langle A| \hat{Q}_{\text{SA}} \sum_Q \tilde{z}_{PQ}$$

$$\times \left(4\hat{W}_Q^P |P\rangle + 2\left(\hat{W}_P^P - \hat{W}_Q^Q \right) |Q\rangle \right). \tag{4.46}$$

4.2.5 *Nuclear-coordinate derivatives of the Lagrangian*

Having determined the Lagrange multipliers by solving Eq. (4.23), it remains to evaluate the molecular gradient by differentiating the Lagrangian itself [Eq. (4.24)]:

$$\begin{aligned}\frac{\partial \mathcal{L}_{PQ}^{\mathrm{CMS}}}{\partial \lambda} &= \frac{\partial H_{PQ}^{\mathrm{CMS}}}{\partial \lambda} + \sum_{p>q} \frac{\partial^2 E_{\mathrm{CAS}}}{\partial \lambda \partial X_{pq}} x_{pq} \\ &\quad + \sum_{R,A} \frac{\partial^2 E_{\mathrm{CAS}}}{\partial \lambda \partial Y_{RA}} y_{RA} + \sum_{R>S} \frac{\partial^2 Q_{\text{a-a}}}{\partial \lambda \partial Z_{RS}} z_{RS} \,. \end{aligned} \tag{4.47}$$

The first-term on the right-hand side of Eq. (4.47) is the Hellmann-Feynman term and, just like the driving vector above, it differs depending on whether one is considering a diagonal or off-diagonal element:

$$\frac{\partial H_{PQ}^{\mathrm{CMS}}}{\partial \lambda} = \begin{cases} \frac{\partial E_P^{\mathrm{PDFT}}}{\partial \lambda} & P = Q \\ \frac{\partial H_{PQ}}{\partial \lambda} & \text{otherwise} \end{cases} . \tag{4.48}$$

In the diagonal case, the Hellmann-Feynman contribution is essentially the same as in MC-PDFT based on an SA-CASSCF wave function,[1] except that intermediate state $|P\rangle$ is used instead of a SA-CASSCF reference state:

$$\begin{aligned}\frac{\partial E_P^{\mathrm{PDFT}}}{\partial \lambda} &= \frac{\partial V_{\mathrm{NN}}}{\partial \lambda} + \sum_{p,q} \frac{\partial h_{pq}}{\partial \lambda} D_{pq}^{PP} + \frac{1}{2} \sum_{p,q,r,s} \frac{\partial g_{pqrs}}{\partial \lambda} D_{pq}^{PP} D_{rs}^{PP} \\ &\quad + \frac{\partial E_{\mathrm{OT}}[\rho_P, \Pi_P]}{\partial \lambda} - \sum_{p,q} \frac{\partial s_{pq}}{\partial \lambda} F_{pq}^{(\mathrm{OT})}, \end{aligned} \tag{4.49}$$

where s_{pq} is the overlap matrix between MOs p and q, the derivatives are partial because the MO coefficients are treated as fixed, and $\partial E_{\mathrm{OT}}[\rho_P, \Pi_P]/\partial \lambda$ and $F_{pq}^{(\mathrm{OT})}$ are given by Eqs. (49) and (31) of Ref. 1, respectively. In the off-diagonal case, the Hellmann-Feynman contribution is like that of SA-CASSCF,[97] except that transition density matrices coupling $|P\rangle$ and $|Q\rangle$ are used instead of the reduced density matrices of SA-CASSCF reference states and the internuclear potential term

is omitted:

$$\frac{\partial H_{PQ}}{\partial \lambda} = \sum_{p,q} \frac{\partial h_{pq}}{\partial \lambda} D^{PQ}_{pq} + \frac{1}{2} \sum_{p,q,r,s} \frac{\partial g_{pqrs}}{\partial \lambda} d^{PQ}_{pqrs} - \frac{1}{2} \sum_{p,q} \frac{\partial s_{pq}}{\partial \lambda} \left(F^{PQ}_{pq} + F^{QP}_{pq} \right). \tag{4.50}$$

The second and third terms on the right-hand side of Eq. (4.47) are also equivalent to corresponding terms in both SA-CASSCF[97] and MC-PDFT based on SA-CASSCF[1], except that CMS-PDFT intermediate-state quantities are used instead of SA-CASSCF reference-state quantities. The fourth term is unique to CMS-PDFT:

$$\sum_{P>Q} \frac{\partial^2 Q_{\text{a-a}}}{\partial \lambda \partial Z_{PQ}} z_{PQ} = \sum_{p,q,r,s} \frac{\partial g_{pqrs}}{\partial \lambda} \sum_{P} \left(D^{PP}_{pq} \tilde{D}^{PP}_{rs} \right) - \sum_{p,q} \frac{\partial s_{pq}}{\partial \lambda} F^{Q_{\text{a-a}}}_{pq}. \tag{4.51}$$

4.3 Conclusion

In this chapter, we report the implementation of the CMS-PDFT energy and a portion of the gradient in *PySCF*. This was disccussed in the context of the total CMS-PDFT analytic gradient. CMS-PDFT is a promising method for studying excited states with strong state interaction. In the following two chapters, we highlight the necessity of these multi-reference treatments with two examples. We first focus on dual photo-redox catalysis and then close with intrastrand photolesion foramtion in DNA.

Reproduced partially with permission from 25.

CHAPTER 5

THE EXCITED STATES OF LNI$^{II/III}$(ARYL)(HALIDE) COMPLEXES RELEVANT TO NI–HALIDE BOND HOMOLYSIS IN THE ARYLATION OF C(SP3)–H BONDS

5.1 Introduction

Photoredox catalysis has gained significant attention in organic synthesis for its capacity to promote difficult reactivity using visible light and earth-abundant metals.[98–102] In the landscape of possible applications, combined photoredox-nickel catalysis has the potential to solve one of the long-standing challenges in organometallic chemistry, which is C_{sp3}-C_{sp2}/C_{sp3} cross-coupling reactions.[103] In contrast to traditional cross-coupling chemistry, light mediated photoredox-nickel catalysis is an effective strategy for activating rarely utilized nucleophiles at mild conditions, expanding the list of cross-coupling partners.[98,104] In this protocol nucleophiles are used as radical precursors to generate C_{sp3}-radicals within the C_{sp3}-C_{sp2}/C_{sp3} cross-coupling scheme. The most notable studies utilized carboxylic acids,[105–108] alkyltrifluoroborates,[102,104,109,110] 4-alkyl-1,4-dihydropyridines,[111,112] potassium alkylbis-(catecholato) silicates[104,113] alkyl halides[114] and similars as radical precursors.

Another remarkable advantage of this methodology is the functionalization of C_{sp3}-H bonds as a cross-coupling partner.[115–118] The first example being the direct α-amino C_{sp3}-H arylation with photoredox-nickel catalysis reported by MacMillan and coworkers,[105] followed by the development of a photoredox-nickel-HAT (HAT = Hydrogen Atom Transfer) catalytic strategy for arylation[119] and alkylation[120] of α-amino C_{sp3}-H bonds. Connected strategies were developed by Glorius and Houk,[121] as well as by Rueping,[122] for the arylation of allylic C_{sp3}–H bonds, and by Martin and Rueping for the cross-coupling of α-oxy C_{sp3}-H[123] and benzylic C_{sp3}-H[124] bonds, respectively. Other variations on the theme developed by Doyle;[125–127] involve using bis(oxazoline), instead of commonly used bipyridine (bpy), as Ni-ligand for the arylation of

α-amino C_{sp3}–H bonds with aryl iodides,30 or using aryl chlorides as coupling partners for the arylation of α-oxy C_{sp3}-H bonds.[126,127] A similar reaction was also reported by Molander, who used aryl bromide as electrophilic partner.[128] The C_{sp3}-C_{sp3} cross-coupling of α-oxy C_{sp3}-H bond with alkyl halide was reported by König.[129]

At odds with these remarkable and broad applications of photoredox-nickel dual catalysis, the amount of computational studies aimed at providing detailed mechanistic understanding is scarce.[111,130] Regarding the sequence of oxidation states of nickel within the catalytic cycle, we recently demonstrated that the methodology involving a HAT catalyst follows the sequence NiI-NiII-NiI-NiIII, with the associated radical addition-SET-oxidative addition-reductive elimination (SET = Single Electron Transfer) fundamental steps.[131,132] The active catalyst is a LNiI–Br species and the rate-determining transition state corresponds to oxidative addition of Ar/Alk–Br to the NiI-complex.[121] The photocatalyst is predicted to activate the nickel complex by SET.

Along another direction, Doyle provided photo-chemical characterization of the electronic states following light excitation of the LNi^{II}(halide) species, with a focus on the mechanism of the Ni^{II}-aryl homolytic dissociation.[133] The main conclusion was that upon excitation of the S_0 LNi^{II}(halide)complex to a metal to ligand charge transfer (^{1}MLCT) state, intersystem crossing leads to a triplet ^{3}MLCT state, followed by the decay of the complex into a triplet ligand field ^{3}(d-d) excited state. Based on density functional theory (DFT) calculations, thermal activation from the latter was proposed to be responsible for Ni-aryl homolytic dissociation. This hypothesis was revised by Hadt on the basis of photo-chemical experiments and multireference calculations.[134,135] The main conclusion was that the excited ^{1}MLCT state can undergo intersystem crossing with the two-electron triplet Ni-aryl repulsive surfaces corresponding to the ^{3}MLCT state and to a ligand to metal charge transfer (LMCT) state. NiII-aryl homolytic dissociation spontaneously occurs after intersystem crossing.

Despite all these remarkable advances, our understanding of the Ni-halide bond dissociation step is incomplete. Different mechanisms, involving either a SET or an energy transfer (EnT) step,

specifically the photosensitized transfer of an exciton, have been proposed in literature,[118,127,128] and we believe a conclusive answer on their feasibility has not been provided yet. This is surprising, considering that Ni-halide bond dissociation occurs at each loop of the catalytic cycle. Understanding it could allow the modification of the nickel ligands and/or the reaction conditions to achieve higher turnover rates and efficiencies. Moreover, using this approach the experimental partners currently coupled with aryl-halides are limited to α-oxy or α-amino C_{sp3}-H bonds, and there is widespread interest to expand the scope. For these reasons we decided to explore this reaction using electronic structure methods. In this work we focus on the arylation of C_{sp3}-H bonds by Ir^{III}-Ni^{0} dual catalysis developed by Molander,[128] Doyle3[126,127] and Rueping[122] independently (figure 5.1).

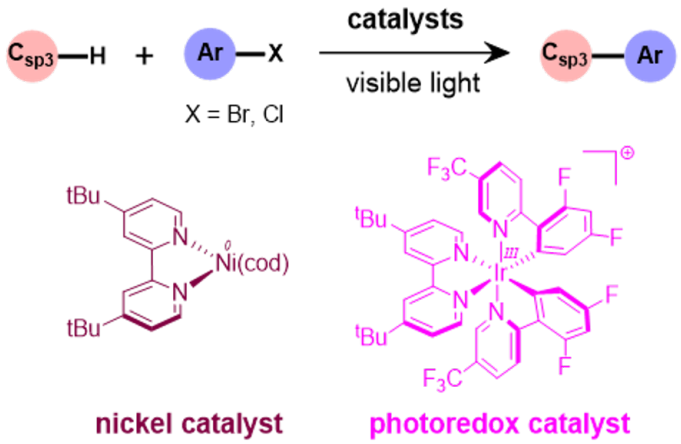

Figure 5.1: Ir^{III}-Ni^{0} catalyzed arylation of C_{sp3}–H bond (C_{sp3}–C_{sp2} coupling).27, 31-33

With this aim we performed DFT calculations to define all possible mechanistic pathways considering PhBr as the electrophilic coupling partner. In general, the excited states of transition metal containing species that lead to photoredox bond homolysis require a multireference (MR) treatment.[136] We thus employed a recently developed MR method, multiconfiguration pair-density functional theory (MC-PDFT)[17,18] that is accurate and orders of magnitude more cost effective

than performing perturbation theory on a multiconfigurational self-consistent-field (MCSCF) reference wave function. We performed MC-PDFT calculations on LNiII(Ar)Br and its oxidized form, [LNiIII(Ar)Br]+, exploring the Ni-Br bond homolysis and comparing the viability of SET and EnT mechanisms. Further, to show whether the EnT mechanism is generalizable to other Ni-halide systems, we extended the multireference calculations to the chloride analogs, LNiII(Ar)Cl and [LNiIII(Ar)Cl]+. The objectives of this work are: i) characterize the excited states of Ni-complexes; ii) explain the energy transfer step; and iii) define the favored pathway of Ir-Ni dual catalyzed C_{sp3}-H arylation.

5.2 Computational Methods

5.2.1 DFT Calculations

The Gaussian 16 software[137] was used for geometry optimizations of all stationary states and transition states by employing the exchange and correlation functional of Perdew, Burke and Ernzerhof, (PBE) called PBE0 which includes Hartree-Fock(HF) exchange in a 3:1 ratio of PBE to HF, in addition with including the Grimme empirical dispersion correction D3 (PBE0-D3).[138,139] To simulate the effect of the THF solvent, the universal solvation model that is based on the full solute electron density (SMD) implicit solvation model was used.[140] For basis sets, we employed the split-valence plus single polarization def2-SVP[141] for lighter atoms (H, C, N, O, and Cl), triple-ζ def2-TZVP[141] for Ir, Ni and Br. This basis set combination is referred as BS1. For further validation of energies, single point calculations using the SMD solvation model were performed with the hybrid-meta-GGA M06 functional[142] with the SDD ECP for Ir and def2-TZVPP[141] for rest of the atoms. This basis set combination is referred as BS2. Unless specified otherwise, free energy values, ΔG, combining single point energy (ΔE) at M06(SMD-THF)/BS2 with the thermal correction (ΔG-corr) at PBE0-D3(SMD-THF)/BS1, represented by M06(SMD-THF)/BS2//PBE0-D3(SMD-THF)/BS1, are reported throughout the manuscript and supporting in-

formation. Marcus-Hush theory was used to estimate activation barriers of single electron transfer (SET) steps, $\Delta G^{\ddagger}_{MH}$.[143]

5.2.2 Multireference Calculations

To reduce the computational cost, we used the bpy ligand instead of di-tertbutyl-bipyridine one used experimentally and we re-optimized the structures with the ORCA[144] software. The optimized geometries obtained with ORCA and Gaussian for the same species are identical. For (bpy)Ni^{II}(Ph)X (X=Br, Cl), besides the ground state singlet, equilibrium structures were obtained for the first 5 triplet states and for the oxidized, [(bpy)Ni^{III}(Ph)X]$^+$ species, equilibrium structures were obtained for the first doublet, using, in both cases, time-dependent density functional theory (TD-DFT).[145–147] For all the Kohn-Sham DFT and TD-DFT described above the PBE0-D3 functional was employed, together with the SMD implicit solvent model for the THF solvent, and the same basis sets as BS1 or def2-SVP[141] for lighter atoms (H, C, and N), def2-TZVP[141] for Ni and Br or Cl (identical to the DFT treatment above apart from the smaller bpy ligand). We used the Tamm-Dancoff approximation, (TDA)[148] which is the default in ORCA and improves the stability of triplet states with TD-DFT.[149] No symmetry was used in any of the geometry optimizations and the defgrid3 was used for all ORCA calculations.

Multireference calculations were subsequently performed using MC-PDFT.[17] The total MC-PDFT electronic energy is the sum of the kinetic energy, nuclear attraction, and classical approximation to the electron-electron Coulomb energy from the MCSCF reference, and the exchange and correlation energies obtained from a MC-PDFT on-top functional. The on-top functionals are translations of existing Kohn-Sham density functionals (DF) and use translated α- and β-spin densities obtained from the total electron density and the on-top pair density of the MCSCF wave function. Hybrid multi-configurational pair density functional theory (HMC-PDFT)[150] computes the total energy as a weighted average of the total MCSCF energy and the on-top MC-PDFT energy (i.e., λ $E_{MC\text{-}SCF}$ + (1 − λ) $E_{MC\text{-}PDFT}$ where λ is the weighting of the MC-SCF reference

energy). In this work, we use the tPBE0 HMC-PDFT functional uses translated PBE (tPBE) on-top functional with λ set equal to 0.25. It has been shown to give accurate excitation energies for a broad class of systems.[150] We thus employed HMC-PDFT to perform a series of single-point calculations as described in the following.

1. At the singlet ground-state geometry, three separate HMC-PDFT calculations were performed, that respectively included 15 (bpy)Ni^{II}(Ph)X singlets, 15 (bpy)Ni^{II}(Ph)X triplets, and 15 [(bpy)Ni^{III}(Ph)X]$^+$ doublets.

2. At each of the excited state optimized structures (5 (bpy)Ni^{II}(Ph)X triplet structures and 1 [(bpy)NiIII(Ph)X]+ doublet structure), a state-averaged HMC-PDFT calculation was performed with 15 states of their specified spin symmetry (triplets for (bpy)Ni^{II}(Ph)X and a doublet for [(bpy)NiIII(Ph)X]+).

All HMC-PDFT calculations were performed in Openmolcas.[48] The def2-TZVP basis set[141] was used for all atoms. The most balanced and cost-effective active space for all excited states contains twelve electrons in twelve orbitals, CAS(12e,12o), (Figure 6.9). This includes a σ bonding orbital between Ni and the phenyl and X ligands, the 3d orbitals of Ni, a π* orbital on the bpy ligand, and four of a correlating set of 3d' orbitals of Ni, to account for the second shell effect.[151] For the singlet and triplet (bpy)Ni^{II}(Ph)X state-averaged CASSCF calculations this active space was employed. In the [(bpy)Ni^{III}(Ph)X]$^+$ doublet calculations the corresponding CAS(11e, 12o) active space, upon orbital optimization, presented a variation of a virtual orbital, namely sometimes this orbital showed more second d-shell character and sometimes more bpy π* orbital character.

5.3 Results and Discussion

We selected Ir[dF(CF_3)ppy]$_2$(dtbbpy)$^+$ as photoredox catalyst, Ni^0(cod)$_2$ as nickel-catalyst, THF and PhBr as substrates, and K_2HPO_4 as the base (figure 5.1). Results and discussion are divided into three sections: i) possible nickel catalytic mechanisms, ii) characteristics of the excited states

of the nickel complexes relevant to the C_{sp3}-H activation, and iii) relative feasibility between energy transfer (EnT) and single electron transfer (SET) mechanisms.

5.3.1 Mechanistic Consideration: Ni-catalytic Cycle

The reaction starts with the generation of an active nickel catalyst 1-Ni0 by ligand exchange and PhBr co-ordination, a step endergonic by 3.1 kcal/mol from the starting Ni(cod)2 complex (Figure 1a). The first step of the nickel catalytic cycle is the oxidative addition of aryl-Br, leading to 2-NiII via transition state [1-2]‡, with an activation barrier of 8.9 kcal/mol (Figure 1b). This is the common starting step in photoredox-nickel dual catalysis in the presence of a Ni(0)-catalyst. The versatility of the nickel catalytic mechanism starts from intermediate 2-NiII.

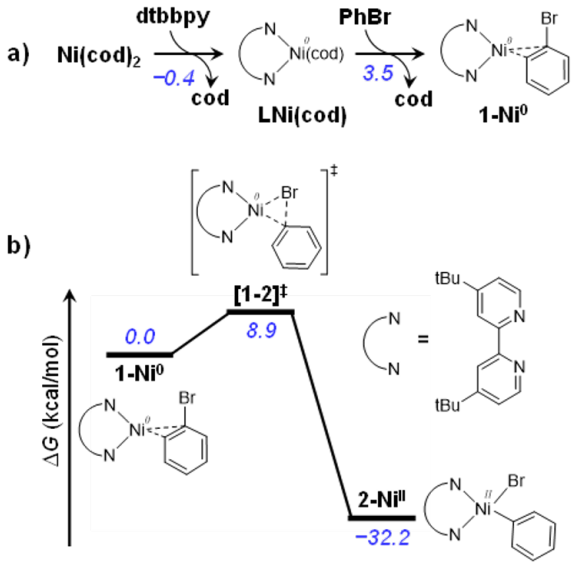

Figure 5.2: Free energy profile of oxidative addition of PhBr to Ni0-complex. The energy values are at M06(SMD-THF)/BS2//PBE0-D3(SMD-THF)/BS1 level of theory.

Depending on the role of the photoredox catalyst two alternative nickel catalytic cycles have previously been proposed, where the key steps are EnT[128] and SET,[127] respectively. For the

sake of completeness we have considered three possible reaction pathways, M1, M2 and M3 (Scheme 2). Along M1 the reaction proceeds via EnT from ^{T}**Ir^{III}** to **2-Ni^{II}**. In contrast, pathways **M2** and **M3** involve SET as the key step. Pathway **M2** occurs via reductive quenching of ^{T}**Ir^{III}** by **2-Ni^{II}**, while oxidative quenching of TIrIII is operative along **M3**. Pathways **M1** and **M2** are discussed in detail (Figure 2 and 3), whereas we only discuss briefly pathway **M3** since it is energetically unfavored. The **M3** energy profile is reported in the SI (Figure S1).

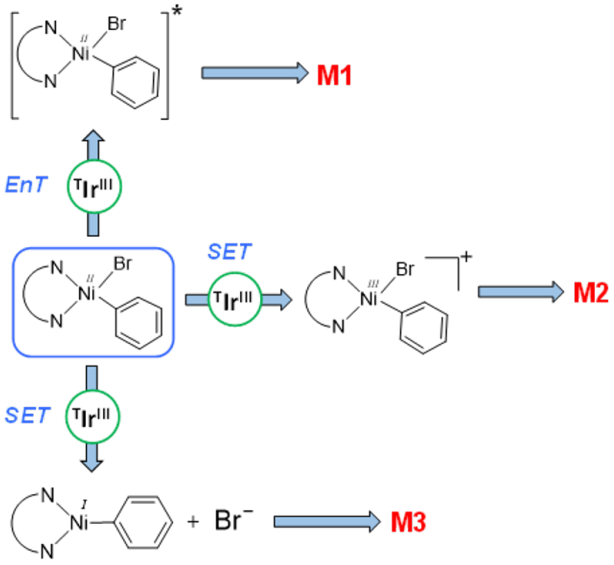

Figure 5.3: Mechanistic considerations for nickel-catalytic cycles in photoredox-nickel catalyzed arylation of α-oxy C_{sp3}–H bonds.

Along the M1 pathway EnT is involved from ^{T}**Ir^{III}** to **2-Ni^{II}**, as proposed by Molander and coworkers (Figure 2).[128] The EnT step results in the excited state **[2-Ni^{II}]***, which serves as source of Br• radical activating the C_{sp3}–H bond. The details of the EnT step and the electronic structure of **[2-Ni^{II}]*** are discussed in section 3.2. The next step is C_{sp3}–H activation, which can occur via outer-sphere (blue line) or inner-sphere (red line) mechanisms.[123,128] Along the outer-sphere pathway the C_{sp3}–H α-bond of THF is activated via the THF·Br• intermediate. No energy

barrier was found for this dissociation step in the one dimensional PESs both in the gas phase and with implicit solvation model calculations. The activation of the α-alkoxy C_{sp3}–H bond of THF by the Br• radical generates the THF• radical while liberating HBr, the latter readily trapped by K2HPO4. The resulting THF• binds to doublet **3-Ni^{I}** to give the **4-Ni^{II}** intermediate. Consistently with our previous studies[131,132] this is a highly exergonic and barrierless step. The inner-sphere C_{sp3}–H activation pathway takes place via the concerted transition state **^{T}[3-4]‡** and an activation barrier of 12.0 kcal/mol (red line, Figure 2). The energy profile clearly indicates that the outer sphere pathway is favored over the inner sphere one. Finally, the last step, reductive elimination from **4-Ni^{II}**, liberates the C_{sp3}–C_{sp3} coupling product with regeneration of nickel the catalyst via transition state **[4-5]‡** and an energy barrier of 16.1 kcal/mol.

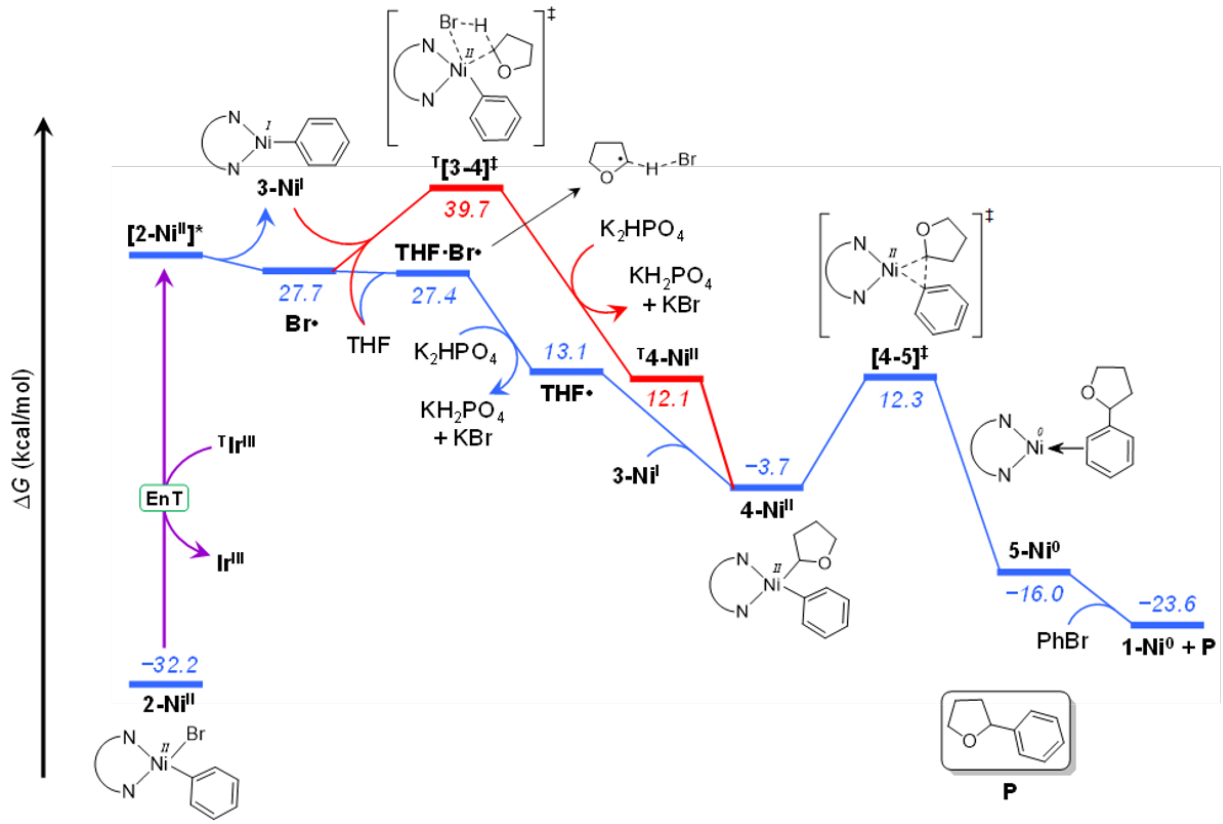

Figure 5.4: Free energy profile of pathway **M1**. For energy conventions refer Figure 5.2

Pathway **M2** has been proposed by Doyle, and it involves SET as a fundamental step via reductive quenching of ^{T}**Ir^{III}** by **2-Ni^{II}** (Figure 3).[127] The single electron oxidation of **2-Ni^{II}** to ^{D}**6-Ni^{III}**, SET1, is an exergonic step with an estimated barrier of 0.2 kcal/mol. Upon direct photoexcitation, homolysis of Br• from ^{D}**6-Ni^{III}** leads to the **7-Ni^{II}** complex. As in pathway **M1** Br• activates the C_{sp3}–H bond of THF, generating THF•. Simultaneously, **7-Ni^{II}** gets reduced by **Ir^{II}** to generate **3-Ni^{I}**, SET2, a step exergonic by 25.5 kcal/mol with an estimated energy barrier of 6.8 kcal/mol. Barrierless exergonic recombination of the two doublet species **3-Ni^{I}** and THF• leads to the **4-Ni^{II}**, which is ready for the reductive elimination to liberate the product. In the outer sphere pathway C_{sp3}–H bond activation occurs via transition state ^{D}**[7-8]‡** for an energy barrier of 6.8 kcal/mol, resulting in the **D8-Ni^{III}** complex. Single electron reduction of the resulting complex by **Ir^{II}**, SET3, generates **4-Ni^{II}**, from which the product is liberated by reductive elimination from **4-Ni^{II}**, as discussed in pathway **M1**.

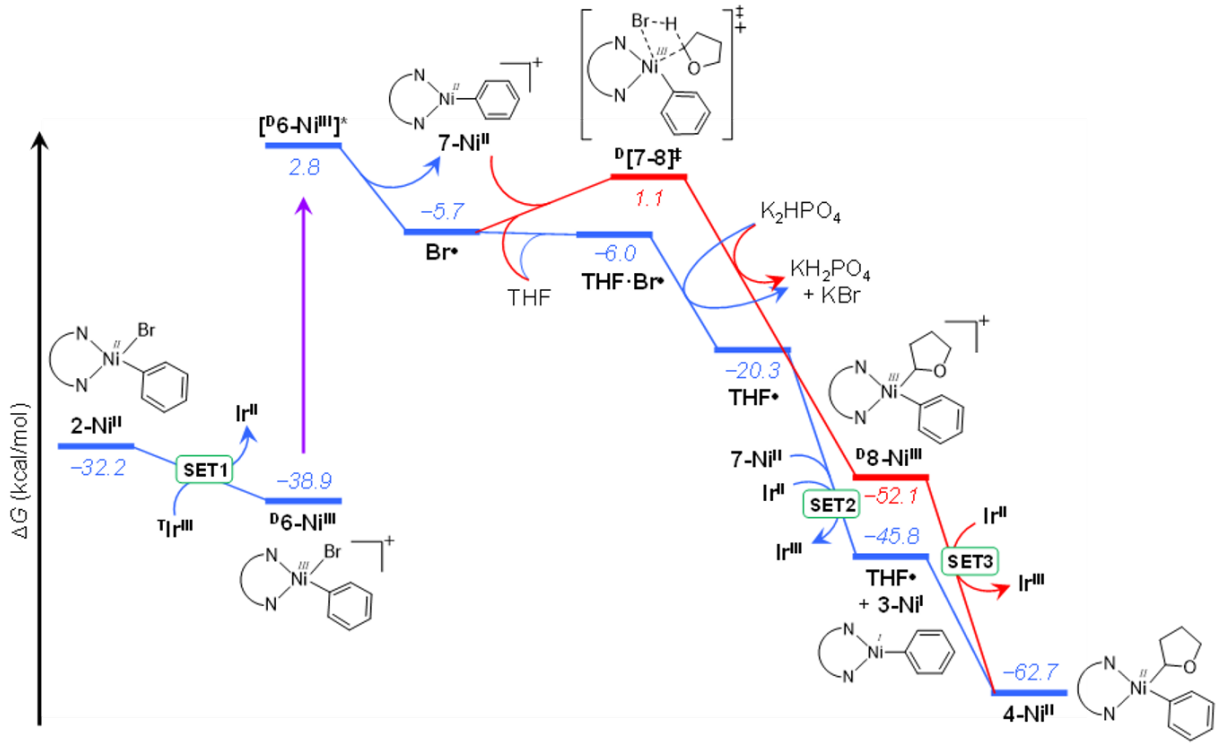

Figure 5.5: Free energy profile of pathway **M2**. For energy conventions refer Figure 5.2

An alternative pathway involving a SET step, **M3**, could involve the oxidative quenching of $^{\mathbf{T}}\mathbf{Ir}^{\mathbf{III}}$ by **2-Ni$^{\mathbf{II}}$** intermediate. The reduction of **2-Ni$^{\mathbf{II}}$** generating **3-Ni$^{\mathbf{I}}$** and Br–, SET4, is endergonic by 28.9 kcal/mol and the estimated barrier is 38.5 kcal/mol. The following oxidation of Br– by $\mathbf{Ir}^{\mathbf{IV}}$ can generate Br• that would promote activation of the C_{sp3}–H bond THF. However, this pathway can be excluded and is not discussed further because step SET4 is too high in energy to occurr at room temperature.[127,128]

5.3.2 Excited States of (bpy)Ni^{II}(Ph)X and [(bpy)Ni^{III}(Ph)X]$^{+}$

The above free energy profiles indicate that both EnT (**M1**) and SET (**M2**) pathways are predicted to be operable (Figures 2 and 3), while the **M3** is excluded due to the high energy of SET4. Control experiments performed by Molander[128] and Doyle[127] independently do not clarify which is the operative pathway, as they were proposed to support an EnT and a SET pathway, respectively. To resolve this inconsistency we investigated the excited states of the [(bpy)Ni^{III}(Ph)X, **2-Ni$^{\mathbf{II}}$**, and [(bpy)NiIII(Ph)X]+, **6-$^{\mathbf{D}}$Ni$^{\mathbf{III}}$**, complexes using HMC-PDFT (tPBE0) calculations and in this section, we focus on the results where X=Br. The states that were likely to result in Ni-Br homolysis, based on their dominant configuration state functions (CSFs), were observed in the optimized five (bpy)Ni^{II}(Ph)Br geometries of the triplet (*vide supra*). For all calculations involving the [(bpy)Ni^{III}(Ph)Br]$^{+}$ doublet geometries, the energies of dissociative states were over 100 kcal/mol and would be inaccessible by visible light excitation. This suggests that an electron transfer that resulted in the charged species would need a higher energy light source than the range used in experiments (400-668 nm light source corresponding to 40-70 kcal/mol).[128] At the (bpy)Ni^{II}(Ph)Br optimized geometry of the lowest energy triplet (triplet state 1), out of the 15 states considered, only the 5th to 11th states are in an energy range of 40-70 kcal/mol above the ground state, and we will focus our discussion on them. (figure 4).

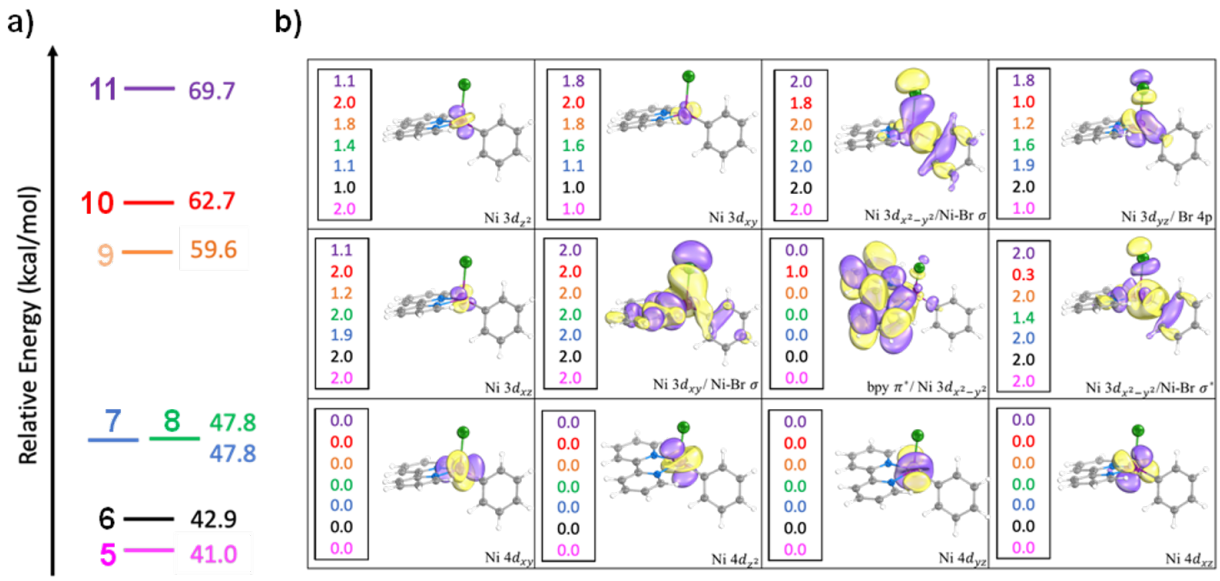

Figure 5.6: a) Energies relative to the ground state singlet of all triplet excited states. b) Active space orbitals and occupation numbers (inset) of excited states within a 40-70 kcal/mol range from ground state for (bpy)NiII(Ph)Br. Excited state colorings are same as in part a). The Ni-Br and Ni-Ph bonds are in the xy-plane, nearly aligned to the x and y-axis, respectively. Excited state colors in the figure: 5-pink, 6-black, 7-blue, 8-green, 9-orange, 10-red, and 11-purple.

Many of these states are multi-configurational in nature, with the natural orbital occupation numbers deviating from integer values. This validates the use of multi-configurational methods for these system. All excited states 5-7, 9 and 11 could possibly result in the Ni-Br bond breaking. To broaden the scope of this work we extended the multiconfigurational study to the chloro analogues (bpy)Ni^{II}(Ph)Cl and [(bpy)Ni^{III}(Ph)Cl]$^+$. The excited states that would be responsible for Ni-Cl homolysis were found at the optimized (bpy)Ni^{II}(Ph)Cl geometry of triplet state 3. There were 15 states included HMC-PDFT calculation and four of them were relevant for the Ni-Cl homolysis and within the energy range accessible by interaction with $^{\mathbf{T}}\mathbf{Ir}^{\mathbf{III}}$, and were thus further analyzed. State 9 in fig. 5.7, strongly resembles excited states 5 and 9 at the lowest energy triplet geometry of

the Br analogue and thus can be involved in Ni-Cl homolysis via Dexter EnT transfer with $^{\mathbf{T}}\mathbf{Ir}^{\mathbf{III}}$. As for the SET pathway, excitation energies for $[(bpy)Ni^{III}(Ph)Cl]^{+}$ are over 100 kcal/mol and thus are not expected to be responsible for Ni-Cl homolysis. Overall, this analysis indicates that the chloro analogues follow the same trend defined for the $(bpy)Ni^{II}(Ph)Br$ and $[(bpy)Ni^{II}(Ph)Br]^{+}$ complexes. The excited states in the chloro-analogues had the same character but with slight energetic differences, only 3 states fell within the 40-70 kcal/mol range and each state showed Ni-Cl bond breaking character.

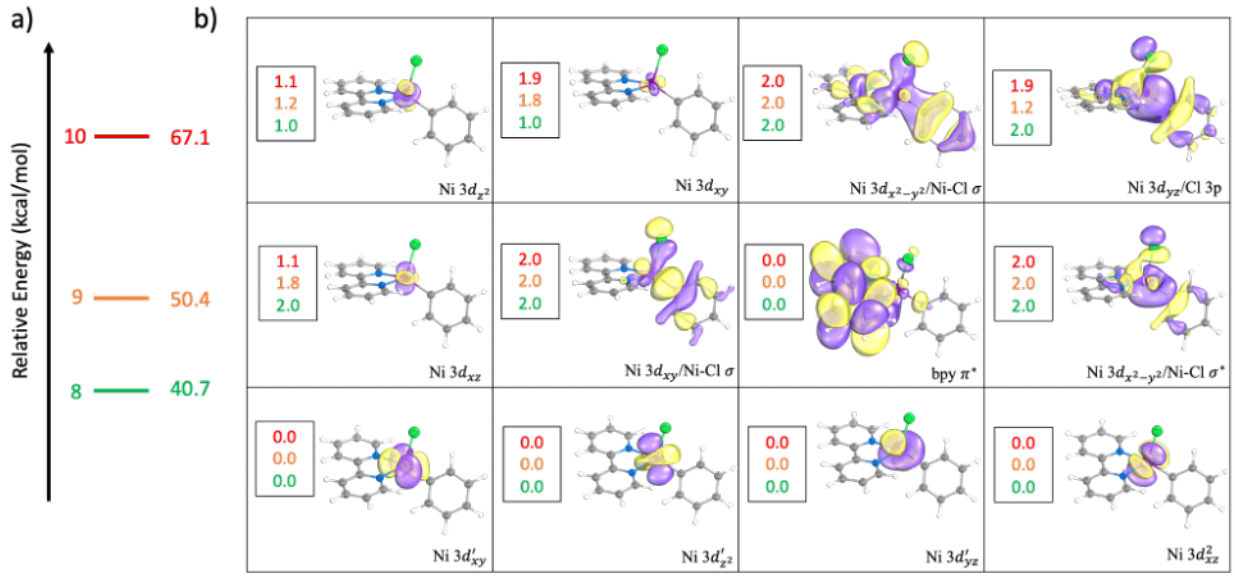

Figure 5.7: a) Energies relative to the ground state singlet of all triplet excited states in the accessible range for $(bpy)Ni^{II}(Ph)Cl$. Excited states 8, 9, and 10 are green, orange, and red respectively. b) Active space orbitals and occupation numbers (inset) of excited states within a 40-70 kcal/mol range from ground state for $(bpy)Ni^{II}(Ph)Br$. Excited state colorings are same as in part a). The Ni-Br and Ni-Ph bonds are in the xy-plane, nearly aligned to the x and y-axis, respectively. Excited state colors in the figure: 5-pink, 6-black, 7-blue, 8-green, 9-orange, 10-red, and 11-purple.

5.3.3 EnT vs. SET Mechanism

Among the excited states of (bpy)Ni^{II}(Ph)X (Figure 7), states 5 and 9 for Br and 9 for Cl are the only ones suitable for Ni-Br homolysis along the M1 pathway, as they have a singly occupied Br orbital and a doubly occupied Ni-Br σ^* orbital. States 6, 7 and 11 for Br and 10 for Cl are instead suitable for heterolytic dissociation of the Ni-Br bond, that would produce $[(bpy)Ni^{III}(Ph)]^+$ and Br–, as shown in Figure 5. Therefore, we are only interested in excited states 5 and 9 for Br and 9 for Cl analogues. These states would result in a homolytic dissociation as the Ni and X charge would be shared between the Ni and X based on the location of the single electron on the system. In one of the singly occupied orbitals for these states there is significant density on the Br atom and the Ni. This balanced distribution of electron density would likely result in a homolytic dissociation of the Ni-X bond. Furthermore, based on this orbital composition analysis, we predict that these states could be the results of double electron exchange via Dexter mechanism, as shown in Figure 5.9.[152]

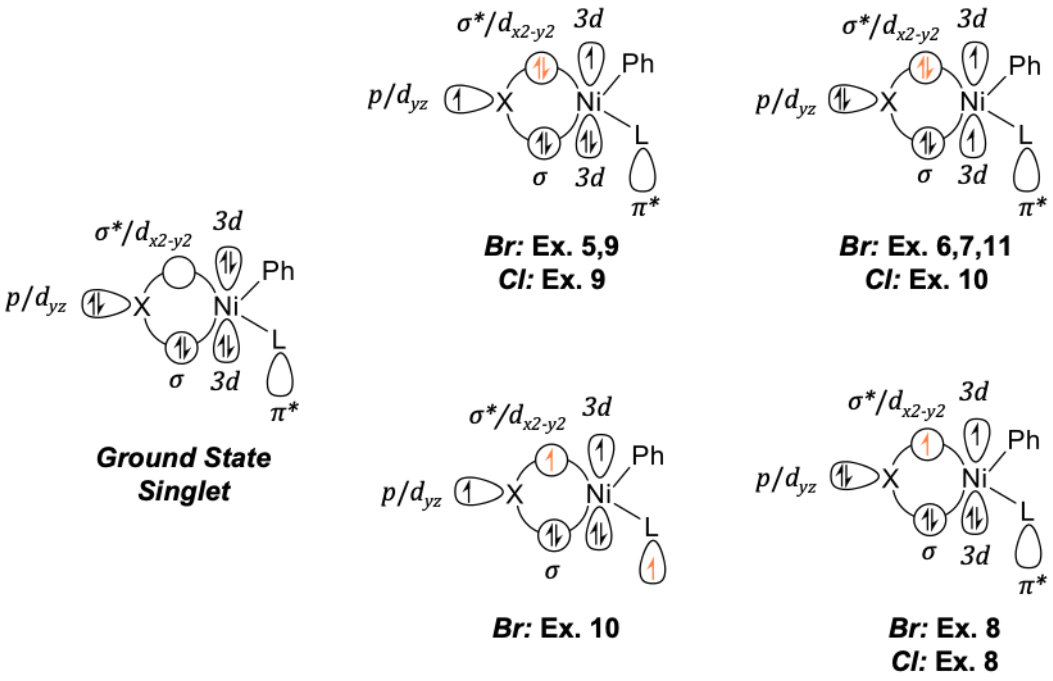

Figure 5.8: Schematic representation of the dominant configurations for excitations that would lead to Ni-X bond breaking from the triplet (bpy)Ni^{II}(Ph)X manifolds. Each of the lobes represent an orbital from the reference wavefunction and the electrons represent of occupation of each orbital in the dominant configuration.

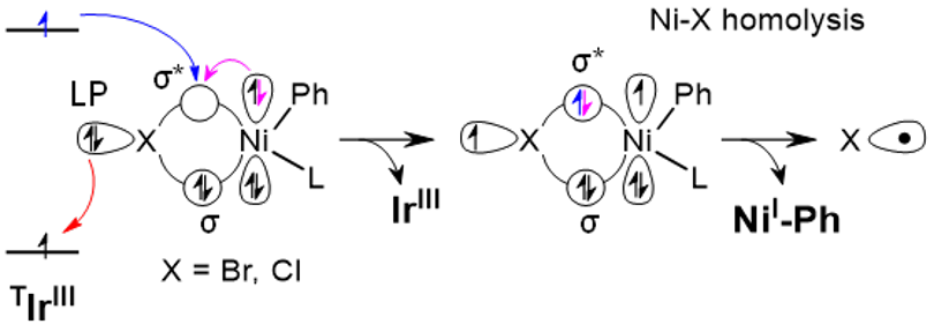

Figure 5.9: Schematic representation of the Dexter EnT step from $^{T}\mathbf{Ir^{III}}$ to (bpy)Ni^{II}(Ph)X, leading to the (bpy)Ni^{II}(Ph)X excited states relevant for Ni-X homolytic dissociation.

Along the **M2** pathway, the multireference treatment on $[(bpy)Ni^{III}(Ph)Br]^+$ clearly indicates that no excited state can been found in the visible light region responsible for the Ni-Br dissociation. Consistently, the Ni–Br bond gets stronger upon oxidation of $(dtbbpy)Ni^{II}(Ph)Br$ to $[(dtbbpy)Ni^{III}(Ph)Br]^+$ (Figure S5). Differently, the Ni–Ph bond becomes weaker after oxidation, which indicates that Ni–Ph bond dissociation is favored over Ni-Br bond in $[(dtbbpy)Ni^{III}(Ph)Br]^+$. This finding is supported by stoichiometric experiments using $(dtbbpy)Ni^{II}(Ar)Cl$, where an external oxidant was used instead of a photocatalyst. In these conditions Ar–H was observed as major product, which is supporting the formation of Ar•.[127] Therefore, we conclude that the **M2** (SET) mechanism is not operative in Ir-Ni dual catalyzed C_{sp3}-H arylation, while **M1** (EnT) is the favored pathway. Similarly, the multireference calculations indicate that the **M1** pathway is operative also for the chloro analogue.

5.4 Conclusion

We elucidated the reaction mechanism of Ir^{III}-Ni^0 catalyzed α-alkoxy Csp3–H arylation starting from the prototype $LNi^{II}(Ar)X$ (X = Br, Cl) complexes by performing electronic structure calculations. Three different pathways, one involving a EnT step and two involving a SET step were considered, depending on the role of the Ir photocatalyst to activate the $LNi^{II}(Ar)X$ intermediate. TD-DFT and HMC-PDFT calculations were used to explore the excited states of the nickel complexes involved in the Ni–X bond homolysis to generate a halide radical, which is crucial in the following C_{sp3}–H activation step. With this investigation, we were able to resolve the ongoing experimental debate regarding the mechanism for the dual photo-catalysis and explain the preference of the EnT mechanism over the SET mechanism by understanding the underlying electronic structure.

Along the EnT pathway energy transfer from the light-excited triplet Ir-photocatalyst to $LNi^{II}(Ph)X$ enables Ni-X bond homolysis to generate X• for C_{sp3}–H activation. Our analysis of $(bpy)Ni^{II}(Ph)Br$

excited states allowed us to identify five states involving Br orbitals and within the range compatible with the irradiating light source. Out of these states we identified two specific states that had a doubly occupied $\sigma^*/d_{x^2-y^2}$ orbital involving the Ni-Br bond and singly occupied Br $3p/d_{yz}$ orbital and Ni 3d orbital. The multireference HMC-PDFT results suggest, for the first time, that this excited state is responsible for the homolytic dissociation of Ni-Br, which can be generated by Dexter EnT from the excited triplet Ir-photocatalyst to the ground state of (bpy)Ni^{II}(Ph)Br. The formation of the doubly occupied Ni-Br $\sigma^*/d_{x^2-y^2}$ orbital occurs with the donation of one electron from TIr^{III} and another from a Ni($3d_{z^2}$) orbital, while the formation of the singly occupied $3p/d_{yz}$ orbital occurs by transfer of one electron from (bpy)Ni^{III}(Ph)Br to the Ir-photocatalyst.

Differently, among the two SET pathways, one involves $1e^-$ oxidation of LNi^{II}(Ph)Br by the Ir-photocatalyst, which leads to $[LNi^{III}(Ph)Br]^+$ that might produce Br• via photoexcitation. Our analysis of the $[LNi^{III}(Ph)Br]^+$ excited states indicated that the first state with a doubly occupied Ni-Br σ^* orbital is located more than 100 kcal/mol above the ground state, and thus cannot be populated with the light sources used experimentally. This suggests that $[(bpy)Ni^{III}(Ar)Br]^+$ is not involved in the reaction pathway, excluding this SET pathway. The other SET pathway can be also excluded, as it requires the highly endothermic 1e- reduction of LNi^{II}(Ph)Br by the Ir-photocatalyst. Our analysis of the Cl analogues indicated a similar photo-chemical scenario, suggesting that a Dexter EnT step should be operative also in the case of Ni-Cl homolytic dissociation.

Overall, our work explains with no ambiguity the operative mechanism for Ni-halide homolytic dissociation, a fundamental step in Ir^{III}-N^0 dual photocatalysis for the activation of inert C_{sp3}-H bonds for C_{sp3}-C_{sp2} cross-coupling reactions. This mechanism involves Dexter EnT from the Ir-photocatalyst to the Ni-complex. The electronic structure characterization we provided for the excited states of LNi^{II}(Ar)X can constitute the basis for future directions of the excited state catalysis for C_{sp3}-H cross-coupling reactions.

This work has been submitted for publication.

CHAPTER 6

INTRASTRAND PHOTOLESION FORMATION IN THIO-SUBSTITUTED DNA: A CASE STUDY INCLUDING SINGLE-REFERENCE AND MULTIREFERENCE METHODS

6.1 Introduction

Thionucleobases are canonical DNA nucleobase analogues in which a carbonyl group has been replaced by a thiocarbonyl group. This modification in the structure of DNA monomers induces dramatic changes in their photophysics and photochemistry as compared to natural DNA nucleobases,[14,153] and these changes have been exploited by the pharmaceutical industry.[154–158] Thionucleobases, unlike canonical nucleobases, are UVA chromophores, as sulfur incorporation into the biomolecule causes a bathochromic shift in their absorption maximum.[14,153] Additionally, the topography of the excited-state potential energy surfaces of the thio-derivatives differs significantly from that of canonical nucleobases. The potential energy surfaces (PESs) of the states populated following photon absorption in natural nucleobases are characterized by barrierless downhill pathways that connect the Franck–Condon region with S_1/S_0 conical intersections, and the rapid decay via these pathways confers the characteristic photostability of the natural nucleobases.[159,160] Although energetically accessible singlet–triplet interacting regions have been located along the main decay paths of nucleobases,[161] the experimental triplet quantum yields observed for natural nucleobases vary between 0.001 and 0.4,[162–165] relegating triplet states to a relatively minor role in the photophysics of these systems. Conversely, the population of the triplet excited states in thionucleobases is well documented, not only in the gas phase or in solution[14,153] but also when embedded in a biological environment. In thionucleobases, the populated spectroscopic state decays to the S_1 state, whose PES is characterized by the presence of one or several minima that can be accessed via internal conversion processes. A relevant feature of thionucleobases is the energetic proximity of the triplet states at the position of the singlet

minima; this proximity, when combined with the heavy-atom effect introduced by the incorporation of a sulfur atom into the system, results in significantly large values of spin–orbit coupling, facilitating the transfer of population from the singlet to the triplet manifold. This explains the unusually high quantum yields of triplets that induce deleterious chemical reactions[14,153] in thiated DNA.[166,167]

The fates of the triplet states of thionucleobases depend strongly on the molecular environment. If the monomer is in solution, an energy transfer process with ground-state oxygen molecules in the environment can produce cytotoxic singlet oxygen.[167–169] However, when thionucleobases are inserted along a DNA strand, exposure to UVA light can trigger photochemical reactions and the formation of covalent photoproducts. Clivio and co-workers isolated and characterized the thietane intermediate, a precursor of the 6-4 pyrimidine–pyrimidone photoproduct (6-4PP), when irradiating thymidylyl(3'-5')-4-thiothymidine with 360 nm light.[170] This intermediate, structure SI2 in fig. 6.1 is the result of a [2+2] cycloaddition reaction between the C5–C6 bond of a canonical thymine (for the atom labeling, see fig 6.1) and the C=S bond of an adjacent 4-thiothymine. Next, the H sitting on the N'3 (the prime denotes the atoms of the thionucleobase) of the thionucleobase migrates to the S atom, activating the C_5–S bond and leading to the final 6-4PP (structure SP1 in fig. 6.1). According to recent theoretical and experimental works, the last steps of the dimerization reaction would take place along the T_1 and S_0 profiles, accessed from intersystem crossing processes (S_1/T_1 and S_1/T_2) from the S_1 minima where significant spin–orbit coupling (SOC) values were recorded (94.1-69.2 cm^{-1}),[171] consistent with an intersystem crossing lifetime of 3 ps.[172]

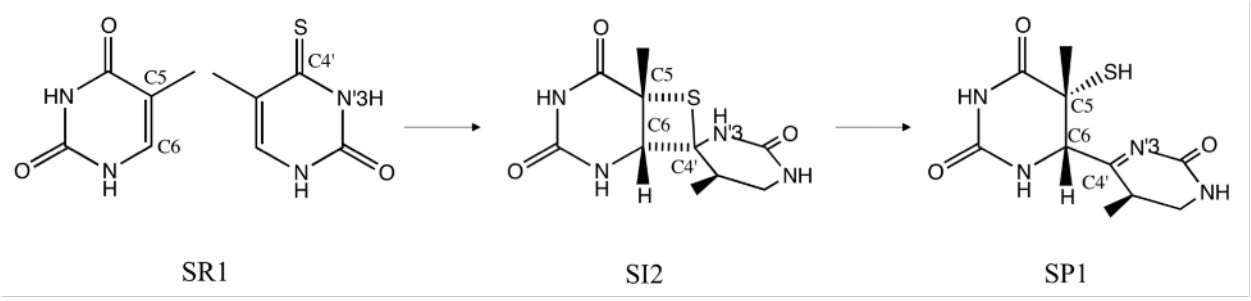

Figure 6.1: Steps Leading to 6-4PP Formation in the Thymine–4-Thiothymine Dimer

The 6-4PP is one of the most abundant lesions in genetic material (second only to cyclobutane pyrimidine dimers). Analogous reaction steps to those in figure 6.1 have been proposed for canonical DNA when continuously exposed to UV light;[173] however, the mechanism of the 6-4PP formation in DNA is still controversial because the role that the triplet excited states play in the mechanism is unclear.[174–176]

In many molecules, excited states are strongly correlated and often require the use of multireference methods for their accurate quantum-mechanical description.[177] The multireference methods considered here start with a complete active space self-consistent field (CASSCF) calculation, which includes a portion of the correlation energy called internal correlation energy. (If the active space is well chosen, this includes all the static correlation energy and a portion of the dynamic correlation energy). Complete active space second-order perturbation theory[89,151] (CASPT2) in its various versions, such as multistate-CASPT2[178] (MS-CASPT2) and extended-multistate-CASPT2[179] (XMS-CASPT2), then incorporates another portion of the correlation energy, called the external correlation energy. Unfortunately, these approaches are computationally unaffordable for many relevant biological systems.

Multiconfiguration pair-density functional theory[17] (MC-PDFT) combines the realistic representation of multiconfigurational character by CASSCF theory with the computational efficiency of including external correlation by using a density functional treatment that aims to capture all the

correlation energy. In particular, MC-PDFT calculates the energy without separating it into internal and external parts. It does this through the use of an on-top functional created by translating exchange–correlation functionals[39] from Kohn–Sham density functional theory (KS-DFT). The results obtained by this method are in many cases comparable in accuracy to those obtained with CASPT2, but the computational cost (computer time and memory) is closer to the less expensive CASSCF method, and this allows its employment for larger systems.

For treating excited states, we employ state-interaction pair-density functional theory[180] (SI-PDFT), which is an extension of MC-PDFT, similar to the MS-CASPT2 extension of CASPT2. The SI-PDFT method includes the coupling between states that is crucial for the correct characterization of regions of the potential energy surface where two or more states of the same symmetry are close in energy or degenerate. Such crossings can play an important role in the deactivation mechanism of photoactive systems, such as the one studied here.

The 6-4PP generation mechanism was previously studied with KS-DFT,[181] which is a single-reference method, and with a combined quantum-mechanical and molecular mechanical (QM/MM) method in which the QM method is MS-CASPT2//CASSCF. In the latter case, the dimer was inserted in a 7-pair double-stranded DNA embedded in a rectangular water box.[171]

The aim of the present work is twofold. On the one hand, we revisit the mechanism of the last stages of 6-4PP generation in a dinucleoside monophosphate containing a thymine and a 4-thiothymine after the excited system has decayed to the lowest lying T_1 triplet and S_0 states, accessed from internal conversion and/or intersystem crossing processes as described in Xie's paper.[171] And on the other hand, we assess the performance of different mon and multiconfigurational methods in the description of the 6-4PP generation in S_0 and T_1 manifolds and in the prediction of the energies of the excited states. In particular, we examine the state-averaged MC-PDFT (SA-PDFT), SI-PDFT, KS-DFT, and unrestricted KS-DFT (UKS-DFT) with molecular mechanical damped dispersion, linear response time-dependent KS-DFT,[182] and the Tamm Dancoff approximation[148] to time-dependent KS-DFT, taking as a reference MS-CASPT2 results.

For brevity, we will denote linear-response time-dependent KS-DFT with a prefix TD, and we will denote the Tamm–Dancoff approximation to time-dependent KS-DFT by the prefix TDA. The use of TDA-DFT is motivated by the well-known triplet instabilities of full-linear-response TD-DFT in near-degeneracy regions.[149,183]

We also give results for the state-averaged CASSCF (SA-CASSCF) reference wave functions on which the MS-CASPT2, SA-PDFT, and SI-PDFT calculations are based. Additionally, we compare to the results of Zou and co-workers[181] employing KS-DFT with the M06-2X exchange-correlation functional.[142] The QM/MM results[171] will be excluded from the comparison, since the severe constraints imposed by the biological surroundings included in that calculation can significantly affect the geometries of the dimer and the energetics of the process.

6.2 Computational Methods

All the starting structures were taken from the work by the group of Eriksson on 6-4PP formation in a natural thymine–thymine dimer by appropriate replacement of a C=O by a C=S group.[173] Full geometry optimizations (63 atoms) along the ground and T_1 states, including both the ribose phosphate backbone and the two nucleobases, and a harmonic vibrational frequency analysis to classify the character of the stationary points were performed by using KS-DFT as implemented in version 3.0.3 of the ORCA software.[184] The hybrid functional B3LYP[185] complemented with the D3 dispersion correction[139] was used with the cc-pVDZ basis set.[186,187] To speed up the calculations, we employed the density fitting approximation RIJCOSX,[144] which decomposes the usual four-center two-electron integrals into three-center integrals using the cc-pVDZ/J[185] auxiliary basis set.

In contrast to the work of Zou et al.,[181] all the minima and transition states for the lowest-lying singlet and triplet states were optimized without constraints.

Ground-state and T_1 potential energy profiles and vertical excitation energies for the lowest-lying singlet and triplet excited states were computed by TD-DFT, TDA-DFT, SA-CASSCF, MS-

CASPT2, SA-PDFT, and SI-PDFT at the optimized geometries from B3LYP-D3.

To correctly describe charge-transfer states at the TD-DFT and TDA-DFT level, the CAM-B3LYP[188] functional was used, and these calculations will be termed TD-CAM-B3LYP and TDA-CAM-B3LYP, respectively. All single-point calculations with TD and TDA methods were performed by using the Gaussian 09 software package.[137]

The SA-CASSCF calculations use an active space of 12 electrons in 11 orbitals. This active space has more configuration state functions than the (14,11) active space employed by Xie et al.[171] because it includes π and π^* orbitals that in the later stages of the mechanism evolve into the σ orbitals involved in the new covalent bond between the two nucleobases. In particular, our active space includes two pairs of π and π^* orbitals on each nucleobase localized over the C'$_4$–S and C_5–C_6 bonds (recall fig. 6.1). Also in contrast to the work by Xie,[171] the sigma C'$_4$–S bonding and antibonding orbitals were included, as the breaking of the C–S bond is a critical step in the reaction mechanism. Finally, the lone pair of the sulfur atom was included as this orbital was found to be necessary for a correct description of the last steps of the reaction. The orbitals of the active space are collected in figure 6.2.

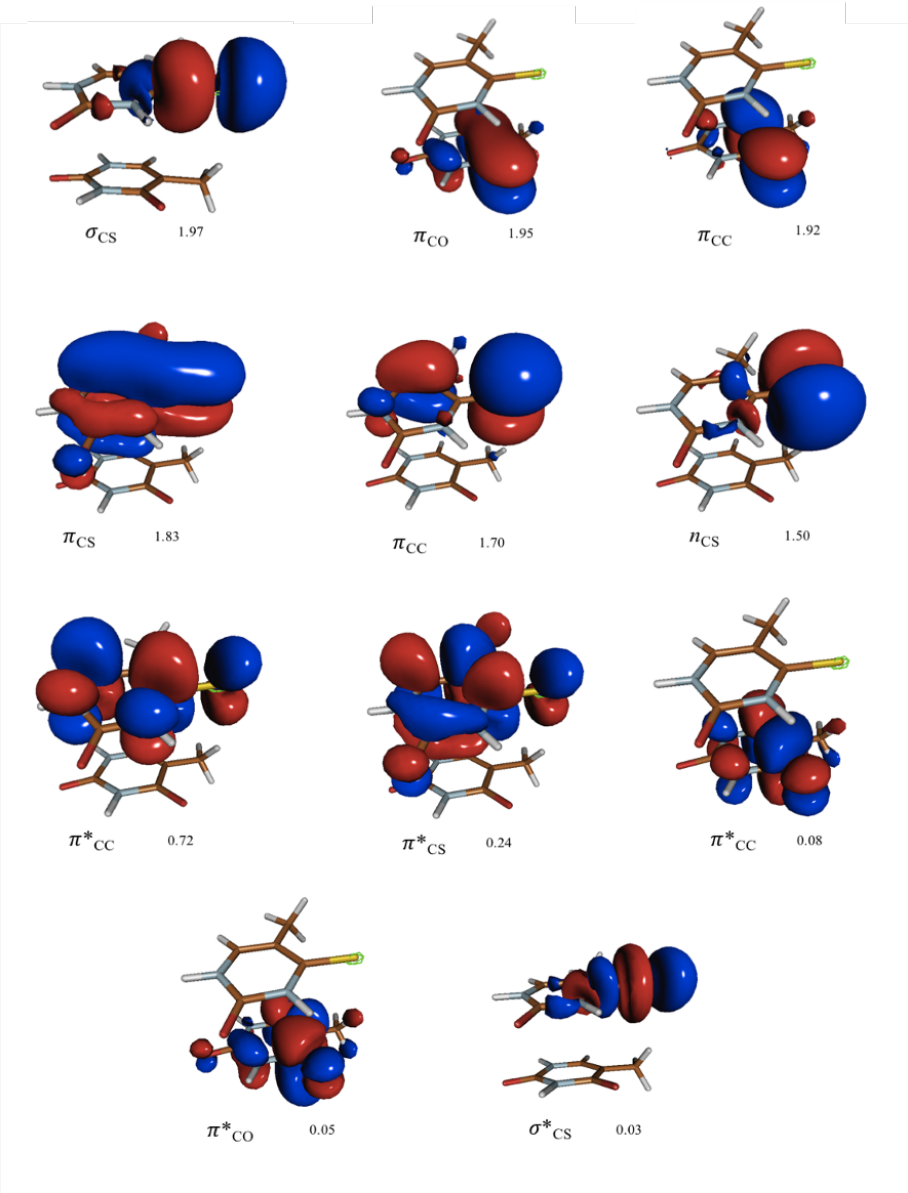

Figure 6.2: SA-CASSCF/cc-pVDZ orbitals with their occupation numbers included in the (12,11) active space employed in the multireference calculations at the ground-state SR1 structure. The sugar–phosphate DNA backbone has been omitted from the figure for clarity.

The SA-CASSCF calculations over three singlet states failed to converge for all the geometries explored when using the same set of active orbitals. To preserve the desired active space and in

particular to ensure that the sulfur lone pair orbital is not rotated out of the active space, the number of roots in the multireference singlet and triplet single-point calculations had to be increased to four singlet and three triplet equally weighted states, respectively. All multireference calculations were performed by using the OpenMolcas program,[48] employing density fitting (RICD).[91] Two different protocols were followed for the CASSCF calculations. First, nonrelativistic calculations were undertaken by using the cc-pVDZ basis set (604 basis functions).

The MS-CASPT2 calculations were performed with a real level shift of 0.3 au[189,190] to avoid intruder states and the default IPEA shift of 0.25 au, and all the orbitals except for the core orbitals were included in the correlation treatment. In the SA-PDFT and SI-PDFT calculations the translated PBE[191] functional (tPBE) was employed.

With the purpose of analyzing the multireference character of the stationary points along the S_0 and T_1 manifolds reported in this work, an M diagnostic[192] was carried out based on SA-CASSCF wave functions.

6.3 Results

6.3.1 Ground-State Mechanism

The ground-state (S_0) potential energy profile for 6-4PP consists of two reaction steps as shown in Figure 6.3. In the reactant structure SR1, the two nucleobases are arranged in a stacked position. The density functional approximation used here, B3LYP-D3, preserves the stacked arrangement of the dimer and prevents coplanarization with hydrogen bond interactions as Zou and co-workers report with the M06-2X functional.[181] As the reaction proceeds, the aromatic rings approach each other, and a [2 + 2] cycloaddition takes place between the C_5–C_6 double bond of thymine and the C'$_4$–S bond of the thiocarbonyl group of 4-thiothymine, passing through transition structure STS1 and forming the thietane intermediate SI2. This high-energy four-membered ring opens via transition structure STS2 corresponding to the transfer of the sulfur atom from the thionucle-

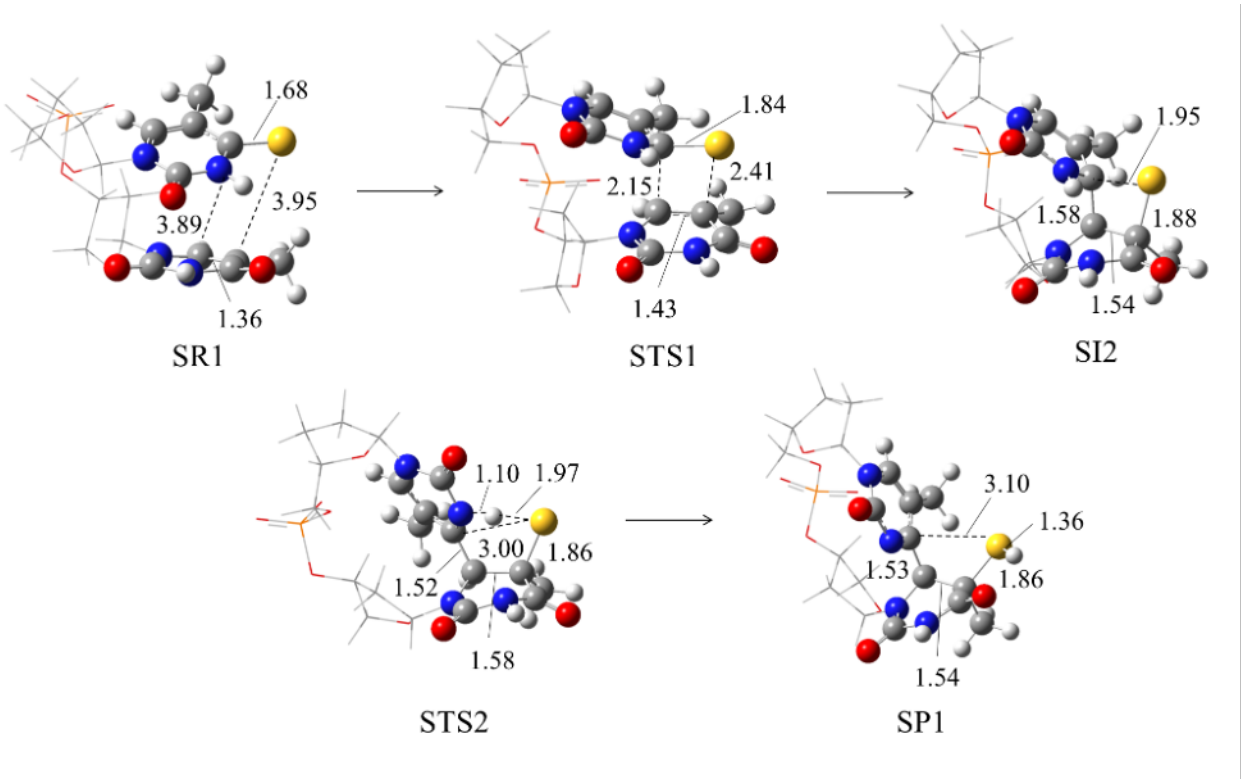

Figure 6.3: Stationary points of the ground-state mechanism for 6-4PP formation with structures optimized by B3LYP-D3/cc-pVDZ. Selected bond distances are shown in Å. Color coding for atoms: C, gray; H, white; N, blue; O, red; S, yellow.

obase to the canonical nucleobase in concert with the migration of a hydrogen from N'$_3$ to the S, resulting in the final 6-4PP, structure SP1. An equivalent mechanism was optimized by Zou and co-workers.[181]

The key bond distances of the B3LYP-D3 optimized geometries for the various stationary points along the singlet mechanism are reported in Figure 6.3. Small differences were observed between the B3LYP-D3 structures obtained here and the M06-2X structures reported by Zou and co-workers.[181] In general, the bond lengths between the C_5, C_6, C'$_4$, and S atoms (see fig 6.1), which are directly involved in the dimerization process, are slightly longer with B3LYP-D3; specifically, the B3LYP-D3 C_5–C_6, C_4–S, and S–C_5 bond lengths, averaged over all the stationary points in the mechanism, are 0.02, 0.04, and 0.07 Å longer than those predicted by M06-2X,[181] respec-

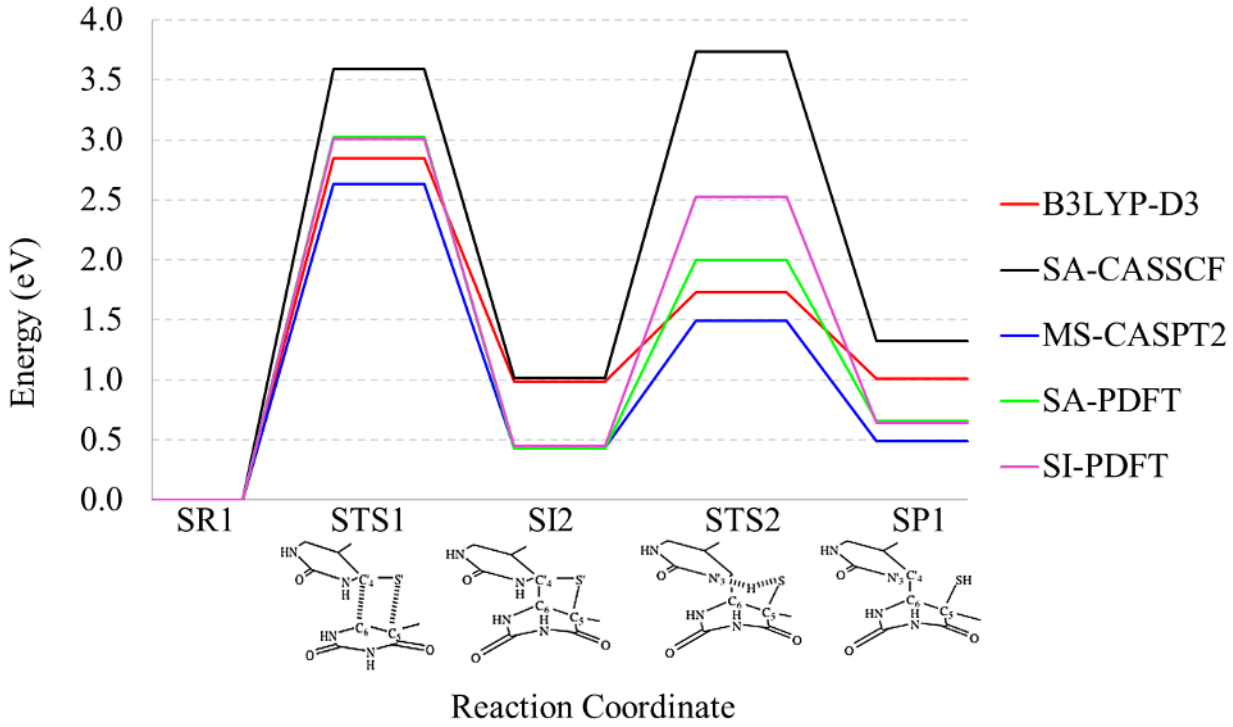

Figure 6.4: Potential energy profiles for 6-4PP formation in the S_0 state at different levels of theory: B3LYP-D3, red line; SA-CASSCF, black line; MS-CASPT2, blue line; SA-PDFT, green line; and SI-PDFT, pink line. The cc-pVDZ basis set was used throughout. Energies are in eV relative to the SR1 ground-state equilibrium structure. All geometries in this profile were optimized at the B3LYP-D3/cc-pVDZ level.

tively. By contrast, the newly formed C_6–C'_4 bond distance is predicted to be very similar or even larger by M06-2X.[181].

Using these optimized geometries, we calculated the S_0 potential energy profiles for the 6-4PP reaction at the SA-CASSCF, MS-CASPT2, SA-PDFT, and SI-PDFT levels of theory; all these calculations use the cc-pVDZ basis set. The polarization functions from cc-pVDZ have an overall stabilizing effect along the entire potential energy curve with this effect being more pronounced for the second step of the reaction.

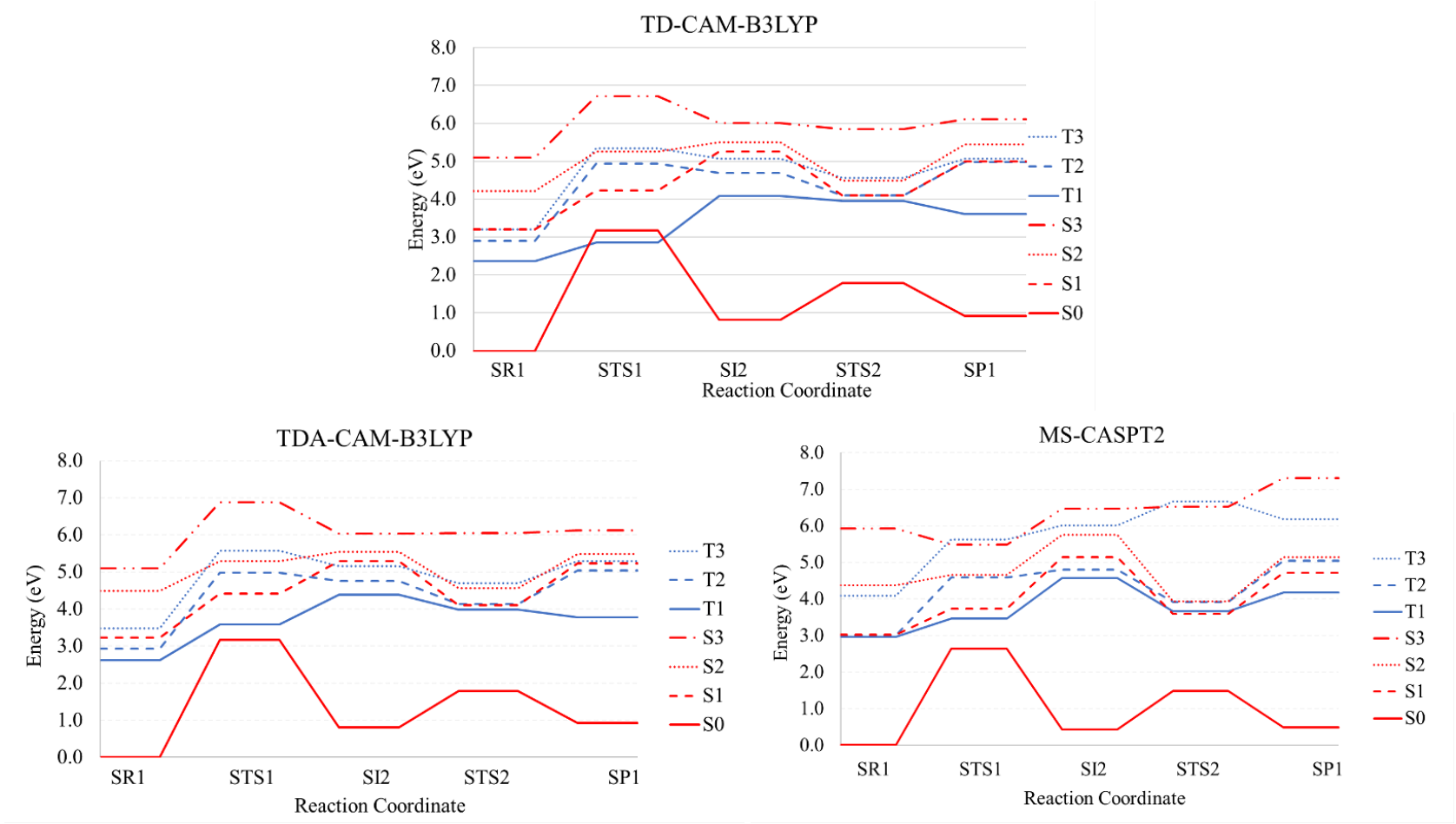

Figure 6.5: Potential energy profiles for the lowest singlet and triplet states along the ground-state reaction coordinate leading to 6-4PP formation, computed at the TD-CAM-B3LYP, TDA-CAM-B3LYP, MS-CASPT2, SA-PDFT, and SI-PDFT levels of theory. The cc-pVDZ basis set was used throughout. Energies are in eV relative to the SR1 ground-state equilibrium geometry. All geometries in this profile were optimized at the B3LYP-D3/cc-pVDZ level (same as in Fig. 2).

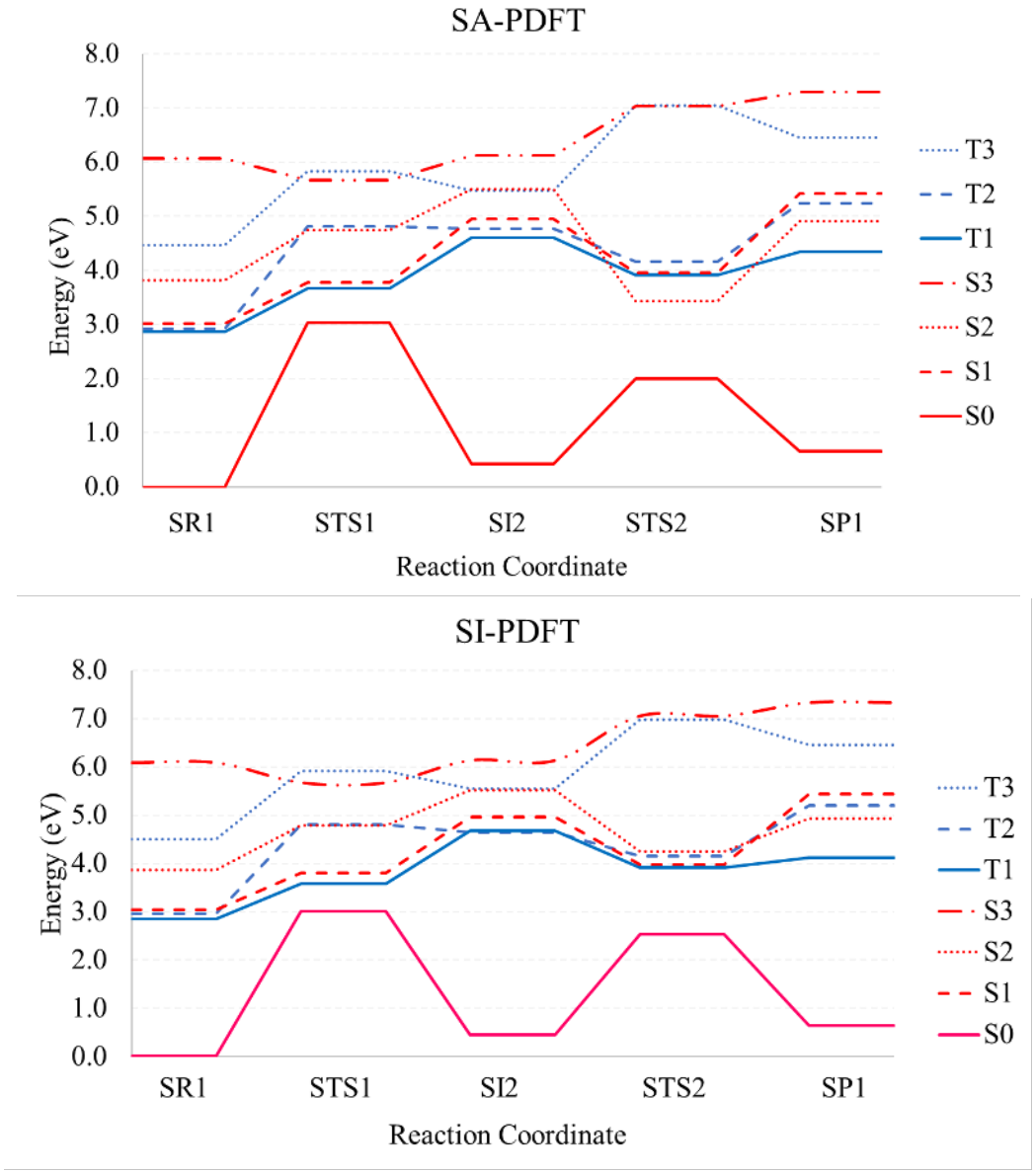

Figure 6.6: Potential energy profiles for the lowest singlet and triplet states along the ground-state reaction coordinate leading to 6-4PP formation, computed at the TD-CAM-B3LYP, TDA-CAM-B3LYP, MS-CASPT2, SA-PDFT, and SI-PDFT levels of theory. The cc-pVDZ basis set was used throughout. Energies are in eV relative to the SR1 ground-state equilibrium geometry. All geometries in this profile were optimized at the B3LYP-D3/cc-pVDZ level (same as in Fig. 2).

As shown in Figure 6.4, the SA-CASSCF method overestimates not only the energies of the transition states but also the energies of the intermediate, SI2, and product, SP1, when compared to MS-CASPT2 results. This is especially apparent for the energy of the STS2 transition state where the barrier is overestimated by 2.24 eV, considering the MS-CASPT2 results as a reference. This step in the dimerization involves the simultaneous breaking of two bonds, i.e., C'$_4$–S, and the transfer of the N'$_3$ proton to the S atom, requiring a better treatment of electron correlation. The other methods included in this study generally provide results comparable to MS-CASPT2. Similar potential energy profiles are obtained with B3LYP-D3 and M06-2X,[181] the latter predicting more stable minima (by 0.4–0.5 eV). The difference in the energy between B3LYP-D3/M06-2X and MS-CASPT2 results of the STS2 structure is 0.2 eV. However, the B3LYP-D3 and M06-2X calculations overestimate the energy of the SI2 intermediate by 0.6 and 0.1 eV, respectively, and the height of the STS1 energy barrier by 0.2 eV, compared to MS-CASPT2.

Both SA-PDFT and SI-PDFT significantly differ with respect to the MS-CASPT2 results for the transition states, overestimating the barrier heights by 0.4 eV for STS1 and by 0.5 and 1.0 eV, respectively, for STS2. For the minima, the MS-CASPT2 and both PDFT results are in reasonable agreement, the largest gap amounting to 0.15 eV. The comparison of the energies for the minima delivered by B3LYP-D3 and PDFT theories reveals a poorer agreement of the former with respect to MS-CASPT2, suggesting that at these points a better treatment of static and dynamic correlation is necessary for the correct description of the nucleobase dimerization mechanism.

In the following, we will assess the performance of all the methods included in our survey in the description of the excited-state potential energy profiles along the global coordinate defining the ground-state mechanism.

Table 6.1 collects the calculated energies and—for the singlet states—the oscillator strengths of the lowest excited states of the reactant SR1. The obtained results indicate that the first bright excited state is S_2. This electronic state has $\pi\pi^*$ character according to all methods, with an

important contribution from the C=S group. MS-CASPT2 predicts the vertical excitation energy of this bright state to be 4.38 eV. A similar vertical excitation energy is obtained by TD-CAM-B3LYP (4.21 eV) and TDA-CAM-B3LYP (4.49 eV), with the latter being in good agreement with the reference MS-CASPT2 value. The SA-PDFT and SI-PDFT methods predict lower vertical excitation energies for the spectroscopic state S_2 by about 0.6 eV compared to MS-CASPT2, while SA-CASSCF predicts a vertical excitation energy about 0.6 eV higher than MS-CASPT2. Figure 6.5 and 6.6 collects the energies of the lowest singlet and triplet excited states along the ground-state reaction coordinate.

From the results in Figure 6.9, we conclude that multireference methods deliver similar excited-state potential energy profiles. Significant differences are found between the multiconfigurational profiles and those obtained by the single reference methods, TD-CAM-B3LYP and TDA-CAM-B3LYP. The most striking difference is the TD-CAM-B3LYP and TDA-CAM-B3LYP overstabilization of the T_1 and T_3 states, which both show $\pi\pi^*$ character. In particular, at the SR1 geometry the T_1–S_0 and T_3–S_0 energy differences are respectively 0.6 and 0.9 eV smaller than the corresponding MS-CASPT2 values. The T_3 state at the SI2 and STS2 positions is overstabilized by 0.94 and 2.10 eV, respectively, using TD-CAM-B3LYP and by 0.85 and 1.97 eV, respectively, using TDA-CAM-B3LYP. These changes translate into a qualitative change of the T_3 landscape in the later stages of the dimerization reaction as compared to multireference methods.

Another important difference is found at the STS1 position, where TD-CAM-B3LYP predicts the T_1 state to be lower in energy than the S_0 state. This pathological behavior is corrected when the Tamm–Dancoff approximation is applied, supporting the conclusion that this method is less sensitive to triplet instability and is recommended with long-range corrected hybrid functionals.[193]

The T_1 state can be computed by UKS-DFT, and the comparison with the TD-DFT results is shown in Figure 6.7. The B3LYP-D3 T_1 profile calculated by UKS is always higher in energy than the ground state with the smallest energy gap along the profile being 0.47 eV, which is similar to the one obtained by using the TDA protocol (0.41 eV) but still rather different than what is seen

	MS-CASPT2		TD-CAM-B3LYP		TDA-CAM-B3LYP		SA-CASSCF	
state	ΔE	f	ΔE	f	ΔE	f	ΔE	f
$S_1(n_S\pi^*_S)$	3.03	0.00002	3.21	0.0003	3.22	0.0003	2.92	0.00001
$S_2(\pi_S\pi^*_S)$	4.38	0.31	4.21	0.31	4.49	0.41	5.02	0.35
$S_3(n\pi^*)$	5.92	0.0002	5.09	0.004	5.10	6.06	0.006	
$T_1(\pi_S\pi^*_S)$	2.97		2.37		2.62		2.86	
$T_2(n_S\pi^*_S)$	3.00		2.90		2.93		2.89	
$T_3(\pi\pi^*)$	4.09		3.21		3.48		3.95	

	SA-PDFT		SI-PDFT	
state	ΔE	f	ΔE	f
$S_1(n_S\pi^*_S)$	3.02	0.00001	3.04	0.00001
$S_2(\pi_S\pi^*_S)$	3.81	0.37	3.86	0.29
$S_3(n\pi^*)$	6.07	0.0004	6.09	0.0004
$T_1(\pi_S\pi^*_S)$	2.87		2.86	
$T_2(n_S\pi^*_S)$	2.91		2.97	
$T_3(\pi\pi^*)$	4.47		4.50	

Table 6.1: Lowest-Lying Vertical Excitation Energies (ΔE) and Oscillator Strengths (f) (Unitless) of the Reactant SR1[a]

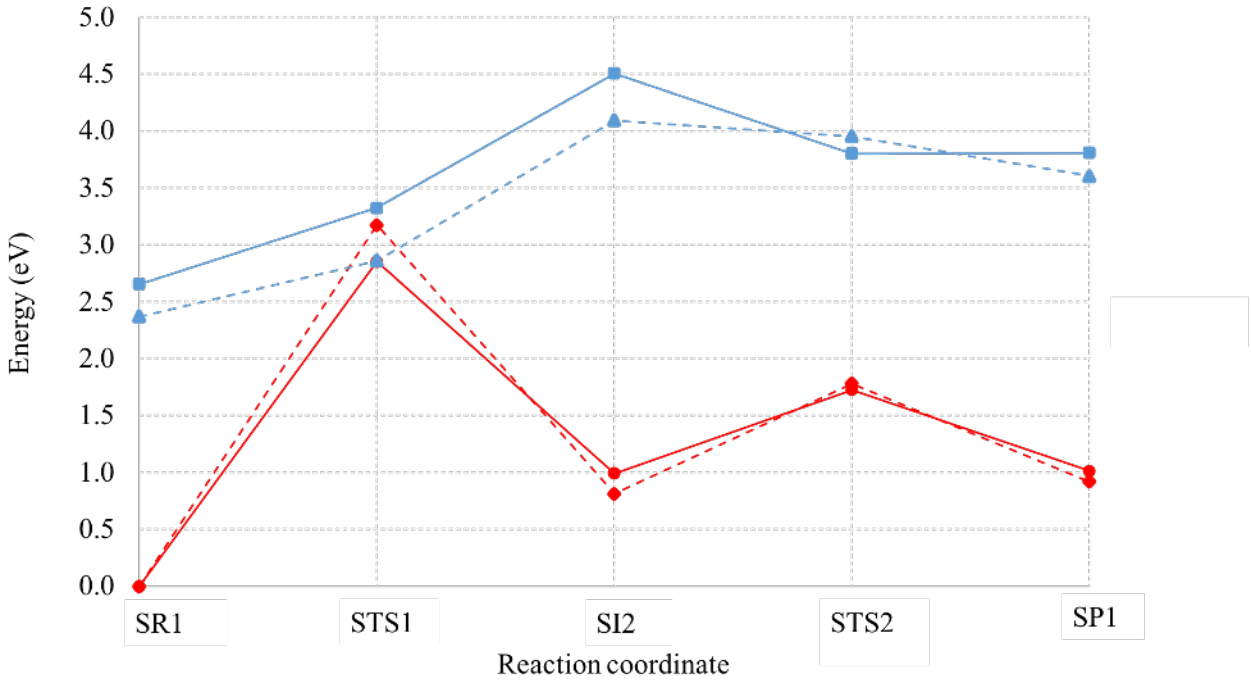

Figure 6.7: Potential energy profiles for the S_0 (red color) and T_1 (blue color) states along the ground-state reaction path leading to 6-4PP formation, computed by UKS calculation with B3LYP-D3/cc-pVDZ (solid lines) and by TD-CAM-B3LYP/cc-pVDZ (dotted lines). Energies are in eV relative to the S_0 state at the SR1 geometry.

with MS-CASPT2 (0.83 eV).

Because the TDA-CAM-B3LYP and UKS-B3LYP-D3 results are very similar, in the lowest triplet excited-state analysis only the UKS-B3LYP-D3 results will be considered as they are less computationally expensive.

Another feature of these PESs that has implications to the reactivity of these systems is that the S_1, T_1, and T_2 states are not degenerate at the TD-CAM-B3LYP profile, while they are degenerate with the multiconfiguration approaches around the SR1 region, and with the TDA formalism, these states are close in energy but not fully degenerate. This failure in the description of the triplet PES by TD-CAM-B3LYP and TDA-CAM-B3LYP might have a direct effect in the photophysics and photochemistry of these systems by missing possible deactivation pathways around the SR1

geometry.

Differences between the single-reference and multireference methods are also observed in the singlet excited states. While the TD-CAM-B3LYP and TDA-CAM-B3LYP S_1 and S_2 state energies agree with the qualitative form of the MS-CASPT2 potential energy curves, the S_3 state energy does not. The S_3 state has a much larger barrier for the STS1 transition state, and the STS2 and SP1 structures are closer in energy than what is predicted by MS-CASPT2.

The comparison of the multireference curves in Figure 6.5 and 6.6 reveals small differences between the SA-PDFT and the MS-CASPT2 methods that are concentrated in the last steps of the reaction pathway, namely, at the SI2 and STS2 structures. SA-PDFT gives a smaller energy of the S_2 and the S_3 states at the STS2 and SI2 structures compared to the reference MS-CASPT2, which leads to interstate crossings that are not observed in MS-CASPT2. However, the SI-PDFT method predicts the same state ordering as MS-CASPT2.

6.3.2 Lowest Triplet Excited-State Mechanism

The high-energy barriers found in the ground-state mechanism hinder the evolution of the 6-4PP reaction through this path and support a photoinitiated mechanism. Moreover, previous theoretical[171] and experimental[172] studies support the participation in the mechanism of triplet electronic states. In particular, the work of Xie et al.[171] localizes five different relaxation pathways to the T_1 state either combining internal conversion (S_2/S_1) and intersystem crossing ($S_2/T_2/T_1$) processes or alternatively accessing the triplet manifold through a four-state intersection ($S_2/S_1/T_2/T_1$). Experimentally triplet species were identified in time-resolved spectroscopic studies, which also recorded moderate triplet quantum yields.[14,166] In view of the importance of the triplet states in the formation of the 6-4PP mechanism, in the following we will evaluate the quality of our pool of methods for the prediction of the triplet energies.

We found that the mechanism for 6-4PP generation in the lowest triplet state is defined by a total of 12 stationary points. Unlike the concerted singlet mechanism, the formation of the intermediate

thietane in the triplet mechanism occurs in two independent steps.

As for the singlet mechanism, in the T_1 reactant, R1, the two nucleobases are in a stacked position (see Figure 6.8). The nucleobases can then undergo two alternative reorganizations that facilitate their approach to generate the thietane. The first mechanism, shown in Figure 6.8a, is called the CC–CS triplet mechanism; it involves bond formation between the C6 of the thymine and the C'4 of the thiothymine (structure I1CC), followed by C_5–S bonding to form the ring (structure I2, Figure 6.9). The second mechanism, shown in Figure 6.8b, is called the CS–CC triplet mechanism; it forms the C_5–S bond first (structure I1CS), and then the thietane is generated by the formation of the C_6–C'_4 bond (structure I2, Figure 6.9).

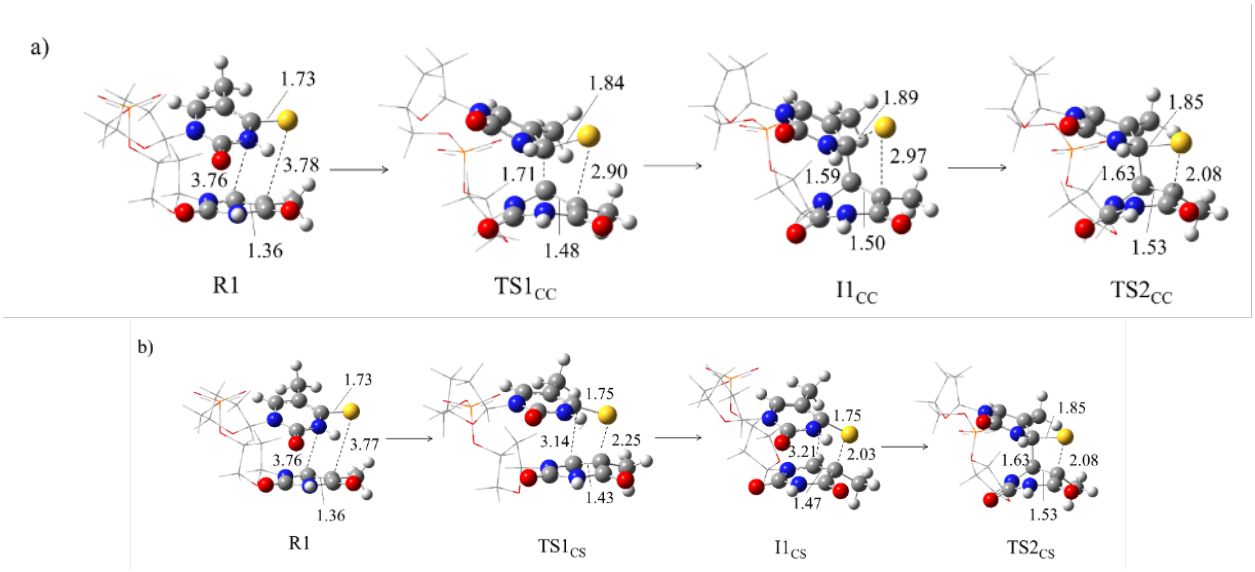

Figure 6.8: Optimized structures for the stationary points in the reaction mechanism for 6-4PP formation for the lowest triplet state by UKS-B3LYP-D3/cc-pVDZ. (a) CC–CS triplet mechanism. (b) CS–CC triplet mechanism. Selected bond distances are given in Å. Color coding for atoms: C, gray; H, white; N, blue; O, red; S, yellow.

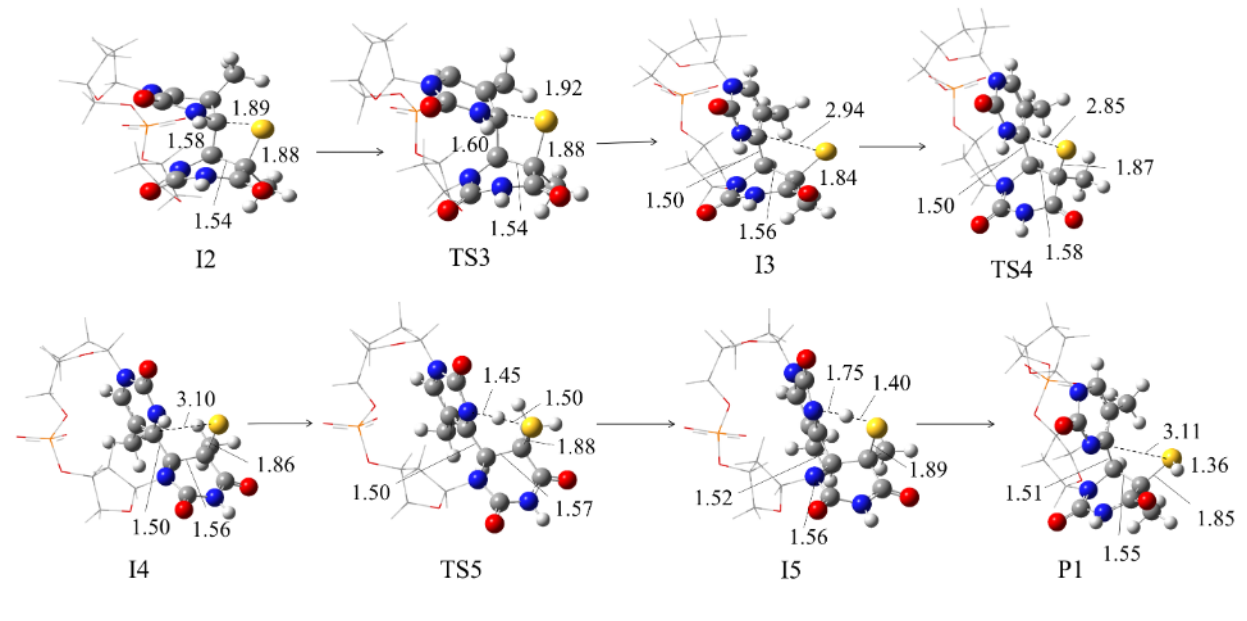

Figure 6.9: Optimized structures for the stationary points of the final steps in the reaction mechanism for 6-4PP formation for the lowest triplet state by UKS-B3LYP-D3/cc-pVDZ. These steps are the same in the CC–CS triplet mechanism and the CS–CC triplet mechanism. Selected bond distances are given in Å. Color coding for atoms: C, gray; H, white; N, blue; O, red; S, yellow.

The last steps are the same in both mechanisms and are shown in Figure 6.9. Once the high-energy thietane is formed, it promptly opens by breaking the C'$_4$–S bond (structure I3), which results in the transfer of the S atom from the original thiothymine to the canonical thymine. In the final step of the mechanism, the system undergoes a dihedral rotation so that the S atom approaches the N'$_3$ atom (structure I4) and facilitates the hydrogen transfer in structure I5. After a final rotation of the SH group, the 6-4PP is formed (structure P1). No previous studies report the last steps of this mechanism that involve the dihedral angle and SH rotation.

A somewhat different scenario was reported by Zou et al.[181] for the last steps of the triplet mechanism. In contrast to our work, Zou et al. predict entirely independent mechanisms for the CC–CS and CS–CC pathways. This overlooks the S dihedral rotation for the preparation of the H

transfer and circumvents the formation of thietane, leading to a sequence of disconnected stationary points. It is also surprising that the highly strained thietane intermediate, located 3.9–4.2 eV above R1 according to our calculations, lies below the initial reactants in the work by Zou et al.[181]

Figure 6.10 shows the profiles for the triplet mechanism investigated by using the UKS-B3LYP-D3/cc-pVDZ geometries optimized for T_1, with energies both by the UKS method and by the multireference methods SA-CASSCF, MS-CASPT2 SA-PDFT, and SI-PDFT, each with the cc-pVDZ basis set.

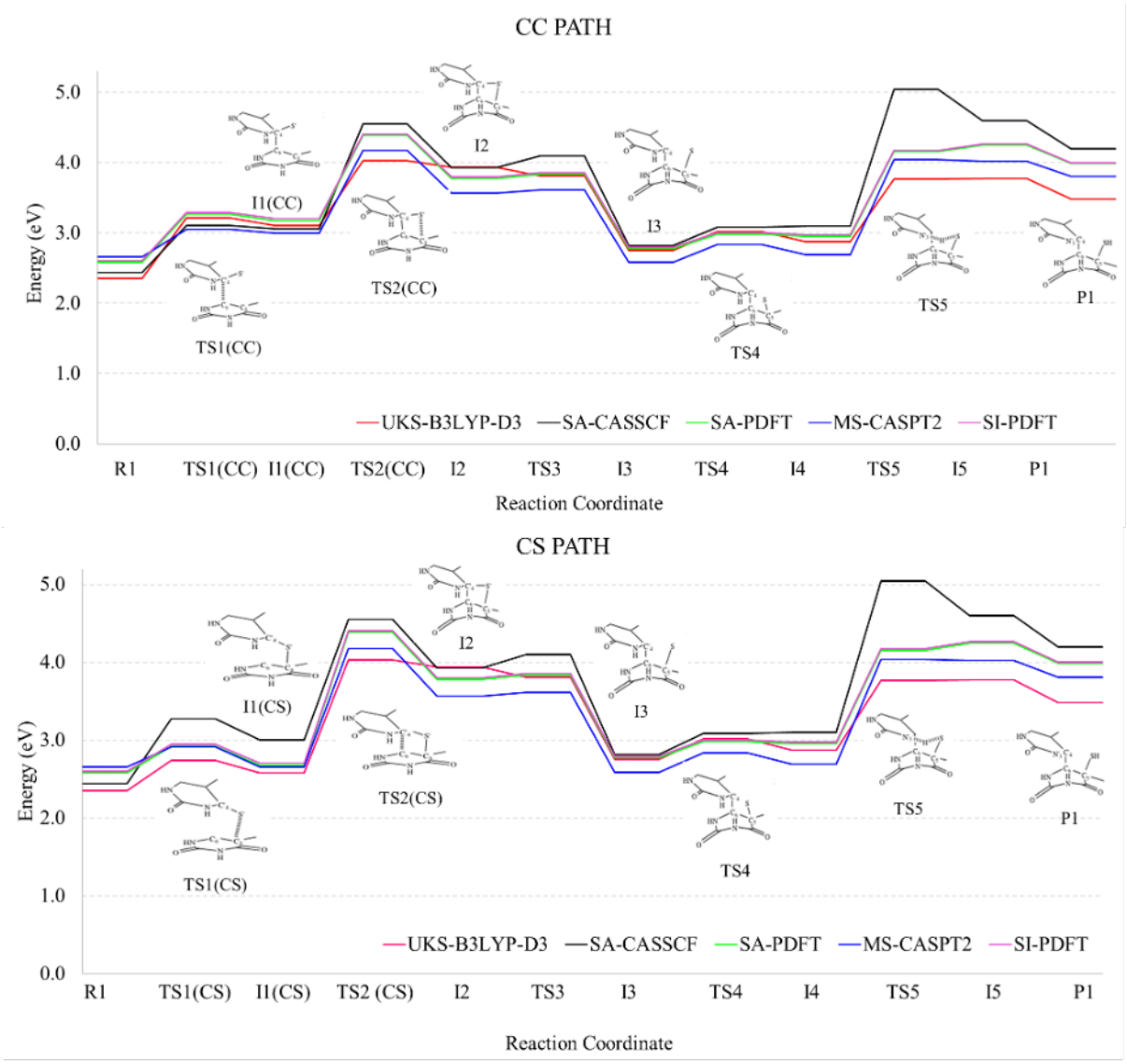

Figure 6.10: Potential energy profile for 6-4PP formation for the CC-CS triplet mechanism and for the CS-CC triplet mechanism calculated with UKS-B3LYP-D3: red line; SA-CASSCF: black line; MS-CASPT2: blue line; SA-PDFT: green line and SI-PDFT: pink line. The cc-pVDZ basis set was used throughout. The energies are in eV relative to the reactants SR1 in the S_0 state. All geometries in this profile were optimized at the UKS-B3LYP-D3 level.

The SA-CASSCF method leads to energetic barriers and minima that are much higher in energy

than those obtained with the other methods. The UKS-B3LYP-D3 profile shows reasonable agreement with the MS-CASPT2 results for most of the steps but has a larger difference for TS5, I5, and P1 product in the last step of the mechanism. The larger error for these structures is likely due to their very high multireference character (M = 0.546–0.551).

The results offered by SA-PDFT and SI-PDFT are in better agreement with MS-CASPT2, though they tend to overestimate the energy along the whole profile. In the triplet reaction profile, there are no significant differences between SA-PDFT and SI-PDFT.

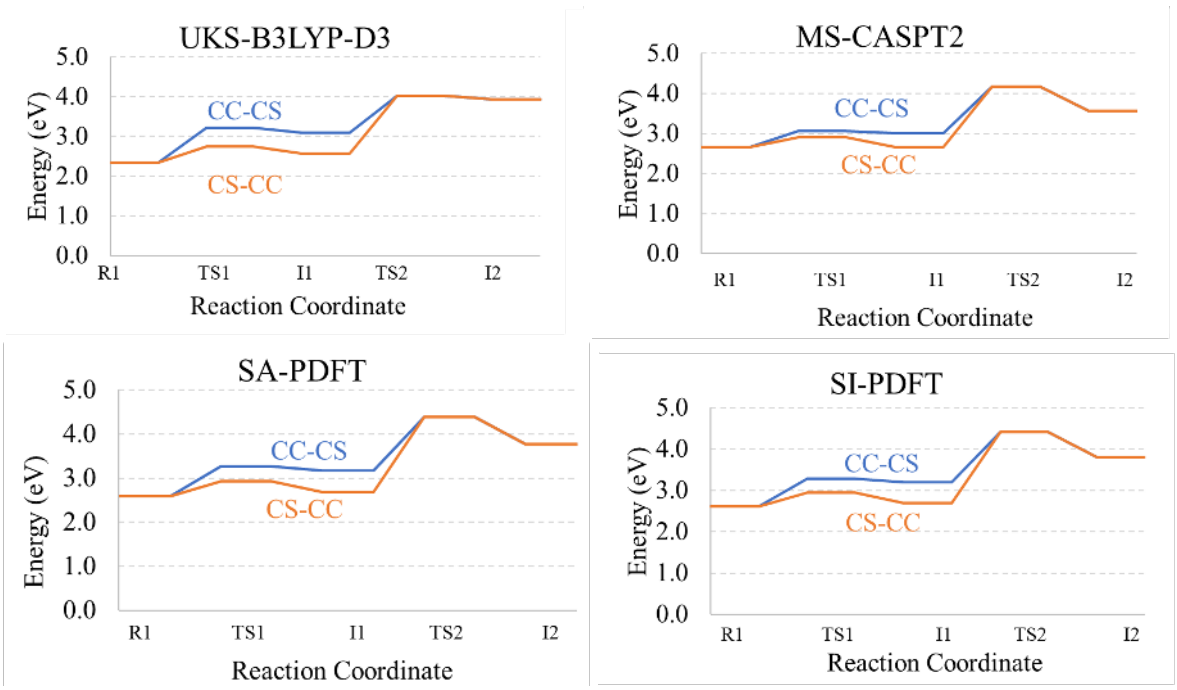

Figure 6.11: T_1 potential energy profiles for the CC-CS (blue lines) and the CS-CC triplet mechanism (orange lines) calculated using UKS-B3LYP-D3, MS-CASPT2, SA-PDFT, and SI-PDFT. The cc-pVDZ basis set was used throughout. Energies are in eV relative to the S_0 energy at its equilibrium geometry (SR1).

Figure 6.11 shows that the triplet potential energy profiles obtained for both mechanisms by using all methods have very high barriers. For all the methods considered, the CS–CC mechanism has

a lower energy requirement. The largest energy difference between CC–CS and CS–CC profiles for the formation of thietane was obtained with UKS-B3LYP-D3. The energy barrier to form the C_5–S bond in the CS–CC triplet mechanism is 2.74 eV by UKS-B3LYP-D3 and 2.53 eV with M06-2X,[181] and the energy needed to form the C6–C'4 bond in the CC–CS triplet mechanism is 3.21 eV with UKS-B3LYP-D3 and 2.91 eV with M06-2X,[181] which indicates that the CS–CC triplet mechanism is more favorable by about 0.5 eV.

However, the MS-CASPT2 results in Figure 6.11 show a much smaller energetic difference between the mechanisms compared to all other methods, with the CC–CS mechanism having a slightly larger barrier than the CS–CC mechanism. The energy barrier to form the C_5–S bond on the CS–CC triplet path is 2.91 eV, and the energy barrier to form the C_6–C'_4 bond on the CC–CS triplet path is 3.05 eV. The difference of 0.1 eV between these triplet mechanisms falls within the range of reliability of the MS-CASPT2 method.

The differences between the SA-PDFT and SI-PDFT profiles (Figure 6.11) are negligible. The SA-PDFT (and SI-PDFT) difference in energy between the CS-CC and CC–CS mechanisms of 0.3 eV is larger than the MS-CASPT2 one and smaller than the UKS-B3LYP-D3 one.

Independent of whether the CC–CS or CS–CC stepwise mechanism is favored, the high-energy barriers that govern the triplet mechanism would preclude the formation of the 6-4PP exclusively along this route. For the CC–CS mechanism, S_0 single-point calculations with B3LYP-D3 and MS-CASPT2 along the T_1 UKS-B3LYP-D3 profile reveal the existence of S_0–T_1 degeneracies (see Figure 6.12). According to MS-CASPT2, the S_0–T_1 degeneracy occurs at the position of the I1CC intermediate where the SOC, computed by using the ANO-RCC-VDZ basis set, amounts to 149 cm–1. This region, which geometrically corresponds to the SI2 intermediate (see Figure 6.4) of the singlet mechanism, would allow for the transfer of the population from the triplet to the singlet manifold, where the reaction would proceed. Once in the ground state, the system would also avoid the high energy barrier of the TS2 transition state (4.0 eV with MS-CASPT2) in the T_1 and evolve to the 6-4PP final product.

With B3LYP-D3, the singlet–triplet crossing is no longer at the minimum and is at the position of the $TS1_{CC}$. In this case, the crossing would lie 0.18 eV above the $I1_{CC}$ which is in line with the energy barrier reported by Zou et al. of 0.24 eV.[181]

For the CS–CC mechanism (see Figure 6.13), B3LYP-D3 predicts similar S_0 and T_1 energies at the position of the I1CS intermediate (Δ = 0.19 eV). This energy gap, however, grows larger at the MS-CASPT2 level (Δ = 0.58 eV).

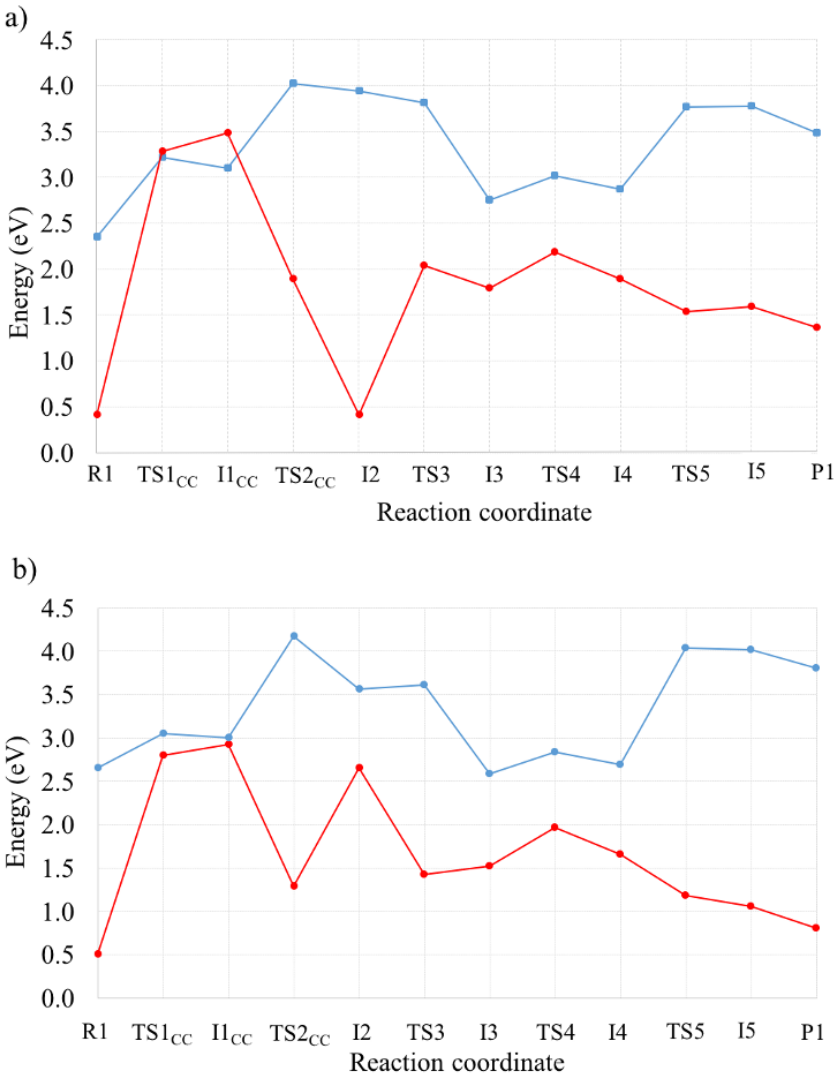

Figure 6.12: Potential energy profile for 6-4PP formation for the CC-CS triplet mechanism and for the CS-CC triplet mechanism calculated with UKS-B3LYP-D3: red line; SA-CASSCF: black line; MS-CASPT2: blue line; SA-PDFT: green line and SI-PDFT: pink line. The cc-pVDZ basis set was used throughout. The energies are in eV relative to the reactants SR1 in the S_0 state. All geometries in this profile were optimized at the UKS-B3LYP-D3 level.

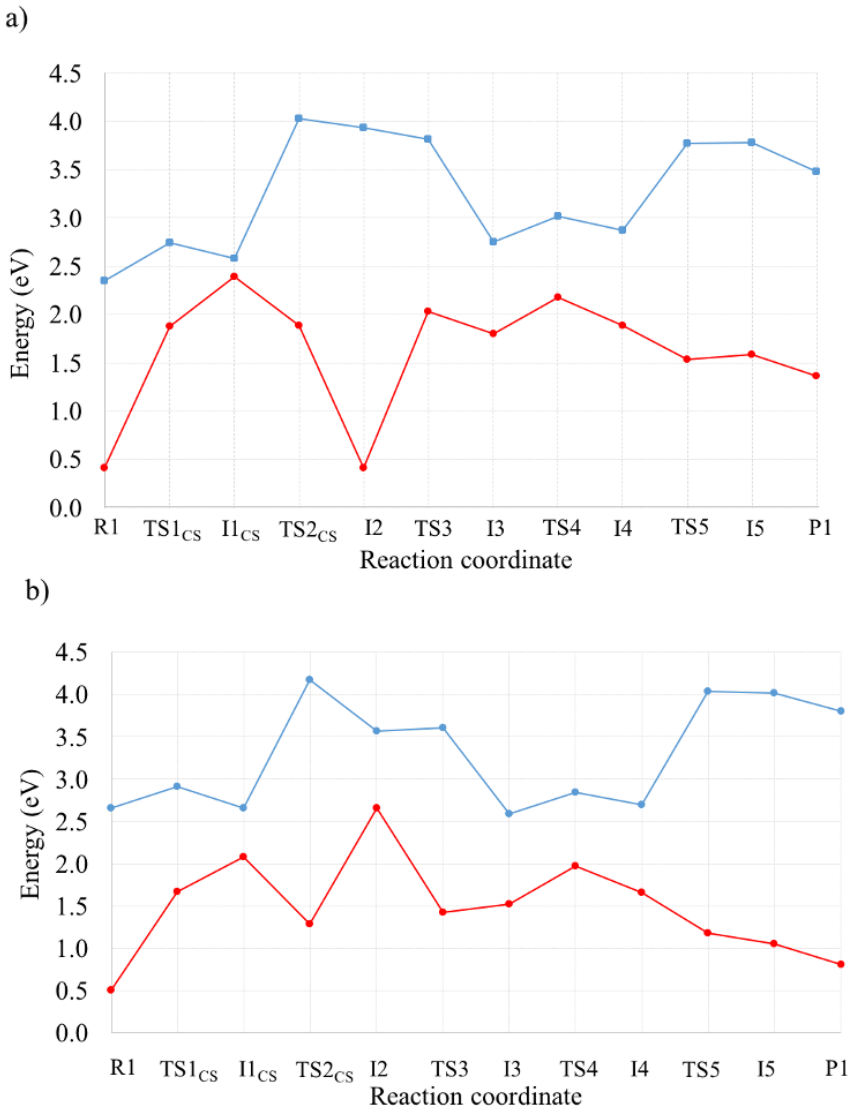

Figure 6.13: Potential energy profile for 6-4PP formation for the CC-CS triplet mechanism and for the CS-CC triplet mechanism calculated with UKS-B3LYP-D3: red line; SA-CASSCF: black line; MS-CASPT2: blue line; SA-PDFT: green line and SI-PDFT: pink line. The cc-pVDZ basis set was used throughout. The energies are in eV relative to the reactants SR1 in the S_0 state. All geometries in this profile were optimized at the UKS-B3LYP-D3 level.

6.4 Concluding Remarks

The thio analogue of the 6-4 pyrimidine–pyrimidone photoproduct, the second most common cross-linking photolesion in natural DNA, is produced when thiated DNA is exposed to UV light. The present work compares several methods for their ability to predict the energetics of the last steps of this process. We studied the mechanism along the ground state and the lowest-lying triplet excited state. The high energy barriers calculated along these profiles suggest a photoinitiated reaction, which would return the population to T_1 and S_0 after internal conversion and/or intersystem crossing processes, as also suggested in previous work.[171]

The calculated S_0 potential energy profile suggests a concerted mechanism for the generation of 6-4PP. Our theoretical assessment reveals that as compared to methods including external correlation, the SA-CASSCF method very significantly overestimates the energetic barriers and the energies of some of the minima. The large differences between the SA-CASSCF results and those obtained by MS-CASPT2 indicate that the incorporation of external electron correlation is necessary to achieve an accurate description of the potential energy profile. We also found some differences between B3LYP-D3 and MS-CASPT2, especially in the region of the strained thietane intermediate. SA-PDFT and SI-PDFT results do not completely agree with the reference MS-CASPT2 results for the description of the ground-state mechanism.

Similar conclusions are drawn for the excited-state potential energy profiles. TD-CAM-B3LYP and TDA-CAM-B3LYP overstabilize the energies of some of the triplet states, while overestimating the energies of higher lying singlets. These large shifts dramatically affect the landscape of the excited-state potential energy profiles and influence the description of the photophysics and photochemistry of these systems. Only small differences, on the other hand, were found between the SA-PDFT and MS-CASPT2 methods, particularly in regions where excited states are strongly coupled. This agreement improves when using the SI-PDFT approach, which properly treats the coupling between states and removes the unphysical crossings on the potential energy surface observed in SA-PDFT.

Two stepwise mechanisms for 6-4PP formation were considered along the lowest triplet state. SA-CASSCF overestimates the barriers and DFT (B3LYP-D3 and M06-2X[181]) underestimates the barriers in the final step of the mechanism when compared to MS-CASPT2. There is excellent agreement in the profiles calculated with the three multireference methods included in our survey. With all methods, we determined the CS–CC triplet mechanism was slightly lower in energy than the CC–CS mechanism.

The energy barriers reported along the singlet and triplet states, although very high, are consistent with the lifetimes reported in the only experimental work available on the system[172] and also with the trapping of the population in certain minima of the PES for some time before the system can evolve to the final stage of the reaction.

The results from this study reinforce that to obtain reliable and accurate results for this strongly correlated photobiochemical reaction, one should employ multireference methods.

Thaïs Scott performed some of the multireference calculations and wrote the manuscript for the Computational Methods and Results and Discussion sections.

Reproduced with permission from 27

CHAPTER 7

CONCLUSIONS

In this work, our goal was to accurately describe the character of excited states produced by photosensitization and to extend the capabilities of MC-PDFT.

The studies involving the photochemistry of Ni-Halide complexes and DNA photolesion formation focused on the importance of excited triplet energy transfer in photosensitization. MC-PDFT was used to settle the divisive debate regarding the photosensitization mechanism of the Ni-halide bond homolysis. The energy transfer mechanism was significantly favored over the single electron transfer mechanism. In the DNA photolesion project, the MC-PDFT results consistently outperformed the single reference methods when compared to experiment. Additionally, the MC-PDFT method was able to accurately describe the excited state and ground state mechanisms of these reactions without increasing the computational cost significantly (compared to CASSCF). MC-PDFT performed particularly well in these systems, and continued development of these methods will lead to even more efficient and accurate studies of excited state systems.

The ideal progression for this project is non-adiabatic molecular dynamics with a full suite of MC-PDFT properties including energies, gradients, non-adiabatic coupling elements, and transition dipole moments.

The research detailed in this dissertation represents significant progress toward this goal. We have derived and implemented the explicit algebraic equations for the analytic first derivatives of the MC-PDFT and CMS-PDFT electronic energies. The development of the analytic gradients, has allowed for more efficient explorations of the MC-PDFT potential energy surface. The framework for these gradients has already been utilized to help develop other first order properties like permanent dipole moments.[194] Implementing the gradients with density fitting was also important to achieving the goal of dynamics with MC-PDFT. Efficient manipulation of the two-electron integrals allows our MC-PDFT calculations to use extensive and accurate basis sets. Current examples of MC-PDFT dynamics are limited to simple cases, such as the recent example of dynamics of

thioformaldehyde that used the SA-MC-PDFT analytic gradients.[195]

Another interesting future project could involve computing the molecular Hessian or the second order derivatives of the energy with respect to the nuclear coordinates. The analytic Hessians of MC-PDFT would be used to predict the force constants and frequencies of molecular systems of interest. Analytic molecular Hessians for more accurate electronic structure methods are scarce due to a large amount of effort required for implementation. Our implementation of the gradient is consistent with the unified modular structure of codes that are already available for other analytic hessians (for example CASSCF). This will allow for the reuse of many sections of already accessible code and will accelerate the development of the Hessians. This work would lead to the study of reaction mechanisms with a full MC-PDFT treatment, which requires the computation of imaginary frequencies to validate transition state structures.

REFERENCES

[1] Scott, T. R., Hermes, M. R., Sand, A. M., Oakley, M. S., Truhlar, D. G., and Gagliardi, L. Analytic gradients for state-averaged multiconfiguration pair-density functional theory. *J. Chem. Phys.*, 153:014106, 2020. doi: 10.1063/5.0007040.

[2] Nakayama, A., Yamazaki, S., and Taketsugu, T. Quantum chemical investigations on the nonradiative deactivation pathways of cytosine derivatives. *J. Phys. Chem. A*, 118(40):9429–9437, 2014. doi: 10.1021/jp506740r.

[3] Schenck, G. O., Hartmann, W., Mannsfeld, S. P., Metzner, W., and Krauch, C. H. Vierringsynthesen durch photosensibilisierte symmetrische und gemischte cyclo-additionen. *Ber. Dtsch. Chem. Ges*, 95(7):1642–1647, 1962.

[4] Hammond, G. S., Turro, N. J., and Fischer, A. Photosensitized cycloaddition reactions. *J. Am. Chem. Soc.*, 83(22):4674–4675, 1961.

[5] Welin, E. R., Le, C., Arias-Rotondo, D. M., McCusker, J. K., and MacMillan, D. W. Photosensitized, energy transfer-mediated organometallic catalysis through electronically excited nickel (II). *Science*, 355(6323):380–385, 2017.

[6] Ortiz-Rodríguez, L. A. and Crespo-Hernández, C. E. Thionated organic compounds as emerging heavy-atom-free photodynamic therapy agents. *Chem. Sci.*, 11:11113–11123, 2020. doi: 10.1039/D0SC04747C.

[7] Arias-Rotondo, D. M. and McCusker, J. K. The photophysics of photoredox catalysis: a roadmap for catalyst design. *Chem. Soc. Rev.*, 45:5803–5820, 2016. doi: 10.1039/C6CS00526H.

[8] Ren, H., Li, G. F., Zhu, B., Lv, X. D., Yao, L. S., Wang, X. L., Su, Z. M., and Guan, W. How does iridium (III) photocatalyst regulate nickel (II) catalyst in metallaphotoredox-catalyzed C–S cross-coupling? theoretical and experimental insights. *ACS Catal.*, 9(5):3858–3865, 2019.

[9] Choi, J. and Fu, G. C. Transition metal–catalyzed alkyl-alkyl bond formation: Another dimension in cross-coupling chemistry. *Science*, 356(6334):eaaf7230, 2017.

[10] Douki, T., Reynaud-Angelin, A., Cadet, J., and Sage, E. Bipyrimidine photoproducts rather than oxidative lesions are the main type of dna damage involved in the genotoxic effect of solar uva radiation. *Biochemistry*, 42(30):9221–9226, 2003. doi: 10.1021/bi034593c. PMID: 12885257.

[11] Crespo-Hernández, C. E., Cohen, B., Hare, P. M., and Kohler, B. Ultrafast excited-state dynamics in nucleic acids. *Chem. Rev.*, 104(4):1977–2020, 2004. doi: 10.1021/cr0206770. PMID: 15080719.

[12] Ullrich, S., Borin, A. C., and Barbatti, M. *Topics in Current Chemistry-Photoinduced Phenomena in Nucleic Acids II*. Springer: Berlin-Heidelberg, 2015.

[13] Gustavsson, T., Improta, R., and Markovitsi, D. Dna/rna: building blocks of life under uv irradiation. *J. Phys. Chem. Lett.*, 1(13):2025–2030, 2010.

[14] Pollum, M., Martínez-Fernández, L., and Crespo-Hernández, C. E. *Photochemistry of Nucleic Acid Bases and Their Thio- and Aza-Analogues in Solution*, pages 245–327. Springer International Publishing, Cham, 2015. ISBN 978-3-319-13371-3. doi: 10.1007/128_2014_554.

[15] Epe, B. DNA damage spectra induced by photosensitization. *Photochemical & Photobiological Sciences*, 1(11):98–106, 2002.

[16] Serrano-Andrés, L. and Merchán, M. Quantum chemistry of the excited state: 2005 overview. *J. Mol. Struct.(Theochem)*, 729(1):99–108, 2005. ISSN 0166-1280. doi: https://doi.org/10.1016/j.theochem.2005.03.020. Proceedings of the 30th International Congress of Theoretical Chemists of Latin Expression.

[17] Li Manni, G., Carlson, R. K., Luo, S., Ma, D., Olsen, J., Truhlar, D. G., and Gagliardi, L. Multiconfiguration pair-density functional theory. *J. Chem. Theory Comput.*, 10(9):3669–3680, 2014. doi: 10.1021/ct500483t.

[18] Gagliardi, L., Truhlar, D. G., Li Manni, G., Carlson, R. K., Hoyer, C. E., and Bao, J. L. Multiconfiguration pair-density functional theory: A new way to treat strongly correlated systems. *Acc. Chem. Res.*, 50(1):66–73, 2016. doi: 10.1021/acs.accounts.6b00471.

[19] Stoneburner, S. J., Truhlar, D. G., and Gagliardi, L. MC-PDFT can calculate singlet–triplet splittings of organic diradicals. *J. Chem. Phys.*, 148(6):064108, 2018. doi: 10.1063/1.5017132.

[20] Sharma, P., Bernales, V., Truhlar, D. G., and Gagliardi, L. Valence $\pi\pi^*$ excitations in benzene studied by multiconfiguration pair-density functional theory. *The Journal of Physical Chemistry Letters*, 10(1):75–81, 2018.

[21] Sand, A. M., Hoyer, C. E., Truhlar, D. G., and Gagliardi, L. State-interaction pair-density functional theory. *J. Chem. Phys.*, 149:24106, 2018. doi: 10.1063/1.5036727.

[22] Scott, T., Nieman, R., Luxon, A., Zhang, B., Lischka, H., Gagliardi, L., and Parish, C. A. A multireference ab initio study of the diradical isomers of pyrazine. *J. Phys. Chem. A*, 123 (10):2049–2057, 2019.

[23] Sand, A. M., Kidder, K. M., Truhlar, D. G., and Gagliardi, L. Calculation of chemical reaction barrier heights by multiconfiguration pair-density functional theory with correlated participating orbitals. *J. Phys. Chem. A*, 123(45):9809–9817, 2019.

[24] Scott, T. R., Oakley, M. S., Hermes, M. R., Sand, A. M., Oakley, M. S., Lindh, R., Truhlar, D. G., and Gagliardi, L. Analytic gradients for multiconfiguration pair-density functional theory with density fitting: Development and application to geometry optimization in the ground and excited states. *J. Chem. Phys.*, 154:074108, 2021. doi: 10.1063/5.0007040.

[25] Bao, M., J Hermes, Scott, T., Sand, A., Lindh, R., Gagliardi, L., and Truhlar, D. Analytic gradients for compressed-state multistate pair-density functional theory. *Mol. Phys.*, 2022.

[26] Maity, B., Scott, T. R., Stroscio, G. D., Gagliardi, L., and Cavallo, L. The role of excited states of LNi $^{II/III}$(aryl)(halide) complexes in ni–halide bond homolysis in the arylation of C_{sp3}–h bonds. *Submitted*, 2022.

[27] Vos, E., Scott, T. R., González-Vázquez, J., Corral, I., Truhlar, D. G., and Gagliardi, L. Intrastrand photolesion formation in thio-substituted DNA: A case study including single-reference and multireference methods. *J. Phys. Chem. A*, 124(50):10422–10433, 2020.

[28] Schrodinger, E. Quantisierung als eigenwertproblem,(dritte mitteilung: Storungstheorie, mit anwendung auf den strakeffekt der balmerlinien. *Ann. Phys.*, (4):474, 1926.

[29] Born, M. and Oppenheimer, J. 1. zur quantentheorie der molekeln. *Ann. Phys.*, 389(20): 457–484, 1927.

[30] Truhlar, D. The reaction path in chemistry: current approaches and perspectives. *Kluwer, Dordrecht*, 229, 1995.

[31] Schlegel, H. B. Exploring potential energy surfaces for chemical reactions: an overview of some practical methods. *J. Comp. Chem.*, 24(12):1514–1527, 2003.

[32] Hellmann, H. *Einführung in die Quantenchemie*. Franz Deuticke, 1937.

[33] Feynman, R. Forces in molecules. *Phys. Rev*, 56:340–343, 1939. doi: 10.1103/PhysRev.56.340.

[34] Handy, N. C. and Schaefer III, H. F. On the evaluation of analytic energy derivatives for correlated wave functions. *J. Chem. Phys.*, 81(11):5031–5033, 1984.

[35] Helgaker, T. and Jørgensen, P. Configuration-interaction energy derivatives in a fully variational formulation. *Theor. Chim. Acta.*, 1989.

[36] Rice, J. and Amos, R. On the efficient evaluation of analytic energy gradients. *Chem. Phys. Lett.*, 122(6):585–590, 1985.

[37] Khait, Y. G., Theis, D., and Hoffmann, M. R. Lagrangian approach for geometrical derivatives and nonadiabatic coupling terms in mrcisd. *Mol. Phys.*, 108(19-20):2703–2716, 2010.

[38] Kohn, W. and Sham, L. J. Self-consistent equations including exchange and correlation effects. *Phys. Rev.*, 140:A1133–A1138, Nov 1965. doi: 10.1103/PhysRev.140.A1133.

[39] Kohn, W., Becke, A. D., and Parr, R. G. Density functional theory of electronic structure. *J. Phys. Chemm.*, 100(31):12974–12980, 1996.

[40] Schuch, N. and Verstraete, F. Computational complexity of interacting electrons and fundamental limitations of density functional theory. *Nat. Phys.*, 5(10):732–735, 2009.

[41] Goerigk, L. and Mehta, N. A trip to the density functional theory zoo: warnings and recommendations for the user. *Aust. J. Chem.*, 72(8):563–573, 2019.

[42] Ghosh, S., Verma, P., Cramer, C. J., Gagliardi, L., and Truhlar, D. G. Combining wave function methods with density functional theory for excited states. *Chem. Rev.*, 118(15): 7249–7292, 2018. doi: 10.1021/acs.chemrev.8b00193.

[43] Perdew, J. P., Savin, A., and Burke, K. Escaping the symmetry dilemma through a pair-density interpretation of spin-density functional theory. *Phys. Rev. A*, 51(6):4531, 1995. doi: 10.1103/PhysRevA.51.4531.

[44] Kaplan, I. Problems in DFT with the total spin and degenerate states. *Int. J. Quantum Chem.*, 107(14):2595–2603, 2007. doi: 10.1002/qua.21423.

[45] Carlson, R. K., Truhlar, D. G., and Gagliardi, L. Multiconfiguration pair-density functional theory: A fully translated gradient approximation and its performance for transition metal dimers and the spectroscopy of $Re_2Cl_8^{2-}$. *J. Chem. Theory Comput.*, 11(9):4077–4085, 2015. doi: 10.1021/acs.jctc.5b00609.

[46] Pulay, P. Analytical derivatives, forces, force constants, molecular geometries, and related response properties in electronic structure theory. *Wiley Interdiscip. Rev. Comput. Mol. Sci.*, 4(3):169–181, 2014. doi: 10.1002/wcms.1171.

[47] Sand, A. M., Hoyer, C. E., Sharkas, K., Kidder, K. M., Lindh, R., Truhlar, D. G., and Gagliardi, L. Analytic Gradients for Complete Active Space Pair-Density Functional Theory. *J. Chem. Theory Comput.*, 14:126–138, 2018. doi: 10.1021/acs.jctc.7b00967.

[48] Aquilante, F., Autschbach, J., Baiardi, A., Battaglia, S., Borin, V. A., Chibotaru, L. F., Conti, I., De Vico, L., Delcey, M., Galván, I. F., Ferré, N., Freitag, L., Garavelli, M., Gong, X., Knecht, S., Larsson, E. D., Lindh, R., Lundberg, M., Malmqvist, P. Å., Nenov, A., Norell, J., Odelius, M., Olivucci, M., Pedersen, T. B., Pedraza-González, L., Phung, Q. M., Pierloot, K., Reiher, M., Schapiro, I., Segarra-Martí, J., Segatta, F., Seijo, L., Sen, S., Sergentu, D. C., Stein, C. J., Ungur, L., Vacher, M., Valentini, A., and Veryazov, V. Modern quantum chemistry with [Open]Molcas. *J. Chem. Phys.*, 152(21):214117, 2020. ISSN 10897690. doi: 10.1063/5.0004835.

[49] Hermes, M. R. https://github.com/MatthewRHermes/mrh, 2018.

[50] Sun, Q., Berkelbach, T. C., Blunt, N. S., Booth, G. H., Guo, S., Li, Z., Liu, J., McClain, J. D., Sayfutyarova, E. R., Sharma, S., Wouters, S., and Chan, G. K. L. PySCF: the python-based simulations of chemistry framework. *Wiley Interdiscip. Rev. Comput. Mol. Sci*, 8(1): e1340, 2018. doi: 10.1002/wcms.1340.

[51] Press, W. H., Teukolsky, S. A., Vetterling, W. T., and Flannery, B. P. *Numerical Recipes in Fortran 77: The Art of Scientific Computing*. Cambridge University Press, Cambridge, U.K., 2nd edition, 1992.

[52] Bao, J. L., Sand, A., Gagliardi, L., and Truhlar, D. G. Correlated-participating-orbitals pair-density functional method and application to multiplet energy splittings of main-group divalent radicals. *J. Chem. Theory Comput.*, 12(9):4274–4283, 2016. doi: 10.1021/acs.jctc.6b00569.

[53] Sharkas, K., Gagliardi, L., and Truhlar, D. G. Multiconfiguration pair-density functional theory and complete active space second order perturbation theory. bond dissociation energies of FeC, NiC, FeS, NiS, FeSe, and NiSe. *J. Phys. Chem. A*, 121(48):9392–9400, 2017. doi: 10.1021/acs.jpca.7b09779.

[54] Sand, A. M., Truhlar, D. G., and Gagliardi, L. Efficient algorithm for multiconfiguration pair-density functional theory with application to the heterolytic dissociation energy of ferrocene. *J. Chem. Phys.*, 146(3):034101, 2017. doi: 10.1063/1.4973709.

[55] Oakley, M. S., Bao, J. J., Klobukowski, M., Truhlar, D. G., and Gagliardi, L. Multireference methods for calculating the dissociation enthalpy of tetrahedral P4 to two P2. *J. Phys. Chem. A*, 122(26):5742–5749, 2018. doi: 10.1021/acs.jpca.7b12366.

[56] Presti, D., Truhlar, D. G., and Gagliardi, L. Intramolecular charge transfer and local excitation in organic fluorescent photoredox catalysts explained by RASCI-PDFT. *J. Phys. Chem. C*, 122(22):12061–12070, 2018. doi: 10.1021/acs.jpcc.8b01844.

[57] Wang, L. P. and Song, C. Geometry optimization made simple with translation and rotation coordinates. *J. Chem. Phys.*, 144:214108, 2016. doi: 10.1063/1.4952956.

[58] Stwalley, W. and Zemke, W. Spectroscopy and structure of the lithium hydride diatomic molecules and ions. *J. Phys. Chem. Ref. Data*, 22(1):87–112, 1993. doi: 10.1063/1.555936.

[59] Adelman, S. and Herschbach, D. Asymptotic approximation for ionic-covalent configuration mixing in hydrogen and alkali hydrides. *Mol. Phys.*, 33(6):793–809, 1977. doi: 10.1080/00268977700100731.

[60] Hoyer, C., Xu, X., Ma, D., Gagliardi, L., and Truhlar, D. Diabatization based on the dipole and quadrupole: The DQ method. *J. Chem. Phys.*, 141:114104, 2014. doi: 10.1063/1.4894472.

[61] Budzák, Š., Scalmani, G., and Jacquemin, D. Accurate excited-state geometries: A CASPT2 and coupled-cluster reference database for small molecules. *J. Chem. Theory Comput.*, 13 (12):6237–6252, 2017. doi: 10.1021/acs.jctc.7b00921.

[62] Jacquemin, D. What is the key for accurate absorption and emission calculations, energy or geometry? *J. Chem. Theory Comput.*, 14(3):1534–1543, 2018. doi: 10.1021/acs.jctc.7b01224.

[63] Job, V., Sethuraman, V., and Innes, K. The 3500 Å $^1A_2$-$\tilde{X}^1A_1$ transition of formaldehyde-H_2, D_2, and HD: Vibrational and rotational analyses. *J. Mol. Spectrosc.*, 30(1-3):365–426, 1969. doi: 10.1016/0022-2852(69)90274-4.

[64] Jensen, P. and Bunker, P. The geometry and the inversion potential function of formaldehyde in the $\tilde{A}^1A_2$ and $\tilde{a}^3A_2$ electronic states. *J. Mol. Spectrosc.*, 94(1):114–125, 1982. doi: 10.1016/0022-2852(82)90298-3.

[65] Clouthier, D. and Ramsay, D. The spectroscopy of formaldehyde and thioformaldehyde. *Annu. Rev. Phys. Chem.*, 34(1):31–58, 1983. doi: 10.1146/annurev.pc.34.100183.000335.

[66] Godunov, I., Abramenkov, A., Bataev, V., and Pupyshev, V. Potential functions of inversion of R 2 CO (R= H, F, Cl) molecules in the lowest excited electronic states. *Russ. Chem. Bull.*, 48(4):640–646, 1999. doi: 10.1007/BF02496238.

[67] Jones, V. and Coon, J. Rotational constants and geometrical structure of the $^1A_2$ and $^3A_2$ states of H_2CO and D_2CO. *J. Mol. Spectrosc.*, 31(1-13):137–154, 1969. doi: 10.1016/0022-2852(69)90347-6.

[68] Walzl, K., Koerting, C., and Kuppermann, A. Electron-impact spectroscopy of acetaldehyde. *J. Chem. Phys.*, 87(7):3796–3803, 1987. doi: 10.1063/1.452935.

[69] Loos, P. F., Scemama, A., Blondel, A., Garniron, Y., Caffarel, M., and Jacquemin, D. A mountaineering strategy to excited states: Highly accurate reference energies and benchmarks. *J. Chem. Theory Comput.*, 14(8):4360–4379, 2018.

[70] Watson, M. A. and Chan, G. K. L. Excited states of butadiene to chemical accuracy: Reconciling theory and experiment. *J. Chem. Theory Comput.*, 8(11):4013–4018, 2012. doi: 10.1021/ct300591z.

[71] Shu, Y. and Truhlar, D. G. Doubly excited character or static correlation of the reference state in the controversial 2^1A_g state of trans-butadiene? *J. Am. Chem. Soc.*, 139(39):13770–13778, 2017. doi: 10.1021/jacs.7b06283.

[72] Haugen, W. and M, T. Molecular structures of 1, 3-butadiene and 1, 3, 5-trans-hexatriene. *Acta. Chem. Scand.*, 20(6):1726, 1966. doi: 10.3891/acta.chem.scand.20-1726.

[73] Fogarasi, G. Relative stabilities of three low-energy tautomers of cytosine: a coupled cluster electron correlation study. *J. Phys. Chem. A*, 106(7):1381–1390, 2002. doi: 10.1021/jp013067x.

[74] Merchan, M., Gonzalez-Luque, R., Climent, T., Serrano-Andres, L., Rodríguez, E., Reguero, M., and Pelaez, D. Unified model for the ultrafast decay of pyrimidine nucleobases. *J. Phys. Chem. B*, 110(51):26471–26476, 2006. doi: 10.1021/jp066874a.

[75] González-Vázquez, J. and González, L. A time-dependent picture of the ultrafast deactivation of keto-cytosine including three-state conical intersections. *Chem. Phys. Chem.*, 11 (17):3617–3624, 2010. doi: 10.1002/cphc.201000557.

[76] Nakayama, A., Harabuchi, Y., Yamazaki, S., and Taketsugu, T. Photophysics of cytosine tautomers: new insights into the nonradiative decay mechanisms from MS-CASPT2 potential energy calculations and excited-state molecular dynamics simulations. *Phys. Chem. Chem. Phys.*, 15(29):12322–12339, 2013. doi: 10.1039/c3cp51617b.

[77] Barker, D. and Marsh, R. The crystal structure of cytosine. *Acta Crystallogr. A*, 17(12): 1581–1587, 1964. doi: 10.1107/S0365110X64003899.

[78] Delcey, M. G., Pedersen, T. B., Aquilante, F., and Lindh, R. Analytical gradients of the state-average complete active space self-consistent field method with density fitting. *J. Chem. Phys.*, 143:044110, 2015. doi: 10.1063/1.4927228.

[79] Galván, I. F., Delcey, M. G., Pedersen, T. B., Aquilante, F., and Lindh, R. Analytical state-average complete-active-space self-consistent field nonadiabatic coupling vectors: Implementation with density-fitted two-electron integrals and application to conical intersections. *J. Chem. Theory Comput.*, 12(8):3636–3653, 2016.

[80] Schütz, M., Werner, H. J., Lindh, R., and Manby, F. R. Analytical energy gradients for local second-order møller–plesset perturbation theory using density fitting approximations. *J. Chem. Phys.*, 121(2):737–750, 2004.

[81] Schrader, D. M. and Prager, S. Use of electrostatic variation principles in molecular energy calculations. *J. Chem. Phys.*, 37(7):1456–1460, 1962.

[82] Baerends, E., Ellis, D., and Ros, P. Self-consistent molecular hartree—fock—slater calculations i. the computational procedure. *Chem. Phys.*, 2(1):41–51, 1973.

[83] Whitten, J. L. Coulombic potential energy integrals and approximations. *J. Chem. Phys.*, 58(10):4496–4501, 1973.

[84] Dunlap, B. I., Connolly, J. W., and Sabin, J. R. On the applicability of LCAO-Xα methods to molecules containing transition metal atoms: The nickel atom and nickel hydride. *Int. J. Quantum Chem.*, 12(S11):81–87, 1977.

[85] Dunlap, B., Connolly, J., and Sabin, J. On first-row diatomic molecules and local density models. *J. Chem. Phys.*, 71(12):4993–4999, 1979.

[86] Aquilante, F., Gagliardi, L., Pedersen, T. B., and Lindh, R. Atomic cholesky decompositions: A route to unbiased auxiliary basis sets for density fitting approximation with tunable accuracy and efficiency. *J. Chem. Phys.*, 130(15):154107, 2009.

[87] Manni, G. L., Carlson, R. K., Luo, S., Ma, D., Olsen, J., Truhlar, D. G., and Gagliardi, L. Multiconfiguration Pair-Density Functional Theory. *J. Chem. Theory Comput.*, 10:3669, 2014. doi: 10.1021/ct500483t.

[88] Andersson, K., Malmqvist, P. Å., and Roos, B. O. Second-order perturbation theory with a complete active space self-consistent field reference function. *J. Chem. Phys.*, 96(2):1218–1226, 1992.

[89] Andersson, K., Malmqvist, P. A., Roos, B. O., Sadlej, A. J., and Wolinski, K. Second-order perturbation theory with a CASSCF reference function. *J. Phys. Chem.*, 94(14):5483–5488, 1990.

[90] Baker, J. Techniques for geometry optimization: A comparison of cartesian and natural internal coordinates. *J. Comp. Chem.*, 14(9):1085–1100, 1993.

[91] Aquilante, F., Delcey, M. G., Pedersen, T. B., Fdez. Galván, I., and Lindh, R. Inner projection techniques for the low-cost handling of two-electron integrals in quantum chemistry. *Mol. Phys.*, 115(17-18):2052–2064, 2017.

[92] Delcey, M. G., Freitag, L., Pedersen, T. B., Aquilante, F., Lindh, R., and González, L. Analytical gradients of complete active space self-consistent field energies using cholesky decomposition: Geometry optimization and spin-state energetics of a ruthenium nitrosyl complex. *J. Chem. Phy.*, 140(17):174103, 2014.

[93] Park, J. W. and Shiozaki, T. Analytical derivative coupling for multistate CASPT2 theory. *J. Chem. Theor. Comput.*, 13(6):2561–2570, 2017.

[94] Park, J. W. and Shiozaki, T. On the accuracy of retinal protonated schiff base models. *Mol. Phys.*, 116(19-20):2583–2590, 2018.

[95] Bao, J. J., Zhou, C., Varga, Z., Kanchanakungwankul, S., Gagliardi, L., and Truhlar, D. G. Multi-state pair-density functional theory. *Faraday Discuss.*, 224:348–372, 2020. ISSN 13645498. doi: 10.1039/d0fd00037j.

[96] Bao, J. J., Zhou, C., and Truhlar, D. G. Compressed-State Multistate Pair-Density Functional Theory. *J. Chem. Theory. Comput.*, 16(12):7444–7452, 2020. ISSN 15499626. doi: 10.1021/acs.jctc.0c00908.

[97] Stålring, J., Bernhardsson, A., and Lindh, R. Analytical gradients of a state average MCSCF state and a state average diagnostic. *Mol. Phys.*, 99(2):103, 2001. ISSN 1362-3028. doi: 10.1080/002689700110005642.

[98] Skubi, K. L., Blum, T. R., and Yoon, T. P. Dual catalysis strategies in photochemical synthesis. *Chem. Rev.*, 116(17):10035–10074, 2016.

[99] Twilton, J., Le, C. C., Zhang, P., Shaw, M. H., Evans, R. W., and MacMillan, D. W. The merger of transition metal and photocatalysis. *Nat. Rev. Chem.*, 1(7):1–19, 2017.

[100] Fabry, D. C. and Rueping, M. Merging visible light photoredox catalysis with metal catalyzed C–H activations: on the role of oxygen and superoxide ions as oxidants. *Acc. Chem. Res.*, 49(9):1969–1979, 2016.

[101] Prier, C. K., Rankic, D. A., and MacMillan, D. W. Visible light photoredox catalysis with transition metal complexes: applications in organic synthesis. *Chem. Rev.*, 113(7):5322–5363, 2013.

[102] Tellis, J. C., Kelly, C. B., Primer, D. N., Jouffroy, M., Patel, N. R., and Molander, G. A. Single-electron transmetalation via photoredox/nickel dual catalysis: unlocking a new paradigm for sp^3–sp^2 cross-coupling. *Acc. Chem. Res.*, 49(7):1429–1439, 2016.

[103] Zheng, S., Hu, Y., and Yuan, W. Recent advances in C (sp^3)–C (sp^3) cross-coupling via metallaphotoredox strategies. *Synthesis*, 53(10):1719–1733, 2021.

[104] Milligan, J. A., Phelan, J. P., Badir, S. O., and Molander, G. A. Alkyl carbon–carbon bond formation by nickel/photoredox cross-coupling. *Angew. Chem., Int. Ed.*, 58(19):6152–6163, 2019.

[105] Zuo, Z., Ahneman, D. T., Chu, L., Terrett, J. A., Doyle, A. G., and MacMillan, D. W. Merging photoredox with nickel catalysis: Coupling of α-carboxyl sp^3-carbons with aryl halides. *Science*, 345(6195):437–440, 2014.

[106] Chan, A. Y., Perry, I. B., Bissonnette, N. B., Buksh, B. F., Edwards, G. A., Frye, L. I., Garry, O. L., Lavagnino, M. N., Li, B. X., Liang, Y., et al. Metallaphotoredox: the merger of photoredox and transition metal catalysis. *Chem. Rev.*, 122(2):1485–1542, 2021.

[107] Zuo, Z., Cong, H., Li, W., Choi, J., Fu, G. C., and MacMillan, D. W. Enantioselective decarboxylative arylation of α-amino acids via the merger of photoredox and nickel catalysis. *J. Am. Chem. Soc.*, 138(6):1832–1835, 2016.

[108] Johnston, C. P., Smith, R. T., Allmendinger, S., and MacMillan, D. W. Metallaphotoredox-catalysed sp^3–sp^3 cross-coupling of carboxylic acids with alkyl halides. *Nature*, 536(7616): 322–325, 2016.

[109] Gutierrez, O., Tellis, J. C., Primer, D. N., Molander, G. A., and Kozlowski, M. C. Nickel-catalyzed cross-coupling of photoredox-generated radicals: uncovering a general manifold for stereoconvergence in nickel-catalyzed cross-couplings. *J. Am. Chem. Soc.*, 137(15): 4896–4899, 2015.

[110] El Khatib, M., Serafim, R. A. M., and Molander, G. A. α-arylation/heteroarylation of chiral α-aminomethyltrifluoroborates by synergistic iridium photoredox/nickel cross-coupling catalysis. *Angew. Chem., Int. Ed.*, 128(1):262–266, 2016.

[111] Buzzetti, L., Crisenza, G. E., and Melchiorre, P. Mechanistic studies in photocatalysis. *Angew. Chem., Int. Ed.*, 58(12):3730–3747, 2019.

[112] Nakajima, K., Nojima, S., and Nishibayashi, Y. Nickel-and photoredox-catalyzed cross-coupling reactions of aryl halides with 4-alkyl-1, 4-dihydropyridines as formal nucleophilic alkylation reagents. *Angew. Chem., Int. Ed.*, 128(45):14312–14316, 2016.

[113] Jouffroy, M., Primer, D. N., and Molander, G. A. Base-free photoredox/nickel dual-catalytic cross-coupling of ammonium alkylsilicates. *J. Am. Chem. Soc.*, 138(2):475–478, 2016.

[114] Zhang, P., Le, C., and MacMillan, D. W. Silyl radical activation of alkyl halides in metallaphotoredox catalysis: a unique pathway for cross-electrophile coupling. *J. Am. Chem. Soc.*, 138(26):8084–8087, 2016.

[115] Holmberg-Douglas, N. and Nicewicz, D. A. Photoredox-catalyzed C–H functionalization reactions. *Chem. Rev.*, 122(2):1925–2016, 2021.

[116] Mantry, L., Maayuri, R., Kumar, V., and Gandeepan, P. Photoredox catalysis in nickel-catalyzed C–H functionalization. *Beilstein J. Org. Chem.*, 17(1):2209–2259, 2021.

[117] Capaldo, L., Ravelli, D., and Fagnoni, M. Direct photocatalyzed hydrogen atom transfer (hat) for aliphatic C–H bonds elaboration. *Chem, Rev.*, 122(2):1875–1924, 2021.

[118] Kariofillis, S. K. and Doyle, A. G. Synthetic and mechanistic implications of chlorine photoelimination in nickel/photoredox C (sp^3)–H cross-coupling. *Acc. Chem. Res.*, 54(4): 988–1000, 2021.

[119] Shaw, M. H., Shurtleff, V. W., Terrett, J. A., Cuthbertson, J. D., and MacMillan, D. W. Native functionality in triple catalytic cross-coupling: sp^3 C–H bonds as latent nucleophiles. *Science*, 352(6291):1304–1308, 2016.

[120] Le, C., Liang, Y., Evans, R. W., Li, X., and MacMillan, D. W. Selective sp^3 C–H alkylation via polarity-match-based cross-coupling. *Nature*, 547(7661):79–83, 2017.

[121] Huang, H. M., Bellotti, P., Chen, P. P., Houk, K. N., and Glorius, F. Allylic C (sp^3)–H arylation of olefins via ternary catalysis. *Nat. Synth.*, 1(1):59–68, 2022.

[122] Huang, L. and Rueping, M. Direct cross-coupling of allylic C(sp^3)- H bonds with aryl-and vinylbromides by combined nickel and visible-light catalysis. *Angew. Chem., Int. Ed.*, 130 (32):10490–10494, 2018.

[123] Shen, Y., Gu, Y., and Martin, R. sp^3 C–H arylation and alkylation enabled by the synergy of triplet excited ketones and nickel catalysts. *J. Am. Chem. Soc.*, 140(38):12200–12209, 2018.

[124] Dewanji, A., Krach, P. E., and Rueping, M. The dual role of benzophenone in visible-light/nickel photoredox-catalyzed C–H arylations: Hydrogen-atom transfer and energy transfer. *Angew. Chem., Int. Ed.*, 58(11):3566–3570, 2019.

[125] Ahneman, D. T. and Doyle, A. G. C–H functionalization of amines with aryl halides by nickel-photoredox catalysis. *Chem. Sci.*, 7(12):7002–7006, 2016.

[126] Nielsen, M. K., Shields, B. J., Liu, J., Williams, M. J., Zacuto, M. J., and Doyle, A. G. Mild, redox-neutral formylation of aryl chlorides through the photocatalytic generation of chlorine radicals. *Angew. Chem., Int. Ed.*, 56(25):7191–7194, 2017.

[127] Shields, B. J. and Doyle, A. G. Direct C(sp^3)–H cross coupling enabled by catalytic generation of chlorine radicals. *J. Am. Chem. Soc.*, 138(39):12719–12722, 2016.

[128] Heitz, D. R., Tellis, J. C., and Molander, G. A. Photochemical nickel-catalyzed C–H arylation: synthetic scope and mechanistic investigations. *J. Am. Chem. Soc.*, 138(39):12715–12718, 2016.

[129] Santos, M. S., Corrêa, A. G., Paixão, M. W., and König, B. C (sp^3)- C (sp^3) cross-coupling of alkyl bromides and ethers mediated by metal and visible light photoredox catalysis. *Adv. Synth. Catal.*, 362(12):2367–2372, 2020.

[130] Yuan, M. and Gutierrez, O. Mechanisms, challenges, and opportunities of dual ni/photoredox-catalyzed C (sp^2)–C (sp^3) cross-couplings. *Wires Comput. Mol. Sci.*, 12(3): e1573, 2022.

[131] Maity, B., Zhu, C., Yue, H., Huang, L., Harb, M., Minenkov, Y., Rueping, M., and Cavallo, L. Mechanistic insight into the photoredox-nickel-hat triple catalyzed arylation and alkylation of α-amino C_{sp3}–H bonds. *J. Am. Chem. Soc.*, 142(40):16942–16952, 2020.

[132] Maity, B., Zhu, C., Rueping, M., and Cavallo, L. Mechanistic understanding of arylation vs alkylation of aliphatic C_{sp3}–H bonds by decatungstate–nickel catalysis. *ACS Catal.*, 11 (22):13973–13982, 2021.

[133] Ting, S. I., Garakyaraghi, S., Taliaferro, C. M., Shields, B. J., Scholes, G. D., Castellano, F. N., and Doyle, A. G. ^{3}d-d excited states of Ni (II) complexes relevant to photoredox catalysis: spectroscopic identification and mechanistic implications. *J. Am. Chem. Soc.*, 142(12):5800–5810, 2020.

[134] Cagan, D. A., Bím, D., Silva, B., Kazmierczak, N. P., McNicholas, B. J., and Hadt, R. G. Elucidating the mechanism of excited-state bond homolysis in nickel–bipyridine photoredox catalysts. *J. Am. Chem. Soc.*, 144(14):6516–6531, 2022.

[135] Cagan, D. A., Stroscio, G. D., Cusumano, A. Q., and Hadt, R. G. Multireference description of nickel–aryl homolytic bond dissociation processes in photoredox catalysis. *J. Phys. Chem. A*, 124(48):9915–9922, 2020.

[136] Vitillo, J. G., Cramer, C. J., and Gagliardi, L. Multireference methods are realistic and useful tools for modeling catalysis. *Isr. J. Chem.*, 62(1-2):e202100136, 2022.

[137] Frisch, M. J., Trucks, G. W., Schlegel, H. B., Scuseria, G. E., Robb, M. A., Cheeseman, J. R., Scalmani, G., Barone, V., Petersson, G. A., Nakatsuji, H., Li, X., Caricato, M., Marenich, A. V., Bloino, J., Janesko, B. G., Gomperts, R., Mennucci, B., Hratchian, H. P., Ortiz, J. V., Izmaylov, A. F., Sonnenberg, J. L., Williams-Young, D., Ding, F., Lipparini, F., Egidi, F., Goings, J., Peng, B., Petrone, A., Henderson, T., Ranasinghe, D., Zakrzewski, V. G., Gao, J., Rega, N., Zheng, G., Liang, W., Hada, M., Ehara, M., Toyota, K., Fukuda, R., Hasegawa, J., Ishida, M., Nakajima, T., Honda, Y., Kitao, O., Nakai, H., Vreven, T., Throssell, K., Montgomery, J. A., Jr., Peralta, J. E., Ogliaro, F., Bearpark, M. J., Heyd, J. J., Brothers, E. N., Kudin, K. N., Staroverov, V. N., Keith, T. A., Kobayashi, R., Normand, J., Raghavachari, K., Rendell, A. P., Burant, J. C., Iyengar, S. S., Tomasi, J., Cossi, M., Millam, J. M., Klene, M.,

Adamo, C., Cammi, R., Ochterski, J. W., Martin, R. L., Morokuma, K., Farkas, O., Foresman, J. B., and Fox, D. J. Gaussian~16 Revision C.01, 2016. Gaussian Inc. Wallingford CT.

[138] Adamo, C. and Barone, V. Toward reliable density functional methods without adjustable parameters: The PBE0 model. *J. Chem. Phys.*, 110(13):6158–6170, 1999.

[139] Grimme, S., Antony, J., Ehrlich, S., and Krieg, H. A consistent and accurate ab initio parametrization of density functional dispersion correction (DFT-D) for the 94 elements H-Pu. *J. Chem. Phys.*, 132(15):154104, 2010.

[140] Marenich, A. V., Cramer, C. J., and Truhlar, D. G. Universal solvation model based on solute electron density and on a continuum model of the solvent defined by the bulk dielectric constant and atomic surface tensions. *J. Phys. Chem. B*, 113(18):6378–6396, 2009.

[141] Weigend, F. and Ahlrichs, R. Balanced basis sets of split valence, triple zeta valence and quadruple zeta valence quality for h to rn: Design and assessment of accuracy. *Phys. Chem. Chem. Phys.*, 7(18):3297–3305, 2005.

[142] Zhao, Y. and Truhlar, D. G. The M06 suite of density functionals for main group thermochemistry, thermochemical kinetics, noncovalent interactions, excited states, and transition elements: two new functionals and systematic testing of four M06-class functionals and 12 other functionals. *Theor. Chem. Acc.*, 120(1):215–241, 2008.

[143] Marcus, R. A. On the theory of oxidation-reduction reactions involving electron transfer. i. *J. Chem. Phys.*, 24(5):966–978, 1956.

[144] Neese, F., Wennmohs, F., Hansen, A., and Becker, U. Efficient, approximate and parallel hartree–fock and hybrid DFT calculations. a 'chain-of-spheres' algorithm for the hartree–fock exchange. *Chem. Phys.*, 356(1-3):98–109, 2009.

[145] Runge, E. and Gross, E. K. Density-functional theory for time-dependent systems. *Phys. Rev. Lett.*, 52(12):997, 1984.

[146] Casida, M. Recent developments and applications of modern density functional theory. *J. Theor. Comput. Chem.*, 4:391, 1996.

[147] Petersilka, M., Gossmann, U., and Gross, E. Excitation energies from time-dependent density-functional theory. *Phys. Rev. Lett.*, 76(8):1212, 1996.

[148] Hirata, S. and Head-Gordon, M. Time-dependent density functional theory within the tamm–dancoff approximation. *Chem. Phys. Lett.*, 314(3-4):291–299, 1999.

[149] Peach, M. J., Williamson, M. J., and Tozer, D. J. Influence of triplet instabilities in TDDFT. *J. Chem. Theor. Comput.*, 7(11):3578–3585, 2011.

[150] Pandharkar, R., Hermes, M. R., Truhlar, D. G., and Gagliardi, L. A new mixing of nonlocal exchange and nonlocal correlation with multiconfiguration pair-density functional theory. *J. Phys. Chem. Lett.*, 11(23):10158–10163, 2020.

[151] Andersson, K. and Roos, B. O. Excitation energies in the nickel atom studied with the complete active space scf method and second-order perturbation theory. *Chem. Phys. Lett.*, 191(6):507–514, 1992.

[152] Dexter, D. L. A theory of sensitized luminescence in solids. *J. Chem. Phys.*, 21(5):836–850, 1953.

[153] Arslancan, S., Martínez-Fernández, L., and Corral, I. Photophysics and photochemistry of canonical nucleobases' thioanalogs: From quantum mechanical studies to time resolved experiments. *Mol.*, 22(6):998, 2017.

[154] Reelfs, O., Macpherson, P., Ren, X., Xu, Y. Z., Karran, P., and Young, A. R. Identification of potentially cytotoxic lesions induced by UVA photoactivation of DNA 4-thiothymidine in human cells. *Nucleic Acids Res.*, 39(22):9620–9632, 2011.

[155] Reelfs, O., Karran, P., and Young, A. R. 4-thiothymidine sensitization of DNA to UVA offers potential for a novel photochemotherapy. *Photochem. Photobiol. Sci.*, 1(11):148–154, 2002.

[156] Pridgeon, S., Heer, R., Taylor, G., Newell, D., O'toole, K., Robinson, M., Xu, Y., Karran, P., and Boddy, A. Thiothymidine combined with UVA as a potential novel therapy for bladder cancer. *Br. J. Cancer*, 104(12):1869–1876, 2011.

[157] Pollum, M., Lam, M., Jockusch, S., and Crespo-Hernández, C. E. Dithionated nucleobases as effective photodynamic agents against human epidermoid carcinoma cells. *ChemMedChem*, 13(10):1044–1050, 2018.

[158] Pollum, M., Guan, L., Ahsanuddin, S., Baron, E., Lam, M., and Crespo-Hernández, C. 593 photoactivation of sulfur-modified DNA and RNA analogs induces cytotoxicity in epidermoid carcinoma cells. *J. Invest. Dermatol.*, 136(5):S105, 2016.

[159] Conti, I., Martínez-Fernández, L., Esposito, L., Hofinger, S., Nenov, A., Garavelli, M., and Improta, R. Multiple electronic and structural factors control cyclobutane pyrimidine dimer and 6–4 thymine–thymine photodimerization in a DNA duplex. *Chem. Eur. J.*, 23(60): 15177–15188, 2017.

[160] Serrano-Andres, L. and Merchan, M. Are the five natural DNA/RNA base monomers a good choice from natural selection?: A photochemical perspective. *J. Photochem. Photobiol. C*, 10(1):21–32, 2009.

[161] Gonzalez-Luque, R., Climent, T., Gonzalez-Ramirez, I., Merchan, M., and Serrano-Andres, L. Singlet- triplet states interaction regions in DNA/RNA nucleobase hypersurfaces. *J. Chem. Theory Comput.*, 6(7):2103–2114, 2010.

[162] Nikogosyan, D., Angelov, D., and Oraevsky, A. Determination of parameters of excited states of DNA and RNA bases by laser UV photolysis. *Photochem. Photobiol.*, 35(5):627–635, 1982.

[163] Salet, C. and Bensasson, R. Studies on thymine and uracil triplet excited state in acetonitrile and water. *Photochem. Photobiol.*, 22(6):231–235, 1975.

[164] Salet, C., Bensasson, R., and Becker, R. Triplet excited states of pyrimidine nucleosides and nucleotides. *Photochem. Photobiol.*, 30(3):325–329, 1979.

[165] Lamola, A. A. and Mittal, J. P. Solution photochemistry of thymine and uracil. *Science*, 154 (3756):1560–1561, 1966.

[166] Mai, S., Pollum, M., Martínez-Fernández, L., Dunn, N., Marquetand, P., Corral, I., Crespo-Hernández, C. E., and González, L. The origin of efficient triplet state population in sulfur-substituted nucleobases. *Nat. Commun.*, 7(1):1–8, 2016.

[167] Pollum, M., Jockusch, S., and Crespo-Hernandez, C. E. 2, 4-dithiothymine as a potent UVA chemotherapeutic agent. *J. Am. Chem. Soc.*, 136(52):17930–17933, 2014.

[168] Harada, Y., Suzuki, T., Ichimura, T., and Xu, Y. Z. Triplet formation of 4-thiothymidine and its photosensitization to oxygen studied by time-resolved thermal lensing technique. *J. Phys. Chem. B*, 111(19):5518–5524, 2007.

[169] Kuramochi, H., Kobayashi, T., Suzuki, T., and Ichimura, T. Excited-state dynamics of 6-aza-2-thiothymine and 2-thiothymine: Highly efficient intersystem crossing and singlet oxygen photosensitization. *J. Phys. Chem. B*, 114(26):8782–8789, 2010.

[170] Matus, S. K. A., Fourrey, J. L., and Clivio, P. Synthesis of the TT pyrimidine (6–4) pyrimidone photoproduct–thio analogue phosphoramidite building block. *Org. Biomol. Chem.*, 1 (19):3316–3320, 2003.

[171] Xie, B. B. and Cui, C. X. Theoretical studies on photo-induced cycloaddition and (6-4) reactions of the thymidine: 4-thiothymidine dimer in a DNA duplex. *Phys. Chem. Chem. Phys.*, 21(4):2006–2016, 2019.

[172] Ortiz-Rodríguez, L. A., Reichardt, C., Hoehn, S. J., Jockusch, S., and Crespo-Hernández, C. E. Detection of the thietane precursor in the UVA formation of the DNA 6-4 photoadduct. *Nat. Commun.*, 11(1):1–9, 2020.

[173] bo Yang, Z., bo Zhang, R., and Eriksson, L. A. A triplet mechanism for the formation of thymine–thymine (6-4) dimers in uv-irradiated DNA. *Phys. Chem. Chem. Phys.*, 13(19): 8961–8966, 2011.

[174] Giussani, A., Serrano-Andres, L., Merchan, M., Roca-Sanjuan, D., and Garavelli, M. Photoinduced formation mechanism of the thymine–thymine (6–4) adduct. *J. Phys. Chem. B*, 117(7):1999–2004, 2013.

[175] Marguet, S. and Markovitsi, D. Time-resolved study of thymine dimer formation. *J. Am. Chem. Soc.*, 127(16):5780–5781, 2005.

[176] Palmer, I. J., Ragazos, I. N., Bernardi, F., Olivucci, M., and Robb, M. A. An MC-SCF study of the (photochemical) paterno-buchi reaction. *J. Am. Chem. Soc.*, 116(5):2121–2132, 1994.

[177] Lischka, H., Nachtigallova, D., Aquino, A. J., Szalay, P. G., Plasser, F., Machado, F. B., and Barbatti, M. Multireference approaches for excited states of molecules. *Chem. Rev.*, 118 (15):7293–7361, 2018.

[178] Finley, J., Malmqvist, P., Roos, B. O., and Serrano-Andrés, L. The multi-state CASPT2 method. *Chem. Phys. Lett.*, 288(2):299 – 306, 1998. ISSN 0009-2614. doi: https://doi.org/10.1016/S0009-2614(98)00252-8.

[179] Shiozaki, T., Győrffy, W., Celani, P., and Werner, H. J. Communication: Extended multi-state complete active space second-order perturbation theory: Energy and nuclear gradients. *J. Chem. Phys.*, 135:081106, 2011. doi: 10.1063/1.3633329.

[180] Sand, A. M., Hoyer, C. E., Truhlar, D. G., and Gagliardi, L. State-interaction pair-density functional theory. *J. Chem. Phys.*, 149(2):024106, 2018.

[181] Zou, X., Sun, Z., Zhao, H., and Zhang, C. y. Mechanistic insight into photocrosslinking reaction between triplet state 4-thiopyrimidine and thymine. *Phys. Chem. Chem. Phys.*, 21 (38):21305–21316, 2019.

[182] Casida, M. E. Time-dependent density functional response theory for molecules. In *Recent Advances In Density Functional Methods: (Part I)*, pages 155–192. World Scientific, 1995.

[183] Casida, M. E. Time-dependent density-functional theory for molecules and molecular solids. *J. Mol. Struct.*, 914(1-3):3–18, 2009.

[184] Neese, F., Wennmohs, F., Becker, U., and Riplinger, C. The ORCA quantum chemistry program package. *J. Chem. Phys.*, 152(22):224108, 2020.

[185] Becke, A. Density-functional thermochemistry. III. the role of exact exchange. *Chem. Phys.*, 98:5648, 1993.

[186] Kendall, R. A., Dunning Jr, T. H., and Harrison, R. J. Electron affinities of the first-row atoms revisited. systematic basis sets and wave functions. *J. Chem. Phys.*, 96(9):6796–6806, 1992.

[187] Dunning Jr, T. H. Gaussian basis sets for use in correlated molecular calculations. I. the atoms boron through neon and hydrogen. *J. Chem. Phys.*, 90(2):1007–1023, 1989.

[188] Yanai, T., Tew, D. P., and Handy, N. C. A new hybrid exchange–correlation functional using the coulomb-attenuating method (CAM-B3LYP). *Chem. Phys. Lett.*, 393(1-3):51–57, 2004.

[189] Roos, B. O. and Andersson, K. Multiconfigurational perturbation theory with level shift—the Cr_2 potential revisited. *Chemical Phys. Lett.*, 245(2-3):215–223, 1995.

[190] Roos, B. O., Andersson, K., Fülscher, M. P., Serrano-Andrés, L., Pierloot, K., Merchán, M., and Molina, V. Applications of level shift corrected perturbation theory in electronic spectroscopy. *J. Mol. Struct. (Theochem)*, 388:257–276, 1996.

[191] Perdew, J. P., Burke, K., and Ernzerhof, M. Generalized gradient approximation made simple. *Phys. Rev. Lett.*, 77(18):3865, 1996.

[192] Tishchenko, O., Zheng, J., and Truhlar, D. G. Multireference model chemistries for thermochemical kinetics. *J.Chem. Theor. Comput.*, 4(8):1208–1219, 2008.

[193] Sears, J. S., Koerzdoerfer, T., Zhang, C. R., and Brédas, J. L. Communication: Orbital instabilities and triplet states from time-dependent density functional theory and long-range corrected functionals. *J. Chem. Phys.*, 135(15):151103, 2011.

[194] Lykhin, A. O., Truhlar, D. G., and Gagliardi, L. Dipole moment calculations using multiconfiguration pair-density functional theory and hybrid multiconfiguration pair-density functional theory. *J. Chem. Theory Comput.*, 17(12):7586–7601, 2021. doi: 10.1021/acs.jctc.1c00915. PMID: 34793166.

[195] Calio, P. B., Truhlar, D. G., and Gagliardi, L. Nonadiabatic molecular dynamics by multiconfiguration pair-density functional theory. *J. Chem. Theory Comput.*, 18(2):614–622, 2022. doi: 10.1021/acs.jctc.1c01048. PMID: 35030306.

[196] Pulay, P. Ab initio calculation of force constants and equilibrium geometries in polyatomic molecules: I. theory. *Mol. Phys.*, 17(2):197–204, 1969.

[197] Said, Y. and Wegman, E. Roadmap for optimization. *Wiley Interdiscip. Rev. Comput. Stat.*, 1(1):3–17, 2009.

[198] Schlegel, H. B. Geometry optimization. *Wiley Interdisciplinary Reviews: Comput. Mol. Sci.*, 1(5):790–809, 2011.

[199] Robb, M. A. *Theoretical chemistry for electronic excited states*, volume 12. Royal Society of Chemistry, 2018.

[200] Evans, R. C., Douglas, P., and Burrow, H. D. *Applied photochemistry*. Springer, 2013.

[201] Peach, M. J., Warner, N., and Tozer, D. J. On the triplet instability in TDDFT. *Mol. Phys.*, 111(9-11):1271–1274, 2013.

[202] Yue, H., Zhu, C., Huang, L., Dewanji, A., and Rueping, M. Advances in allylic and benzylic C–H bond functionalization enabled by metallaphotoredox catalysis. *Chem Commun (Camb)*, 58(2):171–184, 2022.

[203] Pierloot, K., Dumez, B., Widmark, P. O., and Roos, B. O. Density matrix averaged atomic natural orbital (ANO) basis sets for correlated molecular wave functions. *Theor. Chim. Acta*, 90(2):87–114, 1995.

[204] Douglas, M. and Kroll, N. M. Quantum electrodynamical corrections to the fine structure of helium. *Ann. Phys.*, 82(1):89–155, 1974.

[205] Marin, M. d. C., De Vico, L., Dong, S. S., Gagliardi, L., Truhlar, D. G., and Olivucci, M. Assessment of MC-PDFT excitation energies for a set of QM/MM models of rhodopsins. *J. Chem. Theory Comput.*, 15(3):1915–1923, 2019.

[206] Roos, B. O., Taylor, P. R., and Sigbahn, P. E. A complete active space SCF method (CASSCF) using a density matrix formulated super-ci approach. *Chem. Phys.*, 48(2):157–173, 1980.

[207] Dauben, W. G., Salem, L., and Turro, N. J. A Classification of Photochemical Reactions. *Acc. Chem. Res.*, 8:41, 1975. ISSN 00092347. doi: 10.1021/cen-v046n004.p005.

[208] Siegbahn, P. E. Generalizations of the direct CI method based on the graphical unitary group approach. I. Single replacements from a complete CI root function of any spin, first order wave functions. *J. Chem. Phys.*, 70(12):5391–5397, 1979. ISSN 00219606. doi: 10.1063/1.437473.

[209] Siegbahn, P. E. Generalizations of the direct Cl method based on the graphical unitary group approach. II. Single and double replacements from any set of reference configurations. *J. Chem. Phys.*, 72(3):1647–1656, 1980. ISSN 00219606. doi: 10.1063/1.439365.

[210] Granovsky, A. A. Extended multi-configuration quasi-degenerate perturbation theory: The new approach to multi-state multi-reference perturbation theory. *J. Chem. Phys.*, 134(21): 214113, 2011. ISSN 00219606. doi: 10.1063/1.3596699.

[211] Angeli, C., Borini, S., Cestari, M., and Cimiraglia, R. A quasidegenerate formulation of the second order n-electron valence state perturbation theory approach. *J. Chem. Phys.*, 121(9): 4043–4049, 2004. ISSN 00219606. doi: 10.1063/1.1778711.

[212] Larsen, N. W. Microwave spectra of the six mono-13C-substituted phenols and of some monodeuterated species of phenol. Complete substitution structure and absolute dipole moment. *J. Mol. Struct.*, 51(C):175–190, 1979. ISSN 00222860. doi: 10.1016/0022-2860(79)80292-6.

[213] Ratzer, C., Küpper, J., Spangenberg, D., and Schmitt, M. The structure of phenol in the S_1-state determined by high resolution UV-spectroscopy. *Chem. Phys.*, 283(1):153–169, 2002. ISSN 0301-0104. doi: https://doi.org/10.1016/S0301-0104(02)00591-8.

[214] Spangenberg, D., Imhof, P., and Kleinermanns, K. The S_1 state geometry of phenol determined by simultaneous Franck-Condon and rotational constants fits. *Phys. Chem. Chem. Phys.*, 5(12):2505–2514, 2003. ISSN 14639076. doi: 10.1039/b301228j.

[215] Zhu, X., Malbon, C. L., and Yarkony, D. R. An improved quasi-diabatic representation of the 1, 2, 3 ^{1}A coupled adiabatic potential energy surfaces of phenol in the full 33 internal coordinates. *J. Chem. Phys.*, 144(12):124312, 2016. ISSN 00219606. doi: 10.1063/1.4944091.

[216] Zhu, X. and Yarkony, D. R. On the elimination of the electronic structure bottleneck in on the fly nonadiabatic dynamics for small to moderate sized (10-15 atom) molecules using fit diabatic representations based solely on ab initio electronic structure data: The photodissociation. *J. Chem. Phys.*, 144(2):024105, 2016. ISSN 00219606. doi: 10.1063/1.4938236.

[217] Yang, K. R., Xu, X., Zheng, J., and Truhlar, D. G. Full-dimensional potentials and state couplings and multidimensional tunneling calculations for the photodissociation of phenol. *Chem. Sci.*, 5(12):4661–4680, 2014. ISSN 20416539. doi: 10.1039/c4sc01967a.

[218] Vieuxmaire, O. P., Lan, Z., Sobolewski, A. L., and Domcke, W. Ab initio characterization of the conical intersections involved in the photochemistry of phenol. *J. Chem. Phys.*, 129 (22):224307, 2008. ISSN 00219606. doi: 10.1063/1.3028049.

[219] Papajak, E., Zheng, J., Xu, X., Leverentz, H. R., and Truhlar, D. G. Perspectives on basis sets beautiful: Seasonal plantings of diffuse basis functions. *J. Chem. Theory Comput.*, 7: 3027, 2011.

[220] Fdez. Galván, I., Vacher, M., Alavi, A., Angeli, C., Aquilante, F., Autschbach, J., Bao, J. J., Bokarev, S. I., Bogdanov, N. A., Carlson, R. K., Chibotaru, L. F., Creutzberg, J., Dattani, N., Delcey, M. G., Dong, S. S., Dreuw, A., Freitag, L., Frutos, L. M., Gagliardi, L., Gendron, F., Giussani, A., González, L., Grell, G., Guo, M., Hoyer, C. E., Johansson, M., Keller, S., Knecht, S., Kovačević, G., Källman, E., Li Manni, G., Lundberg, M., Ma, Y., Mai, S., Malhado, J. P., Malmqvist, P. Å., Marquetand, P., Mewes, S. A., Norell, J., Olivucci, M., Oppel, M., Phung, Q. M., Pierloot, K., Plasser, F., Reiher, M., Sand, A. M., Schapiro, I., Sharma, P., Stein, C. J., Sørensen, L. K., Truhlar, D. G., Ugandi, M., Ungur, L., Valentini, A., Vancoillie, S., Veryazov, V., Weser, O., Wesołowski, T. A., Widmark, P. O., Wouters, S., Zech, A., Zobel, J. P., and Lindh, R. OpenMolcas: From Source Code to Insight. *J. Chem. Theory Comput.*, 15(11):5925–5964, 2019. ISSN 15499626. doi: 10.1021/acs.jctc.9b00532.

[221] Glockler, G. and Fuller, D. Helium hydride ion. *J. Chem. Phys*, 1(12):886–887, 1933.

[222] Bishop, D. M. and Cheung, L. M. A theoretical investigation of HeH^+. *J. of Mol. Spectrosc*, 75(3):462–473, 1979.

[223] Peyerimhoff, S. Hartree—fock—roothaan wavefunctions, potential curves, and charge-density contours for the HeH^+ ($X^1\ \Sigma^+$) and NeH^+ ($x^1\ \Sigma^+$) molecule ions. *J. Chem. Phys*, 43(3):998–1010, 1965.

[224] Güsten, R., Wiesemeyer, H., Neufeld, D., Menten, K. M., Graf, U. U., Jacobs, K., Klein, B., Ricken, O., Risacher, C., and Stutzki, J. Astrophysical detection of the helium hydride ion HeH^+. *Nature*, 568(7752):357–359, 2019.

[225] Novotný, O., Wilhelm, P., Paul, D., Ábel Kálosi, Saurabh, S., Becker, A., Blaum, K., George, S., Göck, J., Grieser, M., Grussie, F., von Hahn, R., Krantz, C., Kreckel, H., Meyer, C., Mishra, P. M., Muell, D., Nuesslein, F., Orlov, D. A., Rimmler, M., Schmidt, V. C., Shornikov, A., Terekhov, A. S., Vogel, S., Zajfman, D., and Wolf, A. Quantum-state–selective electron recombination studies suggest enhanced abundance of primordial HeH^+. *Science*, 365(6454):676–679, 2019.

[226] Fallon, R. J., Vanderslice, J. T., and Mason, E. A. Potential energy curves for lithium hydride. *J. Chem. Phys.*, 32:1453, 1960.

[227] Li, K. C. and Stwalley, W. C. The $A^1\Sigma^+ \rightarrow X^1\Sigma^+$ bands of the isotopic lithium hydrides. *J. Mol. Spectrosc.*, 69:294, 1978.

[228] Pardo, A., Camacho, J. J., and Poyato, J. M. L. The Padé-approximant method and its applications in the construction of potential-energy curves for the lithium hydride molecule. *Chem. Phys. Lett.*, 131:490, 1986.

[229] Stwalley, W. C. and Zemke, W. T. Spectroscopy and structure of the lithium hydride diatomic molecules and ions. *J. Phys. Chem. Ref. Data*, 22:87, 1993.

[230] Tung, W. C., Pavanello, M., and Adamowicz, L. Very accurate potential energy curve of the LiH molecule. *J. Chem. Phys.*, 134:64117, 2011.

[231] Maniero, A. M. and Acioli, P. H. Full configuration interaction pseudopotential determination of the ground-state potential energy curves of Li_2 and LiH. *Int. J. Quantum Chem.*, 103 (5):711–717, 2005.

[232] Bandrauk, A. D. and Gauthier, J. M. Infrared multiphoton dissociation of lithium fluoride by a coupled equation method. *J. Phys. Chem.*, 93(22):7552–7554, 1989.

[233] McLean, A. Optimized single-configuration wavefunction for the ground state of lithium fluoride. *J. Chem. Phys*, 39(10):2653–2665, 1963.

[234] Benson, G. and Van der Hoff, B. The development of a quantum-mechanical model for the lithium fluoride molecule. *J. Chem. Phys*, 22(3):469–475, 1954.

[235] Fallon, R. J., Vanderslice, J. T., and Mason, E. A. Potential energy curves for lithium hydride. *J. Chem. Phys*, 32(5):1453–1455, 1960.

[236] Roth, W., Imhof, P., Gerhards, M., Schumm, S., and Kleinermanns, K. Reassignment of ground and first excited state vibrations in phenol. *Chem. Phys.*, 252(1-2):247–256, 2000. ISSN 03010104. doi: 10.1016/S0301-0104(99)00326-2.

[237] Dixon, R. N., Oliver, T. A., and Ashfold, M. N. Tunnelling under a conical intersection: Application to the product vibrational state distributions in the UV photodissociation of phenols. *J. Chem. Phys.*, 134(19):194303, 2011. ISSN 00219606. doi: 10.1063/1.3585609.

[238] Pino, G. A., Oldani, A. N., Marceca, E., Fujii, M., Ishiuchi, S. I., Miyazaki, M., Broquier, M., Dedonder, C., and Jouvet, C. Excited state hydrogen transfer dynamics in substituted phenols and their complexes with ammonia: $\pi\pi^*$-$\pi\sigma^*$energy gap propensity and ortho-substitution effect. *J. Chem. Phys.*, 133(12):124313, 2010. ISSN 00219606. doi: 10.1063/1.3480396.

[239] Hause, M. L., Yoon, Y. H., Case, A. S., and Crim, F. F. Dynamics at conical intersections: The influence of O-H stretching vibrations on the photodissociation of phenol. *J. Chem. Phys.*, 128(10):104307, 2008. ISSN 00219606. doi: 10.1063/1.2831512.

[240] Granucci, G., Hynes, J. T., Millié, P., and Tran-Thi, T. H. A theoretical investigation of excited-state acidity of phenol and cyanophenols. *J. Am. Chem. Soc.*, 122(49):12243–12253, 2000. ISSN 00027863. doi: 10.1021/ja993730j.

[241] Sun, Q., Zhang, X., Banerjee, S., Bao, P., Barbry, M., Blunt, N. S., Bogdanov, N. A., Booth, G. H., Chen, J., Cui, Z. H., Eriksen, J. J., Gao, Y., Guo, S., Hermann, J., Hermes, M. R., Koh, K., Koval, P., Lehtola, S., Li, Z., Liu, J., Mardirossian, N., McClain, J. D., Motta, M., Mussard, B., Pham, H. Q., Pulkin, A., Purwanto, W., Robinson, P. J., Ronca, E., Sayfutyarova, E., Scheurer, M., Schurkus, H. F., Smith, J. E. T., Sun, C., Sun, S. N., Upadhyay, S., Wagner, L. K., Wang, X., White, A., Whitfield, J. D., Williamson, M. J., Wouters, S., Yang, J., Yu, J. M., Zhu, T., Berkelbach, T. C., Sharma, S., Sokolov, A. Y., and Chan, G. K. L. Recent developments in the PySCF program package. *J. Chem. Phys.*, 153: 024109, 2020. doi: 10.1063/5.0006074.

[242] Jensen, P. and Bunker, P. R. The geometry and the inversion potential function of formaldehyde in the $^1A_2$ and $^3A_2$ electronic states. *J. Mol. Spectrosc*, 94(1):114–125, 1982.

[243] Takagi, K. and Oka, T. Millimeter wave spectrum of formaldehyde. *J. Phys. Soc. Jpn.*, 18 (8):1174–1180, 1963.

[244] Duncan, J. L. The ground-state average and equilibrium structures of formaldehyde and ethylene. *Mol. Phys.*, 28(5):1177–1191, 1974.

[245] Walzl, K. N., Koerting, C. F., and Kuppermann, A. Electron-impact spectroscopy of acetaldehyde. *J. Chem. Phys*, 87(7):3796–3803, 1987.

[246] Robin, M. *Higher Excited States of Polyatomic Molecules*, volume 3. Elsevier, 2012.

[247] Merchán, M. and Roos, B. O. A theoretical determination of the electronic spectrum of formaldehyde. *Theor. Chim. Acta*, 92(4):227–239, 1995.

[248] Jacquemin, D. What is the key for accurate absorption and emission calculations, energy or geometry? *J. Chem. Theory Comput.*, 14(3):1534–1543, 2018. doi: 10.1021/acs.jctc.7b01224.

[249] Koch, H., Christiansen, O., Jörgensen, P., Sanchez de Merás, A. M., and Helgaker, T. The CC3 model: An iterative coupled cluster approach including connected triples. *J. Chem. Phys*, 106(5):1808–1818, 1997.

[250] Christiansen, O., Koch, H., and Jörgensen, P. Response functions in the CC3 iterative triple excitation model. *J. Chem. Phys*, 103(17):7429–7441, 1995.

[251] Christiansen, O., Koch, H., and Jörgensen, P. Perturbative triple excitation corrections to coupled cluster singles and doubles excitation energies. *J. Chem. Phys*, 105(4):1451–1459, 1996.

[252] Dreuw, A. and Wormit, M. The algebraic diagrammatic construction scheme for the polarization propagator for the calculation of excited states. *WIREs Comput. Mol. Sci.*, 5(1): 82–95, 2015.

[253] Loos, P. F., Scemama, A., Blondel, A., Garniron, Y., Caffarel, M., and Jacquemin, D. A mountaineering strategy to excited states: Highly accurate reference energies and benchmarks. *J. Chem. Theory Comput.*, 14(8):4360–4379, 2018.

[254] Loos, P. F., Lipparini, F., Boggio-Pasqua, M., Scemama, A., and Jacquemin, D. A mountaineering strategy to excited states: Highly accurate energies and benchmarks for medium sized molecules. *J. Chem. Theory Comput.*, 16(3):1711–1741, 2020.

[255] Loos, P. F., Scemama, A., Boggio-Pasqua, M., and Jacquemin, D. Mountaineering strategy to excited states: Highly accurate energies and benchmarks for exotic molecules and radicals. *J. Chem. Theory Comput.*, 16(6):3720–3736, 2020.

[256] Loos, P. F. and Jacquemin, D. A mountaineering strategy to excited states: Highly accurate energies and benchmarks for bicyclic systems. *J. Phys. Chem. A*, 125(47):10174–10188, 2021.

[257] Budzák, Š., Scalmani, G., and Jacquemin, D. Accurate excited-state geometries: A CASPT2 and coupled-cluster reference database for small molecules. *J. Chem. Theory Comput.*, 13 (12):6237–6252, 2017.

[258] Christensen, M., Nilsson, E. J. K., and Konnov, A. A. A systematically updated detailed kinetic model for CH_2O and CH_3OH combustion. *Energy Fuels*, 30(8):6709–6726, 2016.

[259] Sjöholm, J., Rosell, J., Li, B., Richter, M., Li, Z., Bai, X. S., and Aldén, M. Simultaneous visualization of OH, CH, CH_2O and toluene PLIF in a methane jet flame with varying degrees of turbulence. *Proc Combust Inst.*, 34(1):1475–1482, 2013.

[260] Lee, S. H., Ong, C. S., and Lee, Y. T. Evidence of CH_2O ($\tilde{a}^3A_2$) and C_2H_4 ($\tilde{a}^3B_{1u}$) produced from photodissociation of 1, 3-trimethylene oxide at 193 nm. *J. Chem. Phys*, 124(7):074306, 2006.

[261] Widmark, P. O., Malmqvist, P. Å., and Roos, B. O. Density matrix averaged atomic natural orbital (ANO) basis sets for correlated molecular wave functions. *Theor. Chim. Acta*, 77(5): 291–306, 1990.

[262] Bao, J. J. and Truhlar, D. G. Automatic active space selection for calculating electronic excitation energies based on high-spin unrestricted hartree–fock orbitals. *J. Chem. Theory Comput.*, 15(10):5308–5318, 2019.

[263] Clouthier, D. J. and Ramsay, D. A. The spectroscopy of formaldehyde and thioformaldehyde. *Annu. Rev. Phys. Chem.*, 34(1):31–58, 1983.

[264] Godunov, I. A., Abramenkov, A. V., Bataev, V. A., and Pupyshev, V. I. Potential functions of inversion of R_2CO (R= H, F, Cl) molecules in the lowest excited electronic states. *Russ. Chem. Bull.*, 48(4):640–646, 1999.

[265] Gagliardi, L., Truhlar, D. G., Li Manni, G., Carlson, R. K., Hoyer, C. E., and Bao, J. L. Multiconfiguration pair-density functional theory: A new way to treat strongly correlated systems. *Accounts of chemical research*, 50(1):66–73, 2017.

[266] Sharma, P., Bao, J. J., Truhlar, D. G., and Gagliardi, L. Multiconfiguration pair-density functional theory. *Annual Review of Physical Chemistry*, 72:541–564, 2021.

[267] Taylor, S., Wilden, D. G., and Comer, J. Electron energy-loss spectroscopy of forbidden transitions to valence and rydberg states of formaldehyde. *Chem. Phys.*, 70(3):291–298, 1982.

[268] Battaglia, S. and Lindh, R. Extended dynamically weighted CASPT2: The best of two worlds. *J. Chem. Theory Comput.*, 16(3):1555–1567, 2020.

[269] Battaglia, S. and Lindh, R. On the role of symmetry in XDW-CASPT2. *J. Chem. Phys.*, 154 (3):034102, 2021.

[270] Birss, F., Gordon, R., Ramsay, D., and Till, S. High resolution studies of the $\tilde{A}^1A_2$-$\tilde{X}^1A_1$ system of 13C-formaldehyde. *Can. J. Phys.*, 57(10):1676–1680, 1979.

[271] Job, V., Sethuraman, V., and Innes, K. The 3500 $\tilde{A}^1A_2$-$\tilde{X}^1A_1$ transition of formaldehyde-H_2, D_2, and HD: Vibrational and rotational analyses. *J. Mol. Spectrosc.*, 30(1-3):365–426, 1969.

[272] Dirac, P. A. M. A new notation for quantum mechanics. In *Mathematical Proceedings of the Cambridge Philosophical Society*, volume 35, pages 416–418. Cambridge University Press, 1939.

[273] Oelgemöller, M. and Hoffmann, N. Studies in organic and physical photochemistry - an interdisciplinary approach. *Org. Biomol. Chem.*, 143(31):7392–7442, 2016. doi: 10.1039/c6ob00842a.

[274] Dauben, W., Salem, L., and Turro, N. A classification of photochemical reactions. *Acc. Chem. Res.*, 8(2):41–54, 1975. doi: 10.1021/ar50086a001.

[275] Plasser, F., Aquino, A. J., Lischka, H., and Nachtigallová, D. Electronic excitation processes in single-strand and double-strand DNA: a computational approach. In *Photoinduced Phenomena in Nucleic Acids II*, pages 1–37. Springer, 2014. doi: 10.1007/128_2013_517.

[276] Roos, B. O. The complete active space self-consistent field method and its applications in electronic structure calculations. *Adv. Chem. Phys.*, 69:399–445, 1987. doi: 10.1002/9780470142943.ch7.

[277] Matsika, S. and Krylov, A. Introduction: Theoretical modeling of excited state processes. *Chem. Rev.*, 118(15):6925–6926, 2018. doi: 10.1021/acs.chemrev.8b00436.

[278] Abouaf, R., Pommier, J., Dunet, H., Quan, P., Nam, P. C., and Nguyen, M. T. The triplet state of cytosine and its derivatives: Electron impact and quantum chemical study. *J. Chem. Phys.*, 121(23):11668–11674, 2004. doi: 10.1063/1.1812533.

[279] Sobolewski, A., Domcke, W., Dedonder-Lardeux, C., and Jouvet, C. Excited-state hydrogen detachment and hydrogen transfer driven by repulsive $1\pi\sigma^*$ states: A new paradigm for nonradiative decay in aromatic biomolecules. *Phys. Chem. Chem. Phys.*, 4(7):1093–1100, 2002.

[280] Vidal, C. and Stwalley, W. Potential energy curves and adiabatic corrections of weakly bound states: Application to the LiH $B^1\pi$ state. *J. Chem. Phys.*, 80(6):2697–2703, 1984. doi: 10.1063/1.447067.

[281] Schreiber, M., Silva-Junior, M. R., Sauer, S. P., and Thiel, W. Benchmarks for electronically excited states: CASPT2, CC2, CCSD, and CC3. *J. Chem. Phys.*, 128(13):134110, 2008. doi: 10.1063/1.2889385.

[282] Helmich-Paris, B. Benchmarks for electronically excited states with CASSCF methods. *J. Chem. Theory Comput.*, 2019. doi: 10.1021/acs.jctc.9b00325.

[283] Hoyer, C. E., Ghosh, S., Truhlar, D. G., and Gagliardi, L. Multiconfiguration pair-density functional theory is as accurate as CASPT2 for electronic excitation. *J. Phys. Chem. Letters*, 7(3):586–591, 2016. doi: 10.1021/acs.jpclett.5b02773.

[284] Andersson, K., Malmqvist, P. A., Roos, B. O., Sadlej, A. J., and Wolinski, K. Solar energy conversion by dye-sensitized photovoltaic cells. *J. Phys. Chem.*, 44(20):6841–6851, 2005. doi: 10.1021/ic0508371.

[285] Zhugayevych, A. and Tretiak, S. Theoretical description of structural and electronic properties of organic photovoltaic materials. *Annu. Rev. Phys. Chem.*, 66(1):305–330, 2015. doi: 10.1146/annurev-physchem-040214-121440.

[286] Adams, S. T. and Miller, S. C. Beyond D-luciferin: expanding the scope of bioluminescence imaging in vivo. *Curr. Opin. Chem. Biol.*, 21:112 – 120, 2014. ISSN 1367-5931. doi: https://doi.org/10.1016/j.cbpa.2014.07.003.

[287] Improta, R., Santoro, F., and Blancafort, L. Quantum mechanical studies on the photophysics and the photochemistry of nucleic acids and nucleobases. *Chem. Rev*, 116(6):3540–3593, 2016. doi: 10.1021/acs.chemrev.5b00444.